

DISSERTATION

TROPICAL DEEP CONVECTIVE CLOUD MORPHOLOGY

Submitted by

Matthew R. Igel

Department of Atmospheric Science

In partial fulfillment of the requirements

For the Degree of Doctor of Philosophy

Colorado State University

Fort Collins, Colorado

Fall 2014

Doctoral Committee:

Advisor: Susan van den Heever

Richard Eykholt
Eric Maloney
Graeme Stephens

Copyright by Matthew R. Igel 2014

All Rights Reserved

ABSTRACT

TROPICAL DEEP CONVECTIVE CLOUD MORPHOLOGY

A cloud-object partitioning algorithm is developed. It takes contiguous CloudSat cloudy regions and identifies various length scales of deep convective clouds from a tropical, oceanic subset of data. The methodology identifies a level above which anvil characteristics become important by analyzing the cloud object shape. Below this level in what is termed the pedestal region, convective cores are identified based on reflectivity maxima. Identifying these regions allows for the assessment of length scales of the anvil and pedestal of the deep convective clouds. Cloud objects are also appended with certain environmental quantities from the ECMWF reanalysis. Simple geospatial and temporal assessments show that the cloud object technique agrees with standard observations of local frequency of deep-convective cloudiness. Additionally, the nature of cloud volume scale populations is investigated. Deep convection is seen to exhibit power-law scaling. It is suggested that this scaling has implications for the continuous, scale invariant, and random nature of the physics controlling tropical deep convection and therefore on the potentially unphysical nature of contemporary convective parameterizations.

Deep-convective clouds over tropical oceans play important roles in Earth's climate system. The response of tropical, deep convective clouds to sea surface temperatures (SSTs) is investigated using this new data set. Several previously proposed feedbacks are examined: the FAT hypothesis, the Iris hypothesis, and the Thermostat hypothesis. When the data are analyzed per cloud object, each hypothesis is broadly found to correctly predict cloud behavior in nature, although it appears that the FAT hypothesis needs a slight modification to allow for cooling

cloud top temperatures with increasing SSTs. A new response that shows that the base temperature of deep convective anvils remains approximately constant with increasing SSTs is introduced. These cloud-climate feedbacks are integrated to form a more comprehensive theory for deep convective anvil responses to SST.

An investigation into the physical shape and size of mature, oceanic, tropical, deep convective clouds is conducted. Mean cloud objects are discussed. For single-core clouds, the mean cloud has an anvil width of 95 km, a pedestal width of 11 km, and an anvil thickness of 6.4 km. The number of identified convective cores within pedestal correlates well with certain length scales and morphological attributes of cloud objects. As the number of cores increases, so does the size of the mean cloud object. Pedestal width is shown to regress linearly to anvil width when a $2/3^{\text{rd}}$ power scaling is applied to pedestal width. This result implies continuous but retarded growth of anvils with growing pedestals and equivalence in the mass flux convecting through the pedestal and into the anvil. Trends in cloud scales with cloud base and top heights are investigated to shed light on related convective parameterization assumptions and on convective transport, respectively. Many of the results obtained using the CloudSat methodology are also examined with a large-domain radiative-convective equilibrium numerical simulation and are found to exhibit similar trends when modeled. Finally, various CloudSat sampling issues are discussed in several appendices.

Utilizing the CloudSat cloud object database, an examination of the sensitivity of oceanic, mature, deep convective cloud morphology to environmental characteristics is conducted. Convective available potential energy (CAPE), aerosol optical depth, mid-level vertical velocity, and troposphere deep shear are all included as meteorological measures. The sensitivity of various aspects of convective morphology to each one of these environmental

characteristics is assessed individually. The results demonstrate that clouds tend to be invigorated by higher CAPE, aerosol amount, and upward mid-level vertical velocity. Stronger shear tends to make clouds wider but also shallower. The relative importance of each of these, and some additional, environmental measures to trends in cloud morphology are compared. It is found that aerosol, mid-level vertical velocity, and sea surface temperature tend to be the most influential environmental characteristics to convective morphology. The results are shown to be insensitive to the manner in which the environment is measured. The potentially surprising insensitivity of cloud morphology to CAPE is discussed in detail.

ACKNOWLEDGEMENTS

I would like to acknowledge my dissertation advisor, Dr. Susan van den Heever, who has stood by my work, and the rest of my committee for their helpful suggestions. I would also like to thank the NASA CloudSat project (5-319160) and NASA Headquarters under the NASA Earth and Space Science Fellowship Program (NNX 13AN66H) for providing funding over the years. A special acknowledgement is extended to Mr. Aryeh Drager who worked on the implementation of the object identification, provided valuable insight and committed unique effort on the partitioning methods, and who produced figures for the methods in *Chapter II*.

DEDICATION

I would like to dedicate this work to my wonderful wife who despite working only one office away is rarely even that far from my mind.

TABLE OF CONTENTS

Abstract.....	ii
Acknowledgements.....	v
Dedication.....	vi
Table of Contents.....	vii
Chapter I: Introduction.....	1
Chapter II: A Cloudsat Cloud-Object Partitioning Technique and Applications to Scale Pop	6
Introduction.....	6
Data and Methods	8
Data Validation	26
Theories on Scales	30
Conclusions.....	36
Chapter III: Assessment and Integration of Deep Convective Anvil-Climate Feedbacks.....	50
Introduction.....	50
Anvil-Radiation Feedbacks.....	53
Conclusions.....	61
Chapter IV: Deep Convective Cloud Morphology as Observed by CloudSat.....	70

Introduction and Background	70
Methods.....	74
Results and Discussion	75
Conclusions.....	94
Sampling Issues	96
 Chapter V: The Sensitivity and Relative Influence of Environmental Characteristics to Deep..	118
Introduction and Background	118
Methods.....	122
Theoretical Framework.....	124
Results and Discussion	126
Summary.....	142
 Chapter VI: Conclusions and Summary	154
 Citations	158

CHAPTER I: INTRODUCTION

Studies of tropical clouds tend to focus on either of two scales. The most common is the scale at which clouds can be assumed to be well equilibrated with the environment such that a physical separation exists between the scales of interest and the clouds themselves. The second is one that examines individual clouds – their internal dynamics, entrainment characteristics, and the like. At this latter scale the larger environment hardly matters except perhaps as an initial condition. This study seeks to describe an intermediate size, one for which scale separation cannot be assumed but at which individual clouds still create large perturbations such that equilibrium cannot be assumed.

As such, this study will begin the long process of laying a framework for an eminent impending unfortunate event: the point at which either climate or weather prediction models cannot assume scale separation but cannot yet successfully resolve the details of convection. Weather prediction models are, in fact, approaching this scale. This impending issue is one of the major theoretical issues at the time of the writing of this dissertation. Thus, the work included in this dissertation begins to answer a simple question: *across the tropical oceans, what controls the physical length scales of individual deep convective clouds?* Beginning to answer this question will involve developing theories that work up from the deep-cloud scale.

To answer such a question, four aspects of tropical convective length scales are investigated. These form the four science chapters of this dissertation.

Chapter II: This chapter is dedicated foremost to detailing the newly developed tool which will be used for the analysis in the following chapters. The method constructed uses

CloudSat [*Stephens et al*, 2008] data in a new way purposefully directed at enumerating length scales of tropical convection and therefore at the leading question. The methodology discussed parses the CloudSat dataset into individual tropical, mature, deep convective entities. It also partitions these “cloud objects” into physical components. This chapter is supplemented with a simple assessment of the population distribution of a certain cloud length scale property.

Chapter III: Tropical deep convective cloud properties are often assumed to vary as a function of the climate state. In this chapter, several ways in which clouds are sometimes assumed to depend on climate are assessed with the new CloudSat database. For the first time, these ideas are conceptually merged into a single idea. This merger represents a fundamental change in their theoretical conceptualization.

Chapter IV: One of the often-overlooked dependencies of cloud scales are clouds themselves. That is, as clouds grow, their components do so in a related way. In this chapter, the ways in which the length scales of different cloud components depend on one another is examined. It is argued that through such simple analysis, new insight into cloud dynamics are gleaned. The relationship between the widths of convective “anvils” and parent “pedestals” is detailed. While the analysis is often simple, this chapter is the *tour de force* of this dissertation.

Chapter V: The final results examine how six different aspects of cloud morphology change as a function of various environmental measurements. The dependencies of cloud size on convective available potential energy, aerosol amount, mid-level vertical velocity, and troposphere-deep shear are examined. The relative importance of these environmental influences to dictating length scales is then examined.

These four chapters will examine the population of length scales and their dependence on climate, on near-field meteorological environment, and on the related components of clouds themselves.

Thus the theoretical glue that binds these chapters is the idea that *by enumerating simple physical scales of deep convection, insight into physical cloud processes can be gained*. The practical link is a new dataset. The length scales are taken from a wide panoply of real world clouds observed by CloudSat across global oceans. This perspective gives this study a unique framework: it is global; it is appropriately long term (5 years); it is highly detailed; and it is inclusive of deep convective clouds. From this perspective, universal physical processes can be inferred at least for tropical clouds. This framework was developed to provide the kind of physical understanding required to make the long-term transition from clouds-as-plumes to highly variable, physically driven clouds in both models and in conceptual thinking. The analysis techniques are often simple. They are intentionally naïve in a specific attempt to preclude any particular result or implication. This does not mean that the analysis is not well reasoned or that it is disconnected from previous results. Since the tool being used is new, an attempt has been made to go back to fundamental questions that have either received little consideration before or to which this tool may be better suited than any before.

Historical Context

Many aspects of the main body of work included below complement a disparate body of observational work on tropical convection. The seminal investigations into the basic nature of tropical convection began with structured fieldwork in GATE and TOGA-COARE. Results from these campaigns formed much of the basic understanding of tropical convection. Not the least importantly of which was the discovery that tropical, oceanic deep convection was

characteristically different than the over-land thunderstorms that had been studied previously. The primary limitation of these field campaign studies was their small spatial coverage. Even when combined, the area observed covered less than 1% of the tropical oceans for an infinitesimal time. Since those campaigns and in an effort to overcome these limitations, efforts have been focused primarily on satellite studies. Satellite observations provide good spatial *coverage* at the expense of spatial and temporal *resolution*. Most passive sensors are also limited to a top-down view of clouds. This view obscures many of the interesting internal aspects of convection, which itself is inherently a vertical phenomenon. Passive sensors have been combined with an active one, the Tropical Rainfall Measuring Mission [*Kummerow et al*, 1998], to great effect in order to relate clouds to rain. The new CloudSat analysis below adds high spatial coverage with detailed observations of vertically resolved *clouds*, not just rain.

The most basic idea of this dissertation, asking at what length scales convection occurs, has a direct genealogy especially originating from the original field work in the tropics. The more specific issue of detailing the controls on these length scales stems from a much broader family tree. The chapters to come draw from aspects of climate change research, convective theory, meteorology, and geophysics. All of these fields bring some insight into what factors control convective sizes. Climate change studies are often preoccupied with detailing the cloud-climate feedback, which outside of subsidence regions in the tropics is dominated by the kind of deep convective clouds of concern herein. Previous attempts to constrain the feedback have tended to focus on the ways in which convective anvils might respond to various changes in physical processes. Convective theorists have often drawn on the field campaigns listed previously or on small domain simulations in order to make conclusions about cloud-relative dynamic flows. These theorists have quite successfully formed a conceptual framework under

which convection is understood to evolve. Meteorology is inherently concerned with the response of certain surface fields, like rain or wind, to the larger-scale atmosphere. In the tropics, the downscale link is often some form of convection. Forced by predictive desires, special links between convective and the near-field environment have been postulated and used for prediction. And, finally, geophysics is the study of the earth system from a theoretical perspective. The creed of the field is that earth's systems obey simple physical laws. A certain body of geophysics work has been dedicated to detailing reasons for observed populations densities of scales. Clouds will be placed in this framework.

CHAPTER II: A CLOUDSAT CLOUD-OBJECT PARTITIONING TECHNIQUE AND APPLICATIONS TO SCALE POPULATIONS

1. Introduction

Convection clouds forms the primary interface between the atmosphere and what might be called “weather” in the tropical atmosphere. It could even be argued that without convection, the tropical atmosphere would cease to have any weather at all. Within the population of tropical convection, three modes are said to exist. These are shallow, congestus, and deep [Johnson *et al*, 1999]. While the roles of shallow convection and congestus clouds are important, the most influential clouds are those that sustain growth above the freezing level, the deep clouds. Among their myriad of impacts, they rain readily, reflect shortwave radiation back to space, and emit radiation at cool thermal temperatures.

This chapter will introduce a new CloudSat cloud object data set relevant for tropical oceanic deep convective clouds. While it was inspired by the work of Bacmeister and Stephens [2011] who sought to partition clouds into some of the same components that this research does, many of the methods utilized are very different. Following a brief description of the raw data, a the discussion of data processing will be conducted. This will include the details, justification, and assessment of the filtering methods used to determine which raw data are included in the final data set. A detailed description of the new deep convective pedestal/ anvil separation algorithm with examples will follow. In section 3, some familiar aspects of convective occurrence and scale populations, especially those that are unique to the cloud object analysis

done here, are investigated. To compliment the observations, a large domain, cloud-resolving simulation is also analyzed.

It has been shown that clouds across a wide variety of shapes and sizes exhibit (vertical or horizontal length) scale invariant behavior – they exhibit similar characteristics across a wide range of physical length scales. *Machado and Rossow* [1993] showed that systems as large as mesoscale convective systems (MCS) do. Similarly indicative, *Wood* [2012], and *Cahalan and Snider* [1989] have shown that shallow cloud length scales are distributed following a power-law relationship. *Wood and Field* [2011] showed that a power-law scaling exists across a wide range of clouds. Dust devils have also been shown to exhibit similar power-law population distributions [*Lorenz*, 2011]. These results provide important information about the clouds themselves. They imply that clouds behave in a certain way across a wide range of types and sizes. The power-law or exponential distributions mean that clouds are, in some senses, randomly distributed in space and time (i.e. they are scale invariant) with a overabundance of large clouds (i.e. they exhibit power-laws). This result would seem to provide fundamental physical insight into the clouds themselves: they are organized and shaped by a variety of scale independent physics [*Bak et al.*, 1987] which work together in such a way as to yield a population with many small clouds, and few, but a slight overabundance of the largest clouds. The power-law distribution is taken to imply that it is the internal dynamics of a system that form the system properties and not some external forcing [*Yano and Plant*, 2012]. The particular mechanism will be discussed below. The occurrence of these previously observed cloud properties will be analyzed with the new cloud object dataset.

2. Data and Methods

The idea of dissecting scenes of remotely sensed cloud data into contiguous “pieces” of cloud is not new. Such “cloud object” techniques have been used successfully in a variety of different ways. Infrared or visible data from geostationary or polar orbiting satellites have been separated into cloudy and clear sky regions [e.g. *Xu et al.*, 2005; *Dias et al.*, 2012]. The horizontal lengths or areas of clouds within the scene have then been analyzed. The idea can be taken a step further by joining several data sources that cover the same area in order to utilize instrument benefits [e.g. *Nesbitt et al.*, 2000]. “Cloud objects” have also been defined in the vertical through the use of active sensors [e.g. *Nesbitt et al.*, 2000; *Riley et al.*, 2011; *Bacmeister and Stephens*, 2011]. In this case, the cloud object represents a vertical slice or cross section through the cloud. Because these objects provide details in the vertical plane, information about the vertical distribution of liquid water or ice or the effective width of a convective core may be obtained, for example. Fundamentally, the cloud object method can be used to define separate, contiguous cloudy regions and then to understand the physical properties of different groups of objects.

This work introduces a new CloudSat cloud object data set designed for use in investigations of deep-convective clouds. While it was inspired by the work of Bacmeister and Stephens [2011] who sought to partition clouds into some of the same components that this research does, the methods utilized are very different. The basic goal in constructing this data set is for it to be purposefully inclusive of deep convective clouds so as not to allow preconceptions about their size and shape to influence any results. Some of the selection criteria could be further refined in order to limit objects to a certain life cycle stage, say, but this is not the present objective. Following a brief description of the raw data, a discussion of data processing will be

conducted. This will include the details, justification, and assessment of the filtering methods used to determine which raw data are included in the final data set. A detailed description of the new deep convective pedestal/ anvil separation algorithm with examples will follow.

2.1. Data

The methodology developed herein uses a combination of observational data based on retrievals from the CloudSat 94 GHz cloud profiling radar (CPR) and collocated ECMWF environmental reanalysis data. CloudSat is part of the A-Train constellation of satellites and utilizes a sun-synchronous orbit that crosses the equator at approximately 0130 and 1330 local time [Stephens *et al.*, 2002]. The CloudSat radar is designed to observe cloud vertical structure and samples clouds with a vertical resolution of approximately 500 m, a cross-track resolution of approximately 1.4 km, and an along-track resolution of approximately 1.8 km [Stephens *et al.*, 2008]. Data are oversampled such that radar reflectivity and other profiles are reported with vertical spacing of 240 m and along-track spacing of 1079 m. The CloudSat Data Processing Center provides CloudSat data in granules, where one granule contains retrievals taken between two successive nighttime (0130 local time) equator crossings. Figure 1 shows one such granule, obtained on 24 October 2007. Complete information regarding CloudSat capabilities and data products may be obtained from the CloudSat Data Processing Center

(<http://cloudsat.cira.colostate.edu>).

Data available at the time of this study span from the start of CloudSat CPR operation in June 2006 to a temporary system shutdown in April 2011. The present analysis makes use of the level-2 2B-GEOPROF [Haynes and Stephens, 2007], 2B-CLDCLASS [Wang and Sassen, 2007], 2B-CWC-RVOD [Wood, 2008], 2B-FLXHR [L'Ecuyer *et al.* 2008], and 2B-TAU [Polonsky *et al.*, 2008] CloudSat products, along with the ECMWF-AUX and ECMWF2-AUX [Partain, 2007]

auxiliary data products. After elimination of the small minority of granules for which at least one of these data products is unavailable, the data set comprises approximately 20 000 granules. In keeping with the intended uses of this data set, analyses are limited to retrievals taken over tropical latitudes, defined here as $30^{\circ}\text{S} - 30^{\circ}\text{N}$ (unshaded section of Fig. II.1). Since a single granule comprises retrievals taken between successive nighttime equator crossings (see Fig. II.1), each granule contains three tropical sections: one tropical section at each end of the granule, associated with the successive nighttime equator crossings (blue line in Fig. II.1), and one central tropical section, associated with the daytime equator crossing (yellow in Fig. II.1). For this study, we have chosen to limit our analysis to the central tropical section of each granule. This choice effectively eliminates half of all available Cloudsat data but provides several benefits. We have observed that the edges of some granules are missing one or more columns of data for reasons we do not know; one benefit of considering only the central tropical section of each granule is that the potential error associated with attempting to stitch edges of adjacent granules together is avoided. It also yields only sunlit clouds, which is crucial for the assessment of anvil-radiative feedbacks in *Chapter III*. Throughout the development of this methodology, data will be pared away, sometimes seemingly excessively so (like the decision to eliminate nighttime data). However, the data set is still highly inclusive as the sheer amount of data available from 5 years of CloudSat allows for powerful statistics even with a limited subset of data.

A consequence of the A-Train's orbit is that all retrievals over tropical latitudes are taken along a track that has a large meridional component and a small zonal component. Thus, implicit in this and other analyses of tropical CloudSat retrievals [e.g., *Bacmeister and Stephens, 2011*] is the assumption that tropical clouds possess no systematic anisotropy in the horizontal. We have

no reason to reject this assumption in the ensemble mean, although individual clouds can be highly anisotropic. Additional effects of meridional sampling are discussed when relevant.

2.2. Methods

An object-based approach similar to that of *Bacmeister and Stephens* [2011] is employed to identify cloud objects within each CloudSat granule. A more general discussion of object-oriented analysis approaches is provided in *Sellars et al.* [2013]. After cloud objects are identified, a number of filters are applied in order to select mature, marine, deep-convective cloud objects for further analysis. Steps are then taken to help to analyze the morphology of each of these cloud objects. First, each cloud object is partitioned into a convective “pedestal” region and an upper “anvil” region (see 2.2.2 for definitions). A core-counting algorithm is applied in order to estimate the number of convective cores within each cloud object’s pedestal region. Following this preparation, steps are taken to evaluate heights and widths corresponding to various morphological attributes and reanalysis data are used to quantify different environmental attributes (e.g., sea-surface temperature) associated with each cloud object.

Throughout much of the discussion to follow, a sample cloud scene will be examined to illustrate the development of the methodology. The satellite plan view in Fig. II.1 provides high-level context for this scene. Figure II.2a shows the raw reflectivity observed by CloudSat over a select portion of the daytime tropical domain shown in Fig. II.1. Subsequent parts of Fig. II.2 will be discussed when relevant. The colored cloud objects labeled in Fig. II.2c will be the primary targets of discussion.

2.2.1. Identifying Cloud Objects

The 2B-GEOPROF [*Haynes and Stephens*, 2007] “Radar_Reflectivity” and “CPR_Cloud_mask” fields are used to designate each pixel within the data set as “cloudy” or

“clear.” Equivalently, the binary function $C(j,k)$ for horizontal index j and vertical index k such that $C(j,k) = 1$ for cloudy pixels and $C(j,k) = 0$ for clear pixels is created. Individual “cloud objects” are then defined as regions of contiguous cloudy pixels, where pixels are considered contiguous if they share an edge but not if they share only corner. A pixel is designated as “cloudy” if, and only if, its Radar_Reflectivity value is at least -28 dBZ and its CPR_Cloud_mask value is at least 20. This Radar_Reflectivity threshold is approximately equal to the CloudSat CPR’s minimum detectable signal, and this CPR_Cloud_mask threshold corresponds to approximately 95% confidence that the detected signal is not the result of noise [Mace, 2006]. A mask of 20 is a commonly used threshold [e.g. Sassen and Wang, 2008; Riley and Mapes, 2009]. Significantly more rigid thresholds eliminate anvil pixels too aggressively, producing anvil regions detached from their parent convective cores, while significantly more permissive thresholds result in many clearly independent cloud objects becoming connected by bridges of questionably cloudy pixels, especially in the anvil. Parts a and b of Figure II.3 illustrate the effects of various threshold choices on the cloud objects that result. These figures show that the thresholds listed above serve effectively to screen out data that are unlikely to be cloud without paring away too much data. As an anecdotal example, in the scenario illustrated in Figure II.2 and Figure II.3, more permissive thresholds would have resulted in the seemingly inappropriate incorporation of object D into object E. More rigid thresholds might have resulted in the separation of the highest-altitude cloudy region near 15°N from object E. The overall results were tested for a range of numerical thresholds and were found to be insensitive to the choices made. It may therefore be assumed that the conclusions drawn in the following chapters are robust in this regard.

Each CloudSat granule contains potentially hundreds of cloud objects. From these, likely mature, deep-convective cloud objects over tropical oceans are selected for further analysis. To be selected, a cloud object must satisfy *all* of the following criteria:

1. The cloud object must be contained entirely within the central tropical section of the granule. If a granule is incomplete and has an edge within the daytime tropical part of the orbit, objects intersecting the edge of the granule are excluded so as to eliminate incomplete cloud objects.

2. The cloud object must lie entirely over water. This criterion is enforced using the “Navigation_land_sea_flag” information provided by the 2B-GEOPROF product.

3. The cloud object must have significant vertical extent, extending down at least to the 100th vertical level (out of 125, corresponding to an average height of approximately 1.2 km AGL) and extending up to at least the 64th vertical level (corresponding to an average height of approximately 9.8 km AGL). Although 1.2 km may seem too low a threshold given the possibility of elevated convection, we have observed that nearly all CloudSat deep-convective cloud objects over tropical oceans satisfy this condition, as signals from rain result in near-uniform coverage of cloudy pixels at low heights. The five cloud objects identified in Figure II.2c satisfy all of the criteria listed thus far (note that object E continues Fig. II.3c).

4. The cloud object must contain at least one pixel designated as “deep convection” by the 2B-CLDCLASS “cloud_scenario” field [*Wang and Sassen, 2007*]. This criterion is primarily a failsafe, but as Figure 2c shows, object B (red), whose pixels are classified primarily as altostratus, does not satisfy this requirement. Although this criterion only removes about 6% of cloud objects not removed by the other filters, we have observed that it preferentially removes cloud objects that subjectively do not qualify as mature, deep-convective cloud objects, such as

those resembling object B and those formed by immature convective plumes expanding into pre-existing high clouds.

5. The cloud object-partitioning algorithm must identify an anvil region, and the core-counting algorithm must identify at least one convective core. These criteria eliminate objects D (blue) and C (yellow), respectively, and are described further in the next two sections.

Criteria 1 and 2 both introduce a bias toward the over representation of small objects. However, given the comparatively small size of the clouds to the average continuous sampling length, this bias should be small.

2.2.2. Partitioning Cloud Objects

Deep-convective clouds are those that exhibit several characteristic morphological features, including (i) a convective core typically composed of one or more updraft regions with heavy, convective rain that translates through the freezing level and (ii) a horizontally spreading anvil, composed of glaciated and super-cooled liquid hydrometeors, that may or may not be raining. We have found these and other morphological features to be readily identifiable in CloudSat profiles and have developed and implemented two algorithms to define such features within our data set in order to generate useful information about their spatial, thermodynamic, and radiative characteristics.

The first algorithm, described here, partitions deep-convective cloud objects into upper “anvil” and lower “pedestal” regions (so that the anvil rests on the pedestal) (Fig. II.4a). A single deep-convective cloud object, as defined by the criteria in section 2.2.1, may contain multiple convective core regions. We introduce the term “pedestal,” which encompasses everything below the anvil, for precision of terminology. The second algorithm, described in section 2.2.3, estimates the number of “convective cores” within each cloud object’s pedestal.

The goal of the cloud-object partitioning algorithm is to identify a cutoff height for each cloud object. All cloudy pixels above the cutoff height will be considered part of the anvil region and all cloudy pixels below the cutoff height will be considered part of the pedestal region. An object-by-object approach provides two advantages over one that applies a single height cutoff to all objects: first, it yields improved anvil property estimates by adjusting to each individual cloud objects' morphology; second, it yields a new metric, lower-anvil height, that can be used to generate statistics about the lowest height at which detrainment occurs in various regimes.

The cloud-object partitioning algorithm determines a pedestal-anvil cutoff height for each cloud object according to the profile of the number of cloudy pixels identified in each of the cloud object's vertical levels. This metric captures characteristic changes in cloud width at different vertical levels. We define a cloudy-pixels-per-row profile $P_n(k)$ for the n th object,

$$P_n(k) = \sum_{j_{n,k}} C(j, k), \quad (1)$$

where $j_{n,k}$ are the horizontal indices contained in the k th vertical level of the n th cloud object. Figure II.4a and b illustrates this process for objects A, for which an anvil is identified, and D, for which no anvil is identified. In the top panels, the binary cloud object is shown; in the middle panels, the vertical profiles of $P_A(k)$ and $P_D(k)$ are shown. Note that the standard CloudSat vertical index increases with decreasing height; for example, $k = 80$ corresponds to an average height of 6 km, while $k = 105$ corresponds roughly to sea level. Inspection of the cloudy-pixels-per-row profiles corresponding to several mature deep-convective cloud objects reveals a characteristic positive curvature in $P_n(k)$, or a dramatic increase in the *rate* of object widening with height, as anvil transitions to pedestal. In essence, the cloud-object partitioning algorithm identifies the height at which this transition occurs by locating this characteristic curvature in

$P_n(k)$. After computing $P_n(k)$, we smooth the profile three times by repeatedly applying a moving-average filter with a span of eight. Three passes leaves the characteristic shape of the profile while sufficiently eliminating undesirable noise which would otherwise trap our attempts to numerically find the cutoff height. The first and second derivatives with respect to index k of $P_n(k)$, $P_n'(k)$ and $P_n''(k)$ respectively are then computed. The cutoff index, k_{cutoff} , is determined by computing a weighted average of the indices k for which $P_n''(k)$ is positive,

$$k_{\text{cutoff}} = \frac{\sum_{k=k_{\min}}^{k_{\max}} k \cdot P_n''(k) \left[P_n''(k) > 0 \right]}{\sum_{k=k_{\min}}^{k_{\max}} P_n''(k) \left[P_n''(k) > 0 \right]}, \quad (2)$$

where k_{\min} is the minimum vertical index such that $P_n'(k) < 0$, and where k_{\max} equals 85 (see below). The Iverson brackets (square braces in equation [2]) obtain a value of one if the condition inside the brackets is true and zero otherwise. For example, the summation in equation [2] is conducted over the entire unshaded region of Fig. II.4c, but only the data from $k = 70$ to $k = 85$ contribute. The value of k_{\min} is chosen so that any detected positive curvature at upper levels coincides with narrowing from anvil to pedestal. The value of k_{\max} corresponds to a height of approximately 4.8 km and was chosen to prevent positive curvature in $P_n(k)$ near cloud base from affecting the computed cutoff height. Note that for some cloud objects, such as object D, $P_n(k)$ increases monotonically (i.e., the cloud only widens) as k increases from 1 to 85, which leaves k_{\min} undefined (hence the lack of unshaded region in the right-hand side of Fig. II.4c) and prevents the use of equation [2] to compute k_{cutoff} . By virtue of their lack of any narrowing from anvil to pedestal, these cloud objects are unlikely to have reached maturity (i.e., have a well-defined anvil) and are therefore removed from the data set.

Profile smoothness decreases with each level of differentiation, and we have observed that the amount of smoothing required to obtain useful $P_n''(k)$ profiles varies among cloud objects. In order to account for this diversity, two additional calculations of the cutoff index are performed: one with two rounds of moving-average smoothing ($k_{\text{cutoff}2}$) and one with four rounds of moving-average smoothing ($k_{\text{cutoff}4}$). For these calculations, k_{min} is still determined using the $P_n'(k)$ profile calculated with three rounds of moving-average smoothing. If none of these calculations result in the cloud object's removal from the data set, we use these in addition to the previously-computed cutoff index, which we will now call $k_{\text{cutoff}3}$, to compute a final cutoff index,

$$k_{\text{cutoff}} = \frac{k_{\text{cutoff}2} + 2 \cdot k_{\text{cutoff}3} + k_{\text{cutoff}4}}{4}. \quad (3)$$

All cloudy pixels with vertical index greater than k_{cutoff} are designated “pedestal,” and all cloudy pixels with vertical index less than or equal to k_{cutoff} are designated “anvil.” Subjectively from Fig. II.4, it can be seen that this method works. For object A, a subjective guess of the anvil cutoff height might be level 75. Equation [3] assesses that the level is 76 which is certainly consistent with the subjective guess. In fact, the cutoff algorithm exhibits remarkable skill compared to subjective analyses across a large number of objects. Cloud Objects for which the cutoff algorithm fails to yield a useful measure are removed from the dataset. This occurs infrequently

2.2.3. Counting Convective Cores

After each cloud object is partitioned into its anvil and pedestal regions, a second algorithm is used to estimate the number of convective cores within the pedestal region of each cloud object. This is the stage of our analysis with potentially the least skill. In theory, convective cores would be best defined as regions of strong vertical ascent within cloud objects'

pedestal regions [LeMone and Zipser, 1980]. However, neither the A-Train satellites nor any reanalysis data provides the high-resolution spatio-temporal vertical velocity information necessary to identify convective cores according to this definition. Instead, we use relative CloudSat-derived radar reflectivity as a proxy for comparative convective vigor and operationally define convective cores as, essentially, along-track local maxima in reflectivity. While radar reflectivity is an imperfect proxy for convective vigor, it has been found to be useful here in estimating the number of convective cores in a given cloud object's pedestal region, which is the sole objective of the core-counting algorithm. Use of such a reflectivity proxy is not without precedent [Houze, 1993; Yuter et al., 2005, Luo et al, 2008].

The core-counting algorithm examines the reflectivity profiles at the 15 lower vertical levels from $k = 85$ (approximately 4.8 km height) to $k = 99$ (approximately 1.4 km height). Each of these vertical levels will contain at least one cloudy pixel due to earlier filtering by vertical extent, and these vertical levels will all lie within the pedestal region due to the earlier restriction on cutoff-height. We begin by obtaining a snapshot of radar reflectivity at vertical levels $85 \leq k \leq 99$ and horizontal indices $j_{\min} \leq j \leq j_{\max}$, where j_{\min} and j_{\max} are the horizontal indices of the leftmost and rightmost cloudy pixels, respectively, present in vertical levels 85 through 99. The value of radar reflectivity at clear (non-cloudy) pixels is set to -28 dBZ, and the radar reflectivity snapshot is smoothed by twice convolving it with a 2×2 -pixel averaging filter, which adjusts the reflectivity at each pixel in dBZ units, $Z(j,k)$, based on the reflectivity values at neighboring pixels:

$$Z_{\text{smoothed}}(j,k) = \frac{4 \cdot Z(j,k) + 2 \cdot \sum Z_{\text{directly adjacent}} + \sum Z_{\text{diagonally adjacent}}}{16}. \quad (4)$$

The reflectivity snapshot may contain local reflectivity maxima that are associated with immature convective plumes rather than convective core regions that feed into the cloud object's

anvil. As Figures II.2 and II.3 show, object A (green) contains one of these plumes just north of 21°N, and object E contains two of these plumes just south of 13°N. In order to prevent these immature plumes from affecting the count of convective cores, we remove from the pedestal analysis any column within the cloud object that either contains no cloudy pixels with vertical index greater than or equal to 99 or contains more than three non-cloudy pixels between vertical levels 66 and 99. In this way, continuous or near-continuous vertical coverage is ensured through about 9.4 km among columns that are included, which we term “valid” columns. We further remove any isolated sets (termed “islands”) of three or fewer consecutive valid columns fitting the above criteria from the pedestal analysis. If no valid columns remain, we remove the cloud object from the data set. Object C is removed on this basis; this object is likely to be an immature plume convecting into a pre-existing anvil. Unfortunately, this computationally necessary step sets an artificial minimum pedestal width (w_p next section) of 4.3 km. Figure 5a highlights the reflectivity snapshot for valid columns of object A, for which the core-counting algorithm identifies eight cores.

The smoothed radar reflectivity field corresponding to each island of four or more consecutive valid columns is then examined in order to estimate the number of convective cores contained in the entire pedestal region. For each island, we follow the following procedure:

1. Locate maxima (including those occurring on pedestal edges) with reflectivity of at least 0 dBZ at each vertical level. If no local maxima meet this criterion at a given level, record a value of zero cores at that level. Maxima in object A meeting this criterion are indicated in white in Fig. II.5a and with white-filled triangles in Fig. II.5b.
2. If there are at least two maxima at a given level, count the number of non-edge local minima such that the difference between the reflectivity at the minimum and the maximum

of the reflectivities at its adjacent maxima is at least 2.5 dBZ. Add the number of minima satisfying this criterion to the previously recorded value (in 1) for the number of cores at that level and divide by two. Minima in object A meeting this criterion are indicated in black in Fig. II.5a and with black-filled triangles in Fig. II.5b.

3. If a value of zero cores has been recorded at one or more levels, return to step 1 and decrease the reflectivity threshold for local maxima by 1 dBZ (down to a minimum of -10 dBZ if necessary). This tuning of the reflectivity threshold allows us to account for varying amounts of attenuation while preventing weak local maxima from being counted as cores.

4. Take the median of the number of cores recorded across each level, excluding levels for which no core was reported. Fig. II.5b illustrates how the number of cores recorded for object A varies with vertical level. If no cores are reported at any level, record a value of 1 so that each island is determined to contain at least one convective core.

The total number of convective cores in a given cloud object's pedestal region is estimated by summing the numbers of convective cores identified within each island of valid columns. This final step is unnecessary for object A, which has only one island of valid columns. For object A, we obtain an estimate of eight cores from the approach described. This estimate agrees reasonably well with the estimate of 8 or 9 cores that would be obtained subjectively. It should be reiterated that our core-counting algorithm is based on the assumption that the degree of inhomogeneity in the reflectivity field of the pedestal is indicative of the number of convective elements. As such, this algorithm is used to provide an order-of-magnitude estimate of the number of cores, rather than a precise measure of their location.

2.2.4. Defining Morphological Attributes

Once likely deep-convective cloud objects over tropical oceans have been identified and partitioned according to the methods delineated above, information on the morphology of cloud objects are recorded. In particular, we are interested in determining the characteristic pedestal width (w_p), anvil width (w_a), pedestal depth (D_p), and anvil depth (D_a). The height of cloud base (H_{cb}), cloud-top height (H_t), and anvil-pedestal cutoff height (H_{cutoff}) are also recorded. This choice of length scales and variable names in part follows that of *Bacmeister and Stephens* [2011]. Indeed, our definitions of H_{cb} and H_t , the heights of the lowest and highest pixels within a given cloud object, are identical to those of *Bacmeister and Stephens* [2011]. In order to compute H_{cutoff} , the average height corresponding to cutoff index k_{cutoff} (which is rarely an integer) is estimated by interpolating between the average heights of cloud object pixels at the vertical levels immediately above and below the cutoff. From these heights we calculate pedestal depth,

$$D_p = H_{\text{cutoff}} - H_{cb}, \quad (5)$$

and anvil depth,

$$D_a = H_t - H_{\text{cutoff}}. \quad (6)$$

We depart somewhat from *Bacmeister and Stephens* [2011] in our definitions of widths in order to capture the relationship between anvils and their corresponding convective cores in such a manner that only those pedestal regions that feed mass into the anvil are included while associated immature convection is excluded. Pedestal width (w_p) is determined by multiplying the horizontal spacing, 1079 m, by the number of valid columns identified as in the previous section. In this way, columns corresponding to likely immature convection (as well as islands of three or fewer “valid” columns) are removed from the calculation. Anvil width (w_a) is

determined by multiplying the horizontal spacing by the number of columns containing at least one cloudy “anvil” pixel, as defined in section 2.2.2. Note that columns that were removed in the calculation of pedestal width are included in the calculation of anvil width, as well as in the calculations of the heights and depths discussed above. Finally, based on these widths, a detrainment index, I_d , is defined in the manner of *Bacmeister and Stephens* [2011],

$$I_d = \frac{w_a}{w_p}. \quad (7)$$

I_d can be used to imply the relative maturity of a cloud object. Mature storms should exhibit spreading, wide anvils overtop their pedestals and thus, high I_d .

2.2.5. Defining Environmental Characteristics

In addition to recording information about each cloud object’s spatial attributes, information about the environment in which each cloud object resides is also recorded. Each cloud object is assigned a single latitude and longitude. These values are determined by averaging the latitudes and longitudes, respectively, of each of the cloud object’s cloudy pixels. Further environmental information is taken from the ECMWF-AUX auxiliary CloudSat data product, which interpolates ECMWF state-variable data to CloudSat data bins [*Partain, 2007*]. The “skin_temperature” field is commonly used to calculate an average sea-surface temperature (SST) for each cloud object. Since we are particularly interested in the temperature of the water fueling the observed convection, this average is computed across the valid columns previously used to calculate pedestal width. ECMWF SST, the “Sea_surface_temperature” field, (mixed layer) values are also included in a similar way.

The ECMWF-AUX product provides information about temperature, pressure, and relative humidity at the bottom and top of each cloud object’s anvil region. A lower-anvil temperature is computed for each cloud object by averaging the analysis temperature values at

pixels in the lowest vertical level within the anvil. Lower-anvil pressure and relative humidity values are assigned similarly, with relative humidity calculated based on ECMWF-AUX “Temperature,” “Pressure,” and “Specific_humidity” fields using the Goff-Gratch equation (<http://cires.colorado.edu/~voemel/vp.html>). Cloud-top temperature is computed by averaging the “Temperature” values at the top cloudy pixel of each anvil column. In order for a column to be included in the average, its top cloudy pixel must have a vertical index $k \leq 63$ (approximately 10.0 km height or greater). In this way, irrelevant temperatures atop immature convective plumes and shallow sections of anvil are omitted from the calculation of the average. Cloud-top pressure is computed in a similar manner. In an effort to provide an environmental, clear air value, cloud-top relative humidity is computed based on values two pixels (480 m) above the top of each column. It should be noted that these environmental values from ECMWF-AUX are interpolations of grid box averages from nearby analysis points. As such, the values appended to the cloud objects represent a mean atmospheric column for the larger environment in which the cloud is embedded.

Lastly, anvil optical depth is estimated from the 2B-TAU [*Polonsky et al*, 2008] product, and ice water content is taken from 2B-CWC-RVOD [*Wood*, 2008]. First, the layer optical depth and ice water content of anvil pixels are summed for each column to give a vertically integrated total optical depth and ice water path for that column’s anvil pixels. Then, the mean and standard deviation of these column totals are recorded. For a sizeable number of anvil columns, layer optical depth values are missing from the raw data; for a smaller number, IWC values are missing. These columns are not included in the calculation of these quantities, and we record the fraction of missing columns for each cloud object, which is sometimes large. From separate analyses assuming ice-only and liquid-only retrievals, the 2B-CWC-RVOD product assigns each

point an ice water content and a liquid water content based on the ECMWF-AUX-derived temperature at that point. The product assigns the ice-only value for temperatures below -20°C , the liquid-only value for temperatures above 0°C , and a linear combination of the two for temperatures between -20°C and 0°C . For simplicity, our analyses make use only of the resulting ice water content field, "RVOD_ice_water_content". Column total heating rates have been added from the 2B-FLXHR [L'Ecuyer et al 2008] product for all cloudy columns. Column rates are summed across all the columns of each object in order to produce a single value for each cloud object.

2.2.6. Post-Processing Thresholding

The steps outlined thus far produce an initial data set containing approximately 26 000 deep-convective tropical cloud objects over a 5 year period. The criteria for inclusion in this data set are intentionally permissive so as to include all cloud objects whose morphological and environmental attributes can be defined according to the methods outlined above. After this initial data set has been created, cloud objects can still be filtered according to geolocation, time of year, or any other morphological or environmental attribute. In the analyses to follow here, we only include cloud objects with $H_t > 11$ km, $I_d > 1.5$, and $298.75 \text{ K} < SST < 303.75 \text{ K}$. These values allow us to target mature, deep convection over an SST range for which there are many objects. The additional restrictions reduce the size of the data set to approximately 22 000 cloud objects, a quantity more than sufficiently large to yield well-collapsed statistics.

2.2.7. Composite Cloud Images

Composite cloud images are constructed as a means of visualizing the properties of subsets of cloud objects within our data set. It is worth stating explicitly that these composites are used only for visualization purposes. While they provide very insightful qualitative

comparisons, they are not intended to provide any quantitative information. Composite cloud images are, in essence, averages of cloud object binary images such as those shown in Figure II.4a, or, equivalently, averages of the binary fields $C(j,k)$ corresponding to each cloud object. The vast nature of our data set allows statistically-meaningful composites to be constructed from subsets containing as little as two percent of the total data. Composite image structures often converge after only half as much data is used to construct them. Here, objects are binned according to lower-anvil height in order to provide validation of the anvil-pedestal cutoff algorithm; in *Chapter III*, cloud objects are binned according to sea-surface temperature in order to evaluate proposed cloud-radiative climate feedbacks.

As is the case when counting cores, we wish to prevent immature convective plumes attached to mature cloud objects from unduly influencing composite images. However, if “column validity” information is used to remove these plumes, as was the case when counting cores, the question arises, at what vertical level does the plume terminate? We do not wish to remove anvil pixels, and if we simply assume that plumes terminate at lower-anvil height, the resulting composite images will be unsuitable for use in validating the pedestal-anvil cutoff algorithm due to bias caused by this assumption. This issue is addressed by using classifications from the 2B-CLDCLASS “cloud_scenario” field instead. The cloudy pixels making up the convective pedestal regions that feed into the anvil and the cloudy pixels making up the anvil, are those classified as either cirrus (1), altostratus (2), or deep convection (8). Pixels we do not want to include are those classified either as altocumulus (3), stratocumulus (5), cumulus (6), or in rare cases, stratus (4). Figure II.3c illustrates the relevance of the prior and irrelevance of the latter for object E. *Young et al.* [2013] show complimentary results. Thus, the first step in constructing composite cloud images is to eliminate pixels with a “cloud_scenario” value other

than 1, 2, or 8. The images are then aligned according to the average horizontal index of remaining cloudy pixels present in vertical levels 85 through 99. Images are then averaged together, with clear pixels assigned a value of 0 and cloudy pixels assigned a value of 1. Finally, a color scale is applied and the values of all pixels valued below 0.10 are set to zero (black) to accentuate the 0.10 contour. It is important to note that due to the alignment step of the compositing process and diversity of cloud object shapes, these plots always result in what appears to be a single-core-like object.

Figure II.6 shows composite images generated from single-core and double-core clouds (as determined by the core-counting algorithm) for various ranges of lower-anvil heights (as determined by the pedestal-anvil cutoff algorithm). Each image is made up of approximately 1800 cloud objects. The composite anvils do, in fact, appear to detrain higher in the cloud as the cutoff height is increased. Furthermore, each binned cutoff height (highlighted) appears to match the height of the transition from pedestal to anvil in its corresponding composite image. Finally, it should be noted that the concave structure at the highest percentages in Fig. II.6d near the cutoff height is due primarily to increasing inhomogeneity in cloud object structure with increasing cutoff height. Figure 6 therefore exemplifies the utility of this visualization tool, one of simple qualitative assessment.

3. Data Validation

This section includes a discussion of the spatial and temporal frequency distributions of cloud object occurrence (i.e. cloud object number densities). These distributions will be compared to results that have been obtained in previous studies. It is noted that prior studies have examined cloud fraction, which is not a precisely equivalent metric to frequency of deep

convective cloud object occurrence since the objects used herein are very specifically selected. Nevertheless, it will be shown that the data set developed in the previous section has realistic distributions of cloud objects across space and time, and it will be suggested that the data set does not need additional spatial or temporal thresholds. While subtle differences between the developed data set and past results do occasionally arise, it is evident that none of these are sufficiently significant enough to affect the conclusions drawn in section 4.

3.1 Geospatial Statistics

Various spatial frequency distributions of cloud objects are detailed in this section. Some of the first results are similar to those of *Sassen et al.* [2009] who used 2 years of combined CloudSat and CALIPSO data, but the results shown here arise from a very different data set.

First, the frequency distributions of object centers by latitude is presented in Fig. II.7. The figure illustrates the number of cloud objects deemed to center within a certain 2.5-degree latitude bin. Although, this is not a plot of cloud fraction, common features of cloud fraction plots are exhibited including local maxima at $\sim 8^{\circ}\text{S}$ and $\sim 8^{\circ}\text{N}$ (due to the Inter-Tropical Convergence Zone [ITCZ]), a local minimum at the equator, and a steady decrease in magnitude toward the poleward extent of the tropics. The figure looks similar to previously reported results from both recent global models and observations [*Sassen et al.*, 2009; *Probst et al.*, 2012]. Regional binning and analysis of cloud objects (not shown) indicates that mean cloud sizes are similar among regions. This result agrees with the similarities between the cloud object occurrences presented in Figure II.7 and the ISCCP cloud fraction [*Probst et al.*, 2012], which implies that coverage per cloud object is roughly uniform and therefore that cloud size is similar across regions.

A global, two-dimensional occurrence frequency plot is shown in Fig. II.8 with $2.5^\circ \times 2.5^\circ$ bins. It can be seen that the only ocean regions completely lacking deep tropical convective cloud objects are over the stratocumulus decks off of the western side of continents [Wood, 2012]. While other non-stratocumulus regions may exhibit local minima, they are not bereft of deep convection. Regions frequently within the ITCZ tend to exhibit the highest number density of deep convective cloud objects. Other local maxima in cloud objects exist in the Caribbean and northern tropical Atlantic, the South Pacific Convergence Zone, the Bay of Bengal, the northern tropical Pacific especially just west of Panama, and the southwestern tropical Atlantic. It is therefore evident that deep convective cloud object occurrence is fairly ubiquitous.

Figure II.8 is suggestive of the elimination of cloud objects due to overlaying of land or intersection with the tropical boundary by the methodology developed. In several places, islands (e.g. Hawaii, Indonesia, or Hispaniola) or continent boundaries (e.g. the Yucatan or parts of Australia) can be seen to correlate to local minima or zeros in cloud object count over the ocean near the respective location even though there is no physical reason to expect such a minimum. There is also an interesting lack of cloud objects in the central Pacific along the equator between 100°W and 130°W . This result appears to be the consequence of two factors. The first is a climatological lack of clouds in this region [Liao *et al.*, 1995]. But this probably cannot explain the total lack of cloud objects in some latitude-longitude bins. It could illustrate a problem with the standard thresholds used in this study, although easing some of these thresholds did not generate many more cloud objects in this region. Alternatively, this lack of cloud objects may illustrate a daily sampling bias of CloudSat by which clouds are not vertically developed in this region at 1330 LST. Including the nighttime overpass in the data set could answer this question although Sassen *et al.* [2009] did not notice significant differences between night and day in 2

years of data over the East Pacific. The local minimum could also be due to a lack of strong warm ENSO phase which would tend to enhance cloudiness in this region [e.g. *Klein et al*, 1999].

3.2 Temporal Statistics

The analysis in this section will serve to complement the spatial analysis in the previous one by describing whether the methodology developed above introduces any significant temporal biases. Regionally, tropical convection is observed to undergo significant variability over the course of the year [*Sabin et al.*, 2013]. However, when the tropical oceans are examined as a whole, clouds often do not exhibit much of a seasonal cycle [e.g. *Christian et al*, 2003; *Stubenrauch et al*, 2006]. To confirm this in our data set, Fig. II.9 shows the population of cloud objects divided into 5-day bins. Day 366 of 2008 has been excluded for the sake of symmetry, and data from both the northern and southern hemispheres are included. Actual data from 2006 day 166 to 2011 day 107 are in black bars. White bars show an attempt to account for missing data resulting from CloudSat downtime or missing data by adding an artificial number of objects to each day based on the ratio of observations occurring on that day to the highest number of occurrences on any day (day 225, DOY bin 45). These additions are done to facilitate comparisons using this figure and do not impact the data set in any way. The primary implication drawn from Fig. II.9 is a lack of any strong, tropics-wide yearly cycle in the frequency of cloud object occurrence. The second is that a local, temporal minimum does exist near the beginning of the calendar year. This signal exists across all basins and in both the northern and southern hemispheres. Speculatively, it may be a tropical response to the seasonal progression of the Hadley cell [*Mitchell and Wallace*, 1992], a statistical anomaly, or some minor methodological bias. In the event that it is real, it could imply that during these weeks,

clouds are more efficient rain producers per cloud object given global moisture constraints. Perhaps indicative of such an idea is that clouds are computed to be ~10% wider during the first 25 days of the year than the final 340 which could imply weaker entrainment, but we find little additional evidence to suggest this. Due to high convective activity over tropical land regions at the beginning of the calendar year [e.g. *Peterson and Rutledge, 2001*], subsidence might be enhanced over oceans during this time and convection could be suppressed. Or, the explanation might be that a large population is somehow eluding the database through the selection criteria or, as stated above, by diurnal cycle.

The results in sections 3.1 and 3.2 detail the spatio-temporal occurrence of cloud objects and demonstrate that our intentionally inclusive data set is not biased by such inclusions. Subsetting by time or space could have uses but does not seem to be necessary to understand the physics of deep convective cloud objects. These facts should help to address concerns that examining cloud objects across the tropics with no meteorological subsetting might not be justified. The database will now be used to examine deep convective length scale populations.

4. Theories on Scales

This section will focus on the analysis of cloud object volume populations. These will be analyzed in order to shed light on the fundamental behavior of clouds.

4.1 Scale Populations

Attempting to understand cloud dimension population statistics has been a longstanding endeavor [e.g. *Lovejoy, 1982; Cahalan and Joseph, 1989; Wood and Field, 2011*]. In these studies, it was determined that cloud populations follow a power-law relationship with an exponent near 2. These power-law relationships were formulated across many orders of

magnitude of cloud length scales and cloud types from small cumulus ($O < 1\text{km}$) [*Cahalan and Joseph, 1989*] to expansive stratus decks ($O \sim 10\,000\text{km}$) [*Wood and Field, 2011*]. What is not readily apparent from these analyses is whether such power-law distributions are relevant for deep convective clouds of the type included in this data set. It would certainly seem plausible but is not necessarily expected.

The population statistics of both anvil and pedestal volumes are investigated here in an effort to assess this idea. Specifically, these volumes are examined to see if the scale invariant nature of clouds indicated by these power-laws exists among cloud object different components of the cloud objects. Figure II.10 shows the populations of both anvil and pedestal volumes, V , normalized by the maximum dimension, V_{max} , for which there is still significant power (i.e. for widths of 1250km and 700km for anvils and pedestals, respectively). Volumes are calculated as if clouds were cylinders by converting the measured widths to implied areas assuming objects are circular and using either the base to cutoff height or cutoff height to cloud top to determine depths of pedestals and anvils, respectively. Both curves exhibit an exponential decay in power of some form with approximate power-law scaling factors of 1.8 and 2.0 for anvil and pedestal volumes, respectively, using a simple linear least squares fitting in logarithmic space. When comparing the distributions of pedestals and anvil length scales and from these scaling factors, it becomes apparent that anvils exhibit more heavy tail characteristics. Such heavy tails epitomize power-law distributions [*Clauset et al., 2009*]. In corroboration of the results, *Bacmeister and Stephens* [2011] found power-laws in conceptually similar but somewhat more permissive CloudSat cloud object data down to smaller scales than are examined here. To calculate Fig. II.10, cloud objects were assumed to be circular. This is an imperfect assumption. An

assessment of the impact assumed circularity as it pertains to *Chapter IV* can be found in the appendices therein.

One of the interesting consequences of finding that the distributions of pedestal and anvil sizes obey power-law/exponential relationships, indicating scale invariant behavior, is the implication for the universality of the physics at work within tropical deep convective clouds. To obey such a spectral signature, all the clouds that make up the distribution are likely to be dependent on the same physics and these physics must be occurring across all scales [*Bak et al*, 1987]. To occur across all scales, the particular physics at work must be small-scale (or at least, no larger than the smallest object) which would lead to the hypothesis that they are diabatic, rather than purely conservative Newtonian forces which occur on the cloud as a whole and wouldn't seem to scale in the necessary way. We are led to speculate that microphysical heating processes are responsible for the scale invariant behavior. They occur across all space and time scales and the bigger the cloud gets, the bigger their integrated influence. For example, through a volume integral of latent heating, it is reasonable to imagine that as the cloud grows so too does the magnitude of the forcing. It is especially compelling that differences at the interface of microphysics and macrophysics appear to control the scale invariant behavior of global models in *O'Brien et al*. [2013]. If this concept is true, then studying benign, small, but inherently frequent deep cumulus should reveal most of the relevant processes occurring in larger, more intense, infrequent and difficult to study clouds (due to their size and infrequency). The result is a potentially strong endorsement of the methodology developed above that provides strong statistics of the most frequent clouds. In fact *Chen et al*. [1996] show that clouds such as the ones that exist in large numbers in the data set utilized here were observed on 80% of days during TOGA-COARE. Of course, the implications of this scaling result are also that the

predilection of past studies to focus on MCS and larger scale clouds did not lead to any major biases in their conclusions when extrapolated down to the smaller scales of individual convective turrets. While from a process level, using large-scale results to understand building block physics leaves something to be desired, the power-law relationship suggests that it does not seem inherently wrong in the case of tropical deep convection. Such results could potentially be used to inform model parameterization schemes although suggesting specifically in what way is beyond the scope of this study.

These results do not indicate that the large-scale dynamics play no role in partitioning environments between highly convective MCSs and clear-skies. Rather, the results presented in this chapter might indicate that the role is organizational. For example, the well-known occurrence of convective self-aggregation [Su *et al* 2000] might be thought of as representing a scale invariant response of convection to the large scale. Yuan [2011] attributes similar power-law results to aggregation. The results presented here could be understood to imply that MCSs are constructed of building-block convective cells as indicated by the universality at work. Logically, then, the environment could serve to dictate how the building blocks are organized as in the Stretched Building Blocks of Mapes *et al.* [2006] wherein clouds are seen to exhibit similar life cycles over different spatial scales. Further insight could be gained by analyzing the population statistics of environmental variables thought to correlate to convective activity such as midlevel vertical velocity or convective available potential energy (see Chapter V). It would be informative to know if these environmental quantities scale spatially in similar ways to clouds in order to gauge the control mechanism by the environment. In fact, a robust relationship between the mutual growth of pedestals and anvils can be found that follows a $2/3$ power scaling which is entirely due to the flux of mass within clouds (Chapter IV). This result and its causes

and implications are discussed in detail in Chapter IV. This scaling exists for the mean of cloud objects and when combined with the results herein, perhaps suggests that clouds are deterministic in the mean but any one object might be left to random chance. Clouds would therefore be difficult to predict.

The universality, or applicability to all clouds, of fast, internal, and cumulatively scale invariant physics could also have implications for convective parameterizations. Parameterizations are built fundamentally on definite functions of environmental variables on long time scales compared to the convection [e.g. *Arakawa and Schubert, 1974*]. Such frequent, scale invariant physical processes as are suggested here as being important to clouds would be poorly represented in such formulations. These results, therefore, might suggest that a different approach to parameterization is needed that allows faster feedbacks to occur. A high frequency and high resolution, iterative parameterization would seem warranted. This idea is a recast of the fundamental reasoning behind the multi-scale modeling framework [*Grabowski, 2001; Randall et al., 2003*] which allows a cloud model with its short time step, high resolution, and explicit physics to run.

4.2 RCE Simulation

In addition to the observational investigation of cloud populations, results from a cloud resolving model simulation have been investigated to determine whether similar conclusions can be drawn about the nature of simulated convective distributions. A large-domain (3000x200x25km), high-resolution (1km horizontal grid spacing) tropical, radiative convective equilibrium (RCE) [*Manabe and Strickler, 1964*] simulation with resolved convection has been conducted with the Regional Atmospheric Modeling System (RAMS) [*Cotton et al. 2003; Saleeby and van den Heever, 2013*]. This simulation is integrated for 70 days. Over this time,

fields of clouds evolve free of any large-scale forcing. The simulation is doubly periodic and represents a tropical strip. The gross behavior of this simulation will be the topic of future work. For the present study, it is important to note that the clouds generated in the model exhibit gross characteristics of the tropical panoply of clouds [Posselt *et al.*, 2008, 2012].

Because the RCE simulation is 3-dimensional, the result above that the volume-scale populations appear to exhibit power-law dependence can be tested more completely. Not only can the results be extended to 3 dimensions, but also the results from a large range of cloud types can be examined. The most compelling advantage of the 3-dimensional dataset is the ability to analyze cloud volumes without making any assumptions about shape. In the simulation, gridboxes with total condensate mixing ratios of 0.01g/kg or greater are defined to be cloudy. Contiguous cloudy gridboxes are then aggregated into individual single cloud volumes. No shape selection or other thresholding is done and the population includes different cloud types. Because the model vertical grid spacing is non-uniform, a systematic bias in the minimum observable volume of a cloud is introduced wherein the smallest volume clouds are only observable at low levels.

Figure II.11 shows the population of the volume of clouds for those from one cubic kilometer to 10 000 cubic kilometers which spans volume scales from simulated isolated cumulus clouds to large clusters of deep convection. From the smallest volumes to those of the smaller convective clusters ($\sim 10^{12} \text{ m}^3$), a consistent slope exists in the population distribution indicative of scale invariant behavior. This result suggests that, in the simulation at least, not only do the populations imply scale invariant behavior, but also that the power-law nature of convective clouds continues downscale from deep convection to shallow. This conclusion is an interesting one, as it may have been assumed that the growth of clouds from a population of

shallow to congestus to deep would be more deterministic. Unfortunately, a scale break seems to exist at volumes larger than that of individual deep convection. However, this break may be artificially created by the limited domain size of the RCE simulation. The results of *Neggers et al.* [2003] suggest a similar scale break occurring at much smaller volumes for large-eddy simulation of shallow convection on a much smaller domain. In the real world, the scale break probably occurs beyond the Rossby radius where the flow can be readily deformed by the Coriolis force. So just like in the length scale analysis done with CloudSat, the results of the RCE simulation suggest that studying the more-frequent, isolated deep convection should be considered as an avenue for understanding the larger, less frequent but still deep clouds, and they stand as a compelling reflection of the observational results. In the future, a specially designed set of parameterizations could be used in the RCE framework to see if replacing current diabatic physics with some that do not scale with cloud size would introduce non-power-law behavior, although what these would be is not obvious.

5. Conclusions

A methodology to divide CloudSat data into individual cloudy regions (termed cloud objects) that exhibit certain shape and internal characteristics has been developed. Cloud objects were defined to be deep convection based on height, CloudSat cloud-type identification, and contiguity. A method for separating the cloud object into anvil and pedestal (on which the anvil sits) regions was developed. This method relied on a characteristic change in the vertical gradient of horizontal width. Additionally, an attempt was made to count the number of convective cores within each pedestal region, with some success. A composite image technique

was also introduced. The population of cloud objects was shown to exhibit minimal potential bias in their distribution in space or time.

A number of examples of the utility of the cloud object methodology developed herein have been shown. Among the results obtained are that cloud object populations are seen to exhibit a power-law like behavior. Results from a radiative-convective equilibrium model broadly suggest similar behavior in a large-domain simulation. Understanding that clouds exhibit this kind of behavior is crucial to understanding the processes that govern clouds. The population distribution was taken to imply that the many small scale physics occurring rapidly during a the lifetime of a cloud act in concert to force cloud growth. This result was also taken to imply that physical insight gained from one studying one convective cloud can easily be applied to another even if they differ greatly in size. Additionally, the geospatial and temporal distributions of cloud objects were analyzed. As would be expected for an unbiased dataset, it was found that deep convective cloud objects as defined by this methodology exist across the tropical oceans except in regions of stratocumulus, and that the seasonal variability in their occurrence is likely negligible except for a curious decrease in cloud number near the beginning of the calendar year. The ubiquity of cloud objects will be crucial to the following chapters.

Finally, based on some of the above results, it was suggested that common convective parameterization techniques that act as diagnostic functions might be fundamentally inadequate to modeling tropical deep convection. Deep convective cloud objects seem to grow at the mercy of internal, individually small scale but cumulatively scale invariant diabatic physics. As such, any individual cloud could be slaved to its internal, micro-scale processes that occur at many orders of magnitude smaller scales than the cloud itself but which helpfully seem to scale cumulatively with cloud size. Such a cloud would *not* be fated entirely by its initial conditions.

Its nurture would be more important than its nature [*Romps and Kuang, 2010*]. This result could explain why it is so difficult to link any individual cloud to its large-scale environment.

However, it would make intuitive sense if the cloud objects were themselves organized by the large-scale. This would retain a role for both internal and external dynamics, while satisfying the implied results that cloud scales are the result of iterative and numerous internal physical processes.

6. Figures

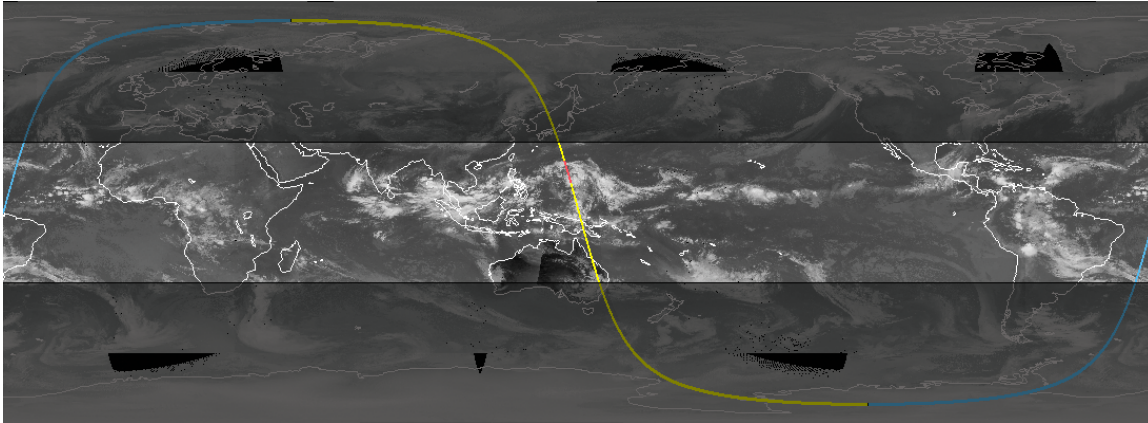


Figure II.1: The orbital path for CloudSat granule 7919, obtained on 24 October 2007, superimposed on global infrared satellite imagery. The orbital path proceeds from right to left, with a nighttime (blue path) equator crossing over the Atlantic Ocean, a daytime (yellow path) equator crossing in the western Pacific Ocean, and a nighttime equator crossing over South America. The tropics, defined as $30^{\circ}\text{S} - 30^{\circ}\text{N}$, are highlighted. The data for the next several figures are taken from the red section of the path.

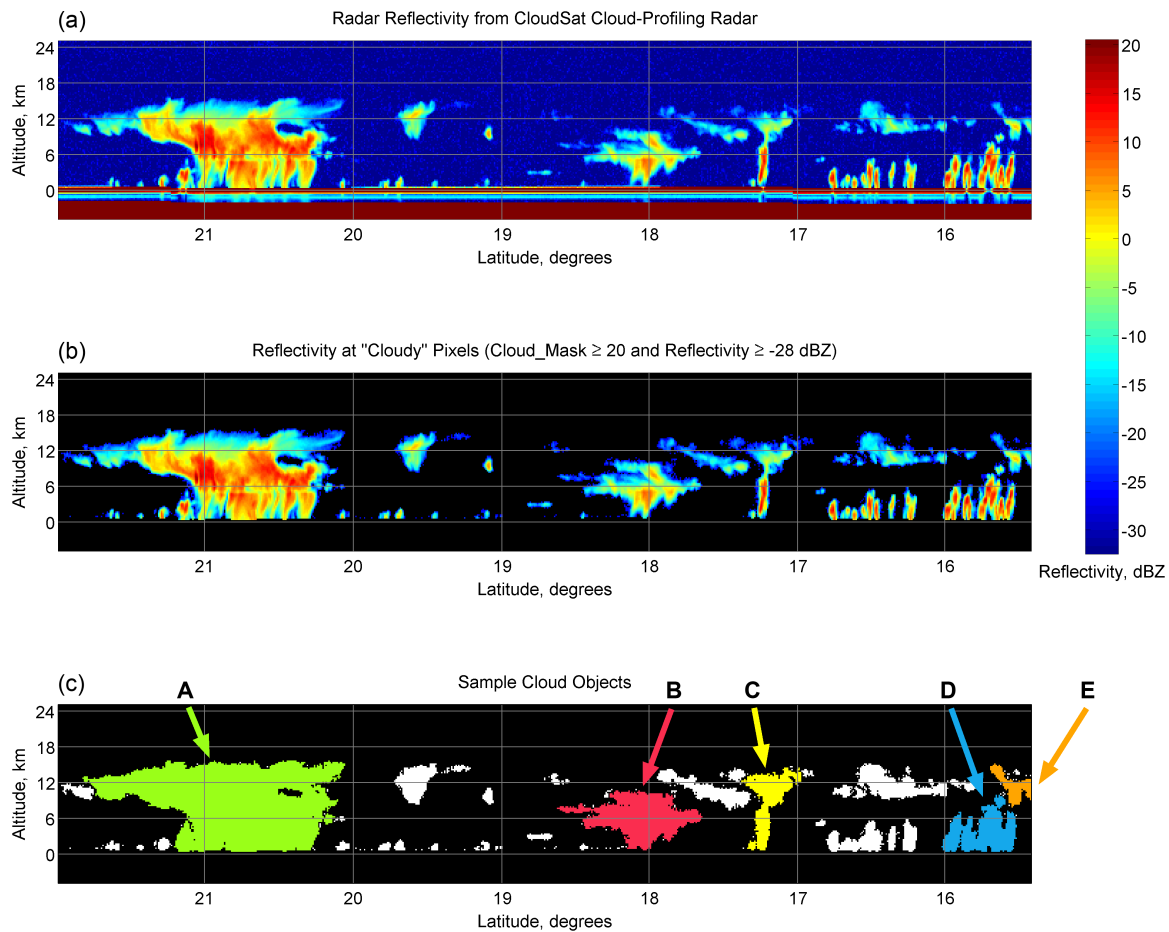


Figure II.2: Partial daytime tropical retrieval from CloudSat granule 7919 (shown in Figure II.1). (a) The 2B-GEOPROF “Radar_Reflectivity” field. (b) Same as (a), but with “clear” pixels colored black. (c) Cloud objects within the retrieval. Cloud objects meeting basic vertical extent requirements are colored and labeled for reference within our discussion. A more complete view of object E (orange) is provided in Fig. II.3.

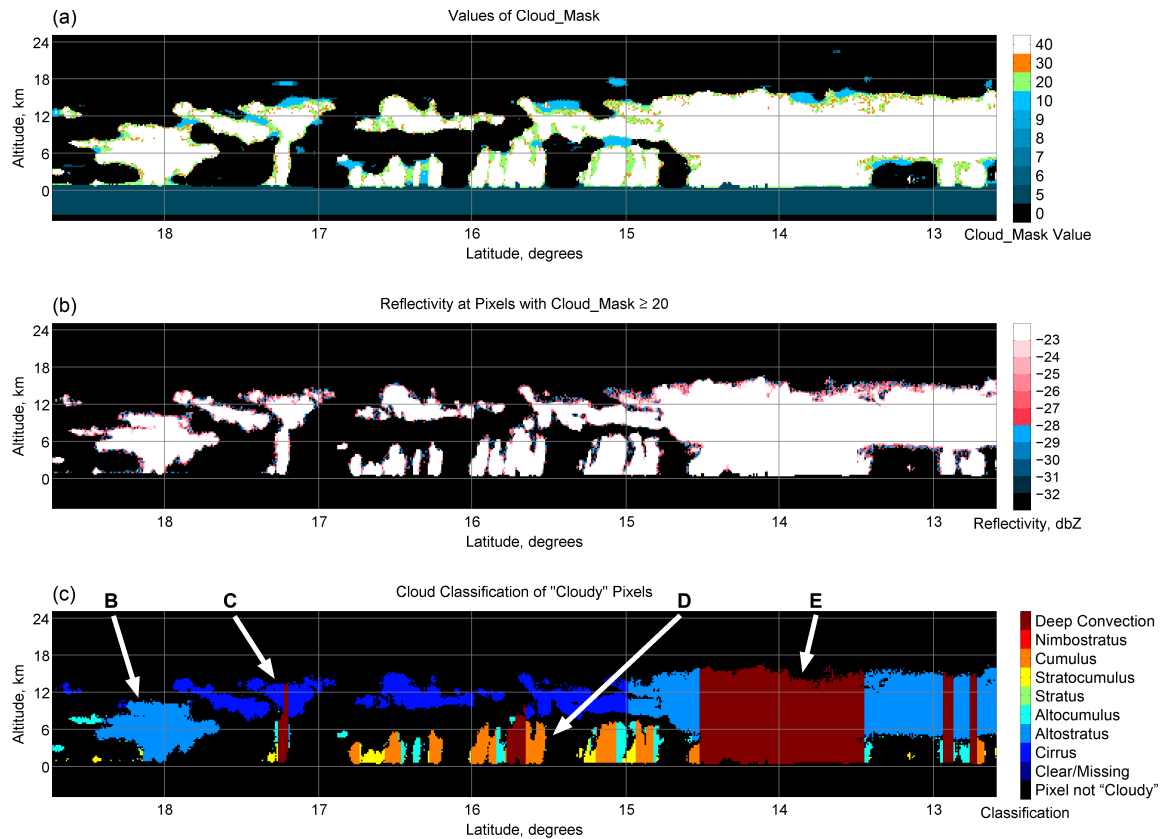


Figure II.3: Illustration of various filtering mechanisms and thresholds. Note the overlap between this scene and that shown in Fig. II.2. (a) The 2B-GEOPROF “CPR_Cloud_mask” field. By our choice of threshold, pixels with values of 20, 30, and 40 are retained. (b) Same as part (b) of Fig. II.2, with color scale modified to emphasize pixels with low reflectivity. By our choice of threshold, pixels with reflectivities of at least -28 dBZ_e (shown in red) are retained. (c) Values of the 2B-CLDCLASS “cloud-scenario” field for “cloudy” pixels.

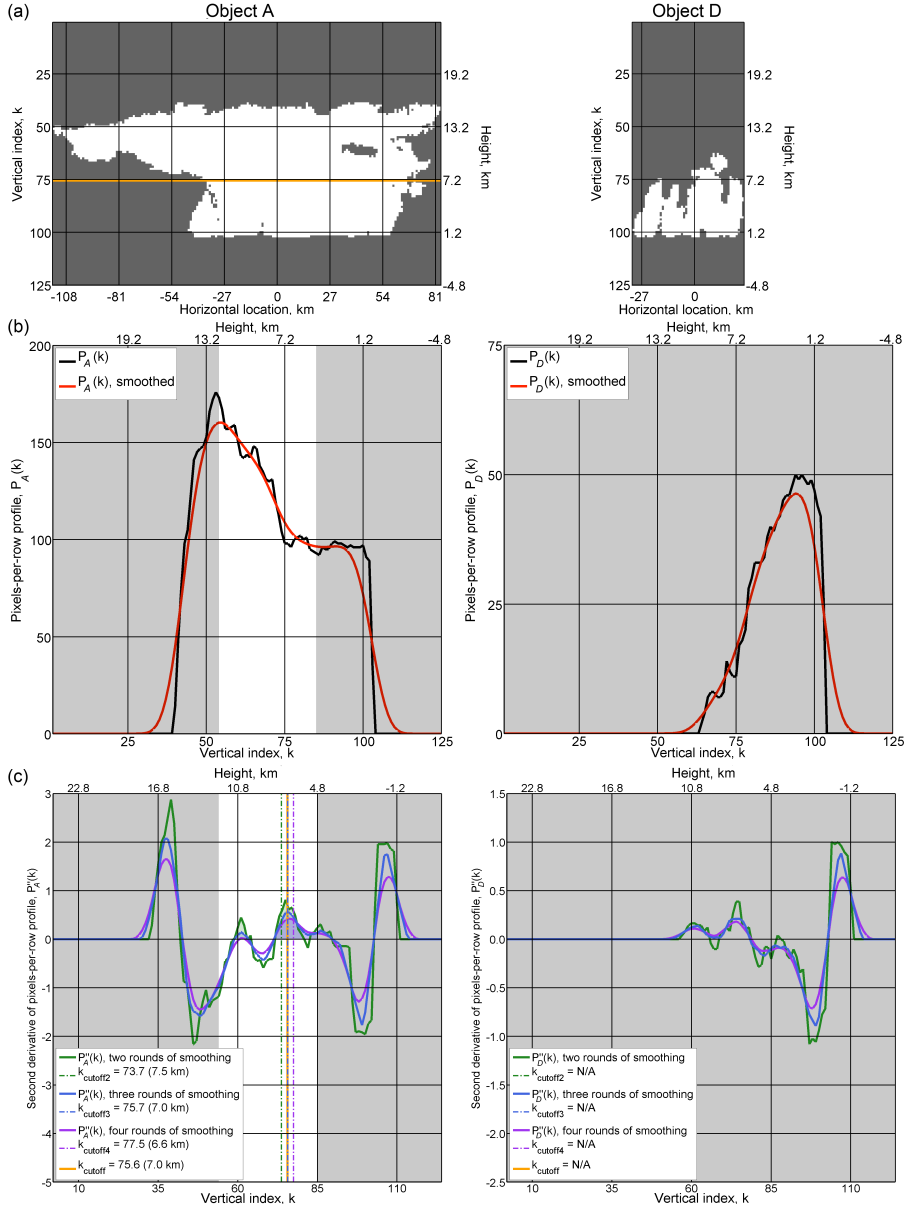


Figure II.4: Illustration of cloud-object partitioning algorithm for object A, for which an anvil is identified, and object D, for which no anvil is identified. (a) Images of objects A and D. (b) Cloudy-pixels-per-row profiles $P_A(k)$ and $P_D(k)$ before and after smoothing. $P_A'(k)$ becomes negative as anvil begins narrowing to pedestal, whereas $P_D'(k)$ does not become negative until cloud base. (c) As the anvil completes the transition to pedestal, $P_A'(k)$ approaches zero, and $P_A''(k)$ becomes positive. The partitioning algorithm identifies a cutoff by searching the unshaded region, starting where $P_A'(k)$ becomes negative and ending at $k = 85$, for regions where $P_A''(k)$ is positive. The solid lines show the profile of width with various levels of smoothing and the dashed lines the corresponding cutoff height. The orange line illustrates the final cutoff height for the object in (a) and (c) for object A. For object D, there exists no unshaded region to search, and so the algorithm does not identify a cutoff.

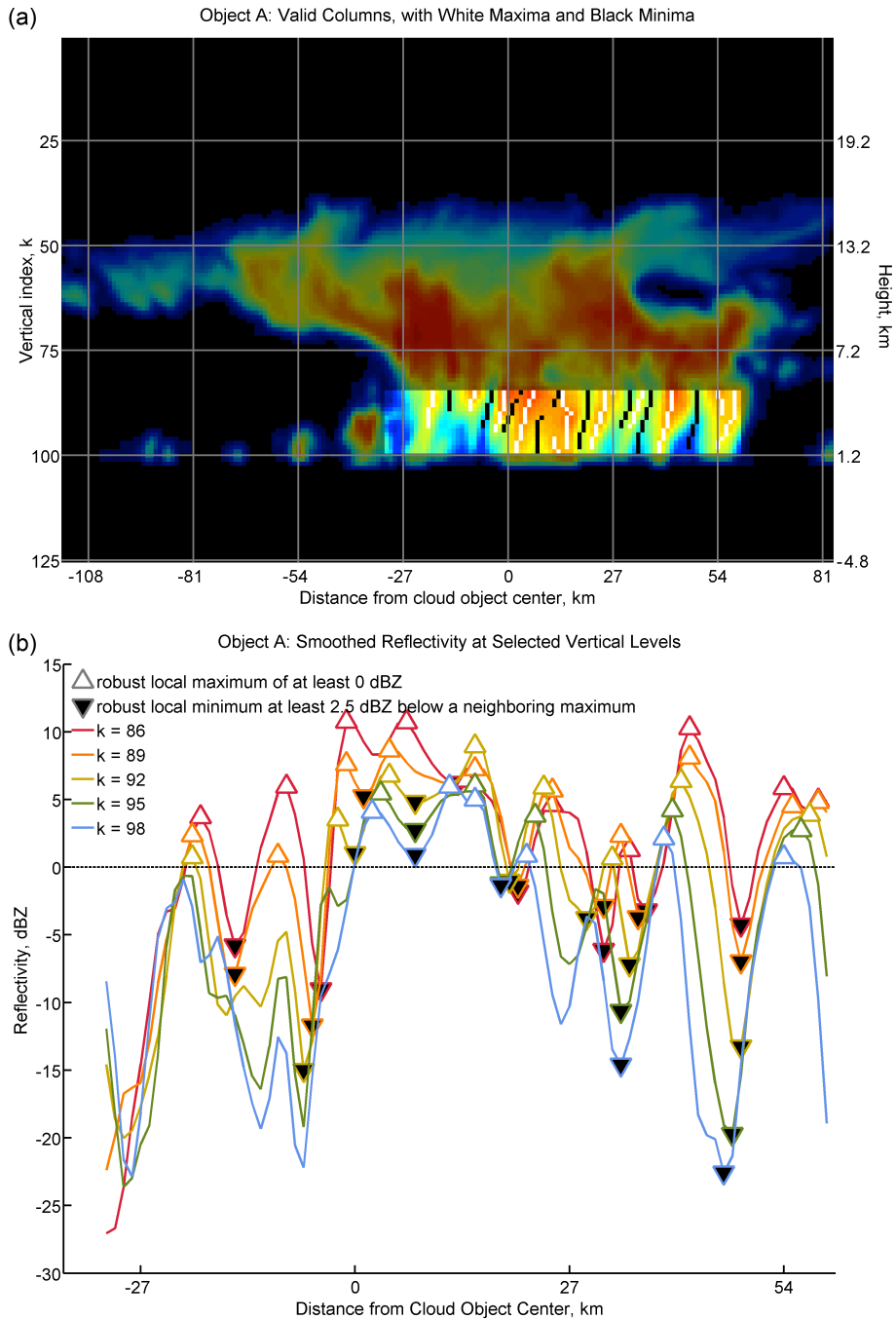


Figure II.5: Illustration of core-counting algorithm for object A, for which eight cores are counted. (a) Reflectivity image of object A after smoothing is applied. Vertical levels 85 through 99 of “valid” columns are highlighted. The immature convective plume on the left edge of the pedestal is eliminated by column validity requirements. The robust local maxima and minima used to count cores are colored white and black, respectively. (b) Reflectivity at five vertical levels within the region highlighted in (a).

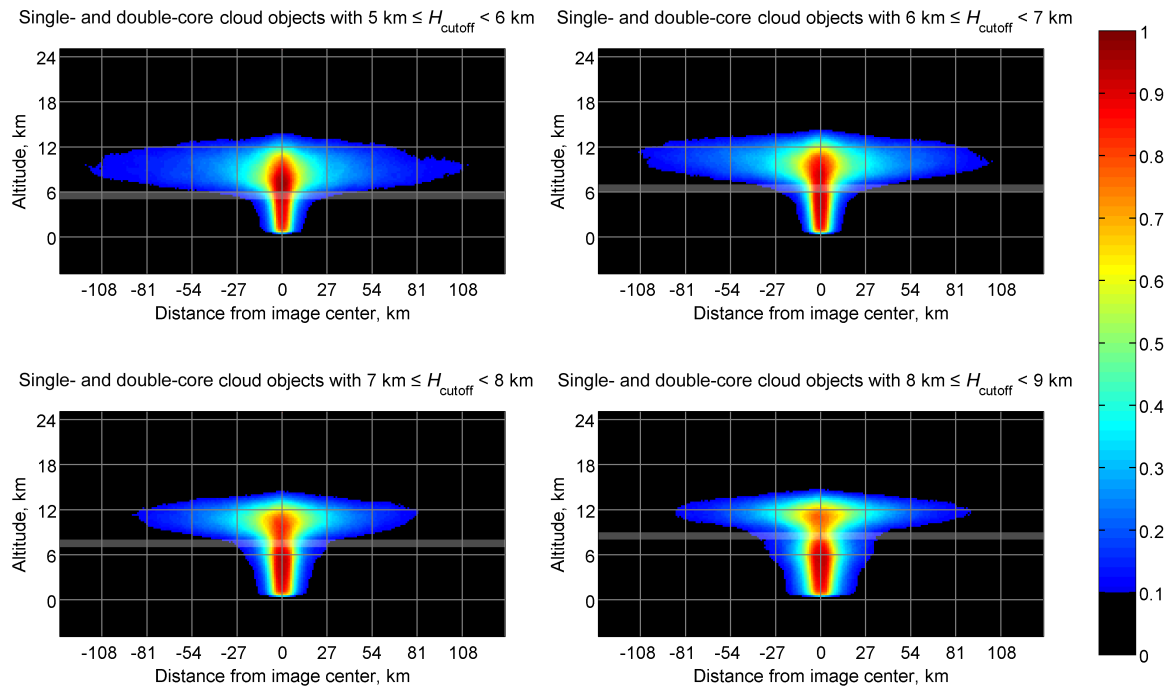


Figure II.6: Composite cloud images of single- and double-core cloud objects for four ranges (highlighted on the images) of lower-anvil heights. The shading represents the fraction of clouds that would overlap if cloud base centers were collocated.

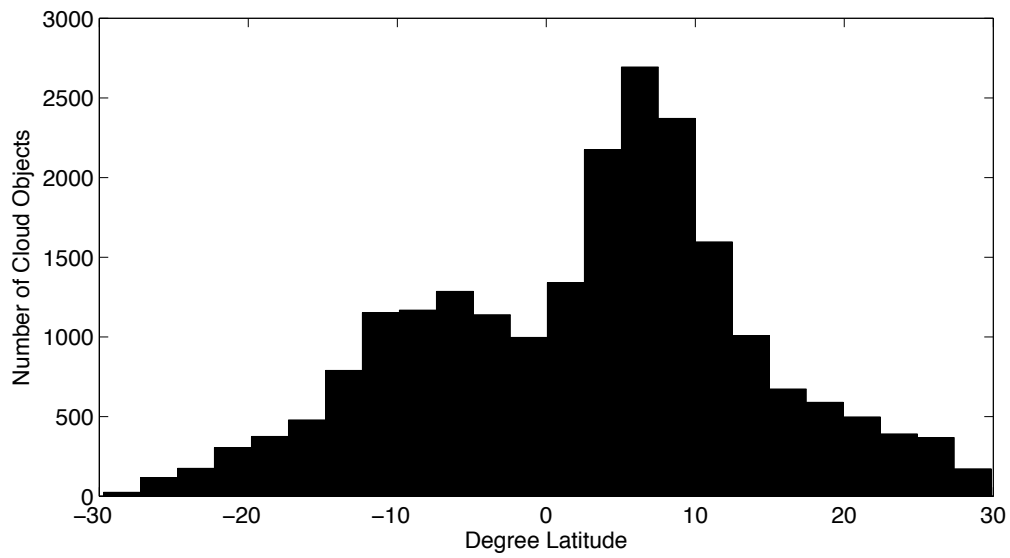


Figure II.7: Population of cloud objects binned by latitude. Bins are 2.5° wide.

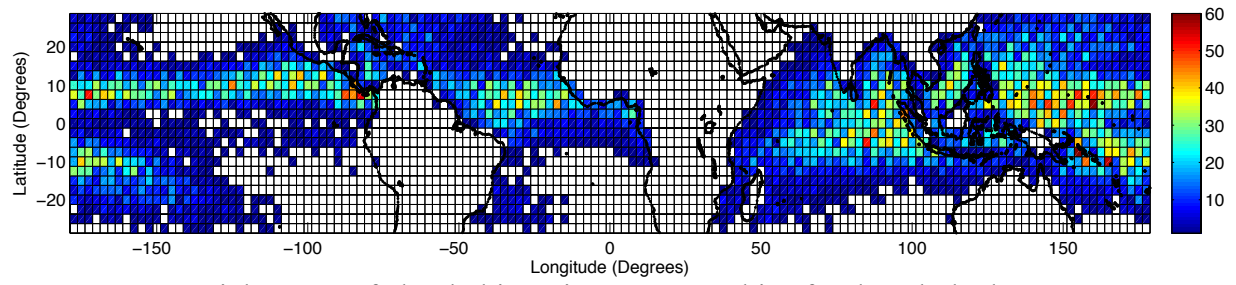


Figure II.8: Spatial counts of cloud objects in $2.5^\circ \times 2.5^\circ$ bins for the whole dataset.

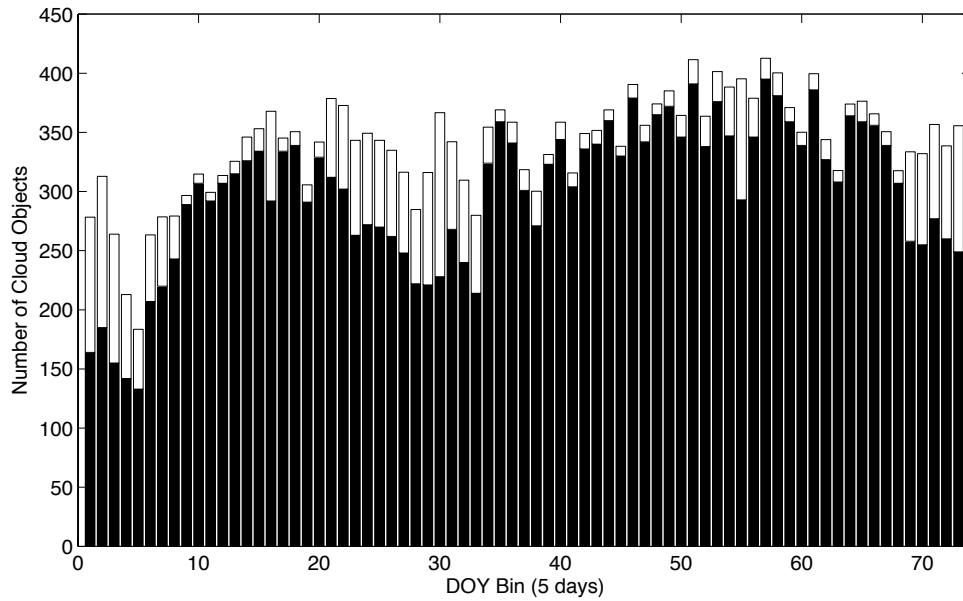


Figure II.9: Temporal population density of cloud objects. Bins are 5 days wide and begin on January 1. White bars represent an artificial addition of data to account for CloudSat operational date non-uniformity and other missing data. Data includes northern and southern hemisphere cloud objects

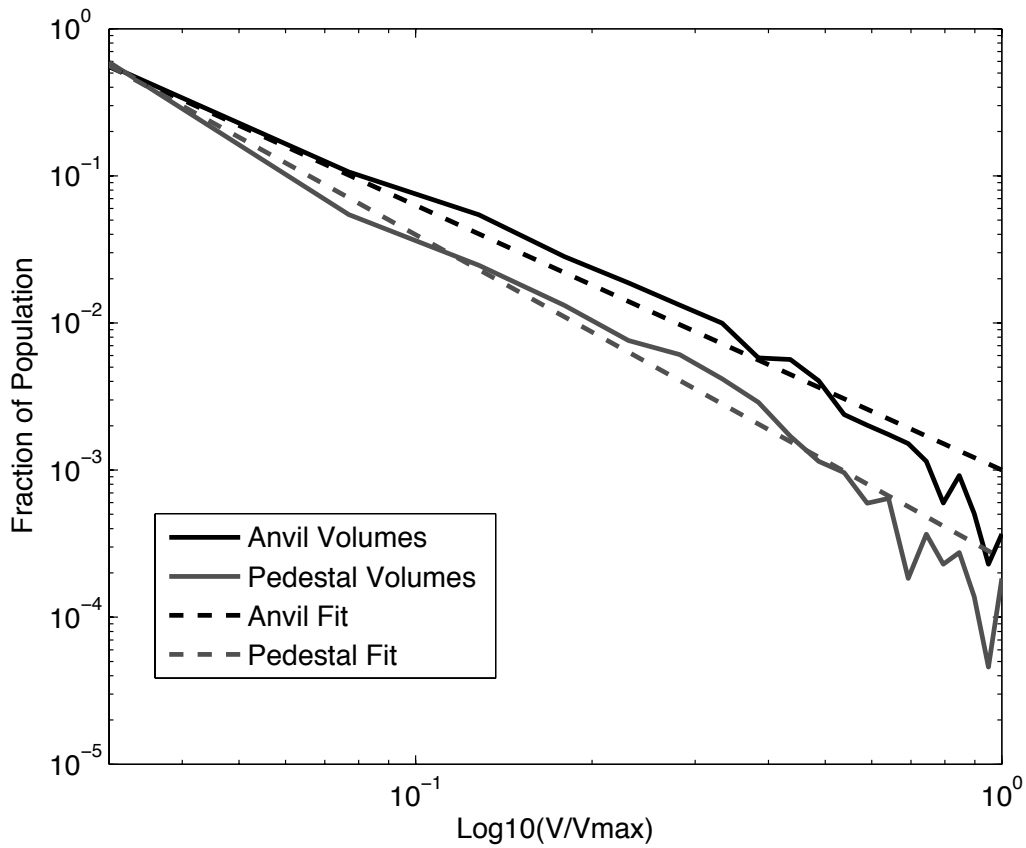


Figure II.10: Populations of volumes scaled by a maximum value for anvils in black and pedestals in grey (solid lines). The power-law fits are shown in the dashed lines.

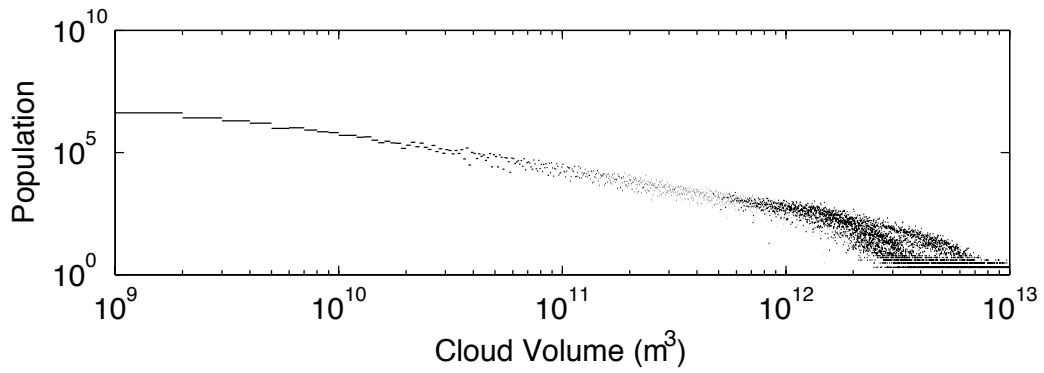


Figure II.11: Population of contiguous-cloud volumes from the RAMS simulation ranging from volumes of 1 km³ (10⁹ m³) to 10 000 km³ (10¹³ m³).

CHAPTER III: ASSESSMENT AND INTEGRATION OF DEEP CONVECTIVE ANVIL- CLIMATE FEEDBACKS

1. Introduction

The development of the cloud object identification algorithm in *Chapter II* was done in particular anticipation of *Chapter III*. Herein, trends in cloud object properties are examined with respect to a pseudo-climate variable. This begins the investigation of the controls of the size and shape of tropical deep convection at the largest possible space-time scale.

Convective clouds are perhaps the most easily observed aspect of the tropical atmospheric system by the layman. But thorough, scientific observation of convective clouds is difficult. Clouds are frequent over ocean, away from ground-based observation systems; they occur across a wide range of length scales, creating difficulty for models; and scientifically defining precisely what is and what is not a cloud remains an elusive goal. Little literature exists on the range of scales over which tropical convection tends to occur, yet if predictions of climate change are to be made more accurate, some knowledge of these scales, the manner in which they interact, and the ways in which they might change with warming is imperative [*Stephens, 2005*]. Some of the most crucial climate impacts of clouds cannot be understood without knowledge of their physical length scales [*Bony et al., 2006*]. The height, and therefore cloud-top temperature, of deep convective clouds dictates the net amount of radiation emitted from the climate system (in cloudy regions) at the top of the atmosphere to space and consequently the amount absorbed by the atmosphere [*Manabe and Strickler, 1964*]. Likewise, the depth of convective anvils defines their shortwave reflectivity [*Liou, 1986*], and the width of convective anvils determines

the partitioning between radiation emitted from high, cold clouds to that from shallow clouds or low, warm regions of clear sky [Stephens *et al.*, 2008].

Extensive previous theoretical and observational work has investigated the interactions between climate and deep convective morphology. Focusing on different facets of these interactions, previous studies have hypothesized and measured how clouds respond to climatologically warmer sea surface temperatures (SSTs):

(i) The Thermostat Hypothesis was originally proposed by *Ramanathan and Collins* [1991]. As the name suggests, it is a theory that attempts to explain the self-regulation of surface temperature in the tropics. *Ramanathan and Collins* [1991] compared data collected during a warm phase of El Niño to data taken during an unperturbed period. They found that the reflectivity of cirrus anvils was greater during the warmer SST (El Niño) period. This led them to propose a negative climate feedback between cirrus anvils and SSTs in which a warmer environment creates thicker anvil cirrus and is subsequently cooled by the more reflective cirrus. Recent observational work [Lebsock *et al.*, 2010; Lloyd *et al.*, 2012] has supported this hypothesis.

(ii) The Iris Hypothesis of *Lindzen et al.* [2001] suggests that as SST increases, the mean anvil area of convective systems will decrease per convective system. This is proposed to occur through an increase in precipitation efficiency (the ratio of water mass precipitated out of cloud base to water vapor fluxed into the base of the cloud). The proposed result is a net negative climate feedback composed of two competing processes: cooling through increased longwave emission (dominant) and warming through lessened shortwave reflectance. This hypothesis has been widely contested [e.g. *Del Genio and Kovari* 2002, *Lin et al.* 2004], often based on the validity of observational evidence rather than the plausibility of the proposed physical

mechanisms.

(iii) The Fixed Anvil Temperature (FAT) Hypothesis of *Hartmann and Larson* [2002] proposes a constant emission temperature from deep convection regardless of the climate state and SST. FAT has shown to be reproducible in models [*Kuang and Hartmann*, 2007], if not without limitations [*Harrop and Hartmann*, 2012]. However, it has been suggested that cloud top temperature might actually increase with increasing surface temperature in the Proportionally Higher Anvil Temperature (PHAT) conjecture [*Zelinka and Hartmann*, 2010] due to changes in mean static stability. FAT has been assessed observationally [*Li et al.*, 2012]. *Xu et al* [2007] showed FAT to be approximately true for horizontally large clouds. And, similar, though conceptually different attempts than those described here have been made to relate CloudSat object-clusters to SST [*Behrangi et al.*, 2012].

Although all of these hypotheses link cloud-top and anvil properties to SST, they generally do not propose how changes in SST might affect cloud morphology below cloud top. This is not entirely surprising given the relative ease of observing cloud top properties from space and the difficulties in obtaining any information below cirrus shields, and since at first glance, below-top quantities would seem to be less important to understanding climate forcing than to detailing convective processes. Indeed this is not entirely untrue. However, convective processes are important to climate when they feed up scale, either through the general circulation mass balance or through the effects on the moisture field and precipitation [*Randall et al*, 2003; *Stevens*, 2005; *Igel et al.*, 2014].

This work will detail the existence or lack thereof of (i)-(iii) and a new potential feedback in a unique dataset well suited to the analysis. Then these responses of anvils to SST will be

discussed as a single cloud morphological response. The use of SST as a proxy for climate in the current dataset will be discussed.

2. Anvil-Radiation Feedbacks

The simplest cloud anvil-climate response to investigate with the new methodology is the proposed Iris Hypothesis [*Lindzen et al.*, 2001] which stipulates that anvil areal extent should decrease with increasing SST. Critically, CloudSat retrievals provide no means of evaluating cloud area; they only provide along-track length information. However, if the mean of many clouds can be assumed to be morphologically isotropic in the horizontal as discussed above, then cloud anvil width can be thought of as a diameter from which a horizontal anvil area can be computed. The results of *Chapter IV* indicate this may not be a bad assumption as they suggest that even though individual deep convective clouds may not be circular, only the most oblong anvils may be misleadingly measured by CloudSat. This result, combined with the near symmetry of the cloud object composites in Fig. III.1, indicates that isotropicity is not an unreasonable assumption. While not wholly unreasonable, anvils are sometimes observed to orient in the zonal direction with the prevailing wind shear. In these cases, and indeed for all cases of non-circular anvils, the measured anvil width will be less than the true maximum value. The implication of this is discussed in *Chapter IV*.

In Fig. III.2a, anvil width can be seen to decrease with increasing SST for SSTs over which we might hope to limit the influence of mean vertical motion [*Lau et al.*, 1997]. Also, in Fig. III.1, it is evident that anvils get narrower with increasing SST for any given overlap fraction. This result would imply an Iris-type response in nature. Examination of mean total-anvil ice water content broadly confirms this, as it shows total ice *content* decreasing by ~40%

across the range of SSTs. The number of objects in each SST bin are listed in Table 1. It will be noted that in *Lindzen et al.* [2001] the smaller anvils are proposed to result from an increase in precipitation efficiency; that is, increased rainout is thought to remove water mass from the cloud that would otherwise enhance anvils. If reflectivity over 0 dBZ is broadly thought of as indicating precipitation from CloudSat [*Haynes et al.*, 2009] with higher values indicating more intense precipitation, then examination of reflectivity structures within cloud objects (not shown) suggests deeper and more intense rain shafts as SSTs increase. The increased depth of rain could also be inferred from Fig. III.1 although this figure includes no indication of actual reflectivity values. Of course higher rain rates do not necessarily imply greater precipitation efficiency. However, given the trends in reflectivity, it is impossible to rule out an increase in precipitation efficiency as a possible mechanism. In *Lindzen et al* [2001], pedestal area was assumed to remain constant as SSTs warmed while the anvil was proposed to decrease. This is not the response observed here. The new data show that pedestal sizes decrease with increasing SST.

Next, the existence of a Thermostat-type response [*Ramanathan and Collins*, 1991] in these data will be assessed. Fundamentally, the Thermostat Hypothesis proposes that rising SSTs will result in more reflective anvil clouds through an increase in the total anvil water (likely, ice) mass. If all in-cloud-particle optical extinction properties are the same, this increase in mass would be observed correctly by measuring an increase in optical depth. Optical depth values, though, are frequently not successfully retrieved, so proxy data are required. Figure III.2b shows that the mean CloudSat-derived anvil ice path increases with SST above 300K, although it exhibits very little total trend between 298K and 304K. However, as Fig. III.2c demonstrates, anvil *physical depth* (the difference between cloud top height and anvil base height [i.e. the cutoff height]) increases with increasing SST. The results presented here are interpreted

as supporting a Thermostat-like response. Physically thicker anvils, and weakly increasing ice path of anvils above 300K SSTs should be more reflective in that manner proposed by *Ramanathan and Collins* [1991].

Finally, the existence of a FAT-type [*Hartmann and Larson*, 2002] response to surface warming will be assessed. Counter to the FAT Hypothesis, Fig. III.2d indicates that cloud-top environmental temperature decreases with increasing SST. However, the cooling is only slight at approximately 1.6 K/K for SSTs between 299 K and 302.5 K, and hence is best characterized as being approximately constant. Such a trend is thus indicative of a FAT-type response. The cooling does appear to be robust (statistically at least) and has been suggested as a climate response before from studies using different methods [*Igel* 2011, *Singh and O’Gorman*, 2012]. It deserves some consideration. It is evident from Figure III.1 that deep convection tends to get taller at a high enough rate as a function of SST that it produces cooler cloud-top environmental temperatures in the level-by-level warmer atmosphere (at least in the mean). Taller (i.e. cooler) convective cells tend on average to be more vigorous than shorter (i.e. warmer) clouds. Thus, the cooler cloud top temperatures observed here are primarily indicative of more intense convection with increasing SST – a result that perhaps is unsurprising. Whether this cooling of anvil environmental temperature with surface warming is true between climates, not just within a particular climate, obviously, is yet to be determined. It is likely that FAT/PHAT mechanisms are more relevant in the former case than they are here as they rely on equilibrium arguments. And it should be noted that this analysis is limited by the coarse spatial resolution of ECMWF reanalysis data appended to the CloudSat data granules. The recent results of *Chae and Sherwood* [2010] implicate high altitude processes as being important for the *precise* anvil temperature.

To conclude this section, a new cloud-climate response to SST warming, the Fixed Lower-Anvil Temperature (FLAT) Hypothesis, is proposed. The phrase “lower-anvil” refers to the anvil-pedestal cutoff height, H_{cutoff} , as defined in *Chapter II*. As Fig. III.2e shows, mean anvil base height tends to rise with SST warming at a rate of 0.15 km K^{-1} . The reciprocal of this value, which gives the equivalent cloud base-SST lapse rate, is 6.7 K km^{-1} . The similarity between this lapse rate and the moist adiabatic lapse rate of 6.5 K km^{-1} (the typical lapse rate near tropical convection) suggests that this height rise is related to temperature. Specifically, the implication is that anvil bases rise approximately isothermally with surface warming. Figure III.2f illustrates the same implied FLAT response by showing the ECMWF temperature at anvil base height. Despite the small change in the temperature of anvil base, the use of the term “fixed” is still appropriate given that the change in temperature should have a negligible radiative forcing. This reanalysis-derived temperature is environmental and is only approximately relevant for in-cloud temperature. It is also noted that due to processes such as ice particle sedimentation, a given cloud’s lower anvil height can be expected to vary over the course of a cloud’s lifetime [Yuan and Houze 2010]. Implicit in this discussion is the assumption that CloudSat is sampling clouds across a representative set of lifecycle stages at all SSTs. Further work is necessary to evaluate the validity of this assumption and to assess whether the FLAT response can be reproduced in other contexts, such as numerical modeling experiments.

But, why should a FLAT response exist? Anvil-edge structure is dictated by a variety of diabatic processes: among them, radiation, evaporation/sublimation, and turbulent mixing. All three depend on temperature: radiation through the Stefan-Boltzmann law, evaporation/sublimation through the Clausius-Clapeyron relationship, and turbulence through changes in density if shear is low. The latter two mechanisms rely primarily upon pressure and

temperature variations in the vertical. So it would seem reasonable to suggest that temperature dictates many anvil processes at the interface with clear air. For the lower-anvil boundary, it is possible to imagine a first-order balance between warming from upwelling longwave radiation, which, in the moist tropics especially, is a function both of surface temperature and temperature at levels below cloud, and cooling from downwelling longwave radiative flux divergence and evaporation/sublimation. This balance could conceivably occur at some temperature level in the atmosphere. If an anvil base is too warm, it would evaporate and cool until it reaches the desired temperature balance at the cooler level. This level would be approximately independent of surface temperature and would dictate where the lower boundary of the anvil would exist in equilibrium. As a result, mean anvil base temperature would remain approximately constant across meteorological or climate states in the tropics. It could also be that the anvil base is constrained by the mesoscale flow that tends to organize a dry inflow just above the melting level from clear-air regions into deep convection [*Posselt et al*, 2008].

What, then, are the likely radiative feedback implications of such a response in anvil base? Consider the interstitial air between the sea surface and anvil base. Since emitted radiation is such a strong function of temperature, the downwelling longwave radiation emitted by anvil base would remain largely unchanged with increasing SST. Meanwhile, upwelling longwave radiation emitted by the sea surface would increase. This combination of increased heating from below and unchanged heating from above would result in net heating of the interstitial below-anvil air in the vicinity of the cloud. Further work is necessary to assess these effects.

The climate system is not directly influenced by the length scales of tropical deep convection; rather, the vertically integrated climate system is affected by the perturbation to radiative fluxes caused by these convective storms. Figure III.3 shows mean shortwave and

longwave column radiative heating rates for each object as a function of SST. In order to be consistent with the analysis framework, a sum of column heating rates [L'Ecuyer *et al*, 2008] for the entire width of the cloud object is assigned to each object. Consequently, these values represent the integrated influence of the entire cloud object to the energy budget of the atmosphere. Figure III.3a shows that total shortwave heating for each object decreases with increasing SST. This result agrees with the observed narrowing of cloud objects with increasing SST. The data could also be exhibiting a Thermostat-like response with less absorbed shortwave, but this is difficult to gauge with atmospheric quantities. Figure III.3b demonstrates that the total longwave heating rates per cloud object increase with increasing SST. This is due to the FAT-type response of the cloud objects forcing objects to cool each column less and the narrowing of cloud objects, which reduces the number of columns over which the sum is computed. As Figure III.3c shows, the competing trends displayed in Figures III.3a and III.3b largely offset one another. The trend in total (shortwave + longwave) heating rate between 299 K and 302.5 K is weak. The 303 K and 303.5 K bins show a decrease in total heating rate with increasing SST that is consistent with strongly narrowing anvils over that range (Fig 11a). From these data, a simple climate sensitivity can be calculated as the difference in magnitudes between the 299K bin and the 303.5K bin divided by the range of SSTs. This simple sensitivity is $-5.3 \text{ K d}^{-1} \text{ K}^{-1}$ (Kelvin per day of heating per Kelvin of SST rise), and it comes mostly from the shortwave influence. Since the sensitivity is negative, as SSTs increase, individual cloud objects actually radiatively warm the atmosphere less. To calculate a true climate sensitivity, the frequency of objects and their lifetimes both of which could change with SSTs would need to be known. A top-of-atmosphere analysis was not conducted here because that type of analysis can be conducted more thoroughly with other datasets.

Both the longwave and the shortwave heating rate figures show consequences of the Iris – narrowing anvils shrink each cloud object’s ability to interact with radiation – and of deepening anvils. It would be useful to know which of these is the dominant contributor to the total trends in heating rate. Figure III.3d shows the total heating rate of each object normalized by its anvil depth. The resulting trend is a consequence of changes in anvil width only. The sensitivity for clouds of constant 1m-anvil depth is $-1.0(10^{-3}) \text{ K d}^{-1} \text{ K}^{-1}$. Figure III.3e shows the total heating rate of each object normalized by its anvil width. Its sensitivity for clouds of constant 1m-wide anvil is $2.6(10^{-5}) \text{ K d}^{-1} \text{ K}^{-1}$. Therefore, a unit increase in the width of cloud results in a larger decrease in total heating than does a unit increase in the depth result in an increase. So, it is evident from these data that the trend with increasing SST of total heating of clouds is comparatively more sensitive to changes in anvil width than to equivalent changes in anvil depth. Given that anvils widths change over a wider range than anvil depths (Fig 11a versus 11c), cloud object total heating rates are more sensitive to changes in width than to changes in depth as SSTs increase. Figures III.3d and III.3e also serve to confirm the responses seen in the morphology examination. Figure III.3d shows that total heating increases as SSTs increase. This response is likely primarily a result of deepening anvils. As SSTs increase, Fig. III.3e shows that total heating decreases which is likely due to decreasing anvil widths.

In principle the feedbacks discussed above are proposed responses of clouds to mean-climate warming. In the present work, potential responses are ascertained by examining the trends that appear when cloud objects, all residing within the current climate system, are sorted according to local SST. Thus, the results are limited by the extent to which trends within the observable, current climate are indicative of trends with respect to climate change. However, this is a common limitation when trying to use observational data to understand climate. It has been

shown before that using SSTs as a proxy for cloud feedbacks due to climate change can be misleading [e.g. *Hartmann and Michelsen, 1993; Lau et al, 1997; Bony et al, 1997*]. The present study is immune to some, but not all, of the complications arising from the correlation between time averaged SST and large-scale circulation due to the tropics-wide distribution of cloud objects in each SST bin as a result of the use of instantaneous SSTs. Figure III.4 shows the distribution of cloud objects as a function of SST and latitude. Cloud objects exist in all SST bins at all latitudes 30°S-30°N. This ensures sampling in any SST bin from within the climatological Hadley Cell ascent and descent regions. Figure III.4 shows that the difference in mean SST between the equator and 30° is on the order of ~1K. This result is in contrast to the mean difference of monthly mean SST which is on the order of ~10K. This contrast implies latitude (large-scale circulation) and SST are much more independent in this data set than they are when clear sky is included.

With the above responses in mind and in a final effort to ensure robustness of the data, the data have also been subsampled and reanalyzed to ensure that the trends presented hold regardless of large-scale flow regime and with a consistent number of cloud objects in each SST-latitude bin. Latitude is used as a modest proxy for large-scale flow. Data are resampled whereby equal numbers of data are randomly selected from within 10° latitude x 0.5K bins. The trends are then reassessed with the new, limited data. Figure III.5 shows one such sample of the data. It implies that the trend of increasing anvil depth with SST exists regardless of the latitude bin used. None of the trends shown in Fig. III.2 is ruled out by multiple random iterations of Fig. III.5.

3. Conclusions

The derived cloud object data were used to analyze the dependence of anvil morphology on SST. Based on the analysis presented, we hypothesize that the various climate hypotheses discussed function in the following synergistic manner. If FAT (Fig. III.2d) and FLAT (Figs. III.2e&f) can be assumed logically to be the most likely mechanisms occurring in the real atmosphere, then anvil clouds are left with strong upper and lower boundary conditions. Again, this is true insofar as both of these mechanisms are likely to be only first order accurate. These hypotheses rely on temperature and seem to occur due to potentially strong physical constraints. The FAT in particular has shown robustness to past analysis despite the uncertainty here. The profile of temperature is relatively well constrained in the tropics [Meehl *et al*, 2007; Igel *et al.*, 2014]. It is generally thought that, in the current climate and under conditions of climate change, the tropical temperature profile is dictated by the moist adiabat which is a function of surface conditions. In a world with a warmer surface, the moist adiabat is steeper due to the non-linearity of the Clausius-Clapeyron relationship. This means that the temperature levels of the anvil base and anvil top, as dictated by the FLAT and FAT mechanisms, respectively, are farther apart in a warmer atmosphere. Consequently, anvils should become deeper if their base and top temperatures are constant. This response is essentially a Thermostat. It is also conceivable that if anvils become sufficiently deep in response to surface warming, and assuming only moderate changes in total detraining mass or volume, an Iris-type response might also occur, especially since anvils are much wider than they are tall. The assumption of constant detrainment is certainly questionable, but the mean cross-sectional area of anvils in the cloud object data do not exhibit a statistically significant trend from the 299.5K to the 302.5K bins and varies by only

30% across the entire range while the anvil width varies by 45% and continuously across the SST range. Total anvil ice path varies even less: 10% and 38%, respectively.

Figure III.6 summarizes the findings of this work by illustrating the primary cloudy-sky anvil-radiation effects: consistent longwave radiation (FAT+FLAT), resulting in a constant anvil greenhouse effect; and modulated solar radiation (Thermostat+Iris), resulting in more reflection and less transmission but over less anvil area. The important implication of the figure is that all the cloud-climate feedbacks happen simultaneously. The anvil structure changes in a coherent and theoretically understandable way. Neglected in this work are clear sky effects, a full analysis of which would require understanding changes in cloud object frequency in addition to the changes of objects with SST described here.

It is noted explicitly that these methods are only relevant to the mean of an ensemble of many cloud objects. Any cloud-climate response discussed herein should not be assumed to be at work for any individual cloud. The methodology relies on the assumption of strong statistical significance achieved through binning and averaging. Furthermore, the physical mechanisms behind the cloud responses to warming are thought of only in an equilibrium sense and often do not imply anything specific about an individual object. The climate, though, inherently depends on the ensemble mean of these responses. Ultimately then, cloud object methods are ideal tools with which to study the cloud-climate problem and their use in the future is encouraged. Future chapters will examine sensitivity tests to environmental characteristics (including SST) and cloud resolving modeling simulation and will confirm this conclusion.

4. Tables

Table III.1: The number of cloud objects in each SST bin in Fig. III.2.

SST (K)	Number of objects	SST (K)	Number of objects
299	323	299.5	499
300	835	300.5	1515
301	2689	301.5	3968
302	4896	302.5	4739
303	3282	303.5	1437

5. Figures

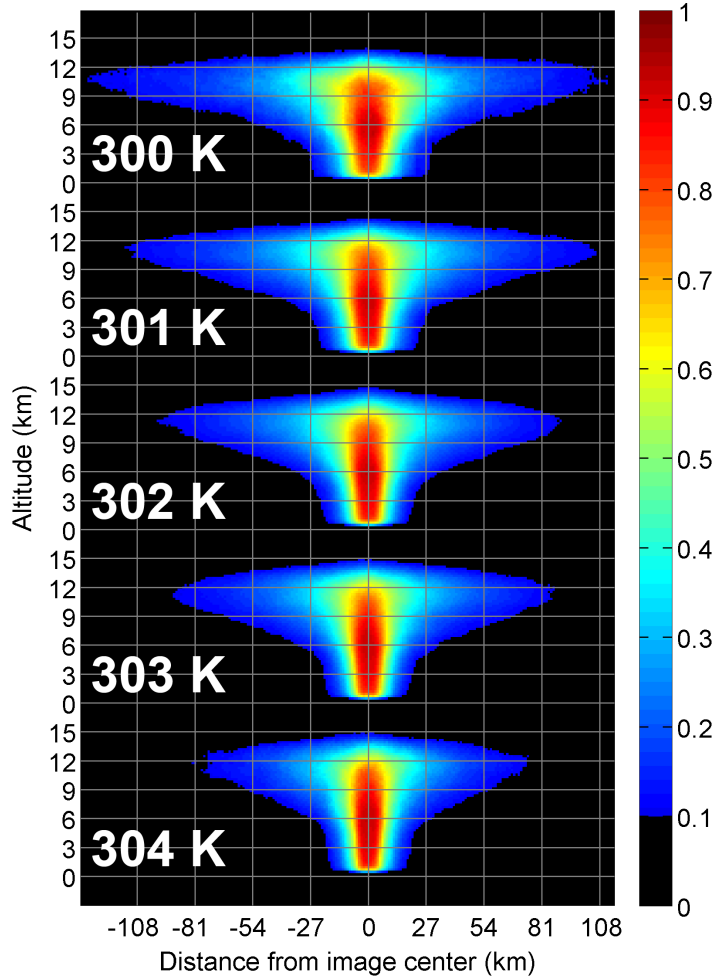


Figure III.1: Fraction of cloud objects at each listed SST that overlap at a certain grid point relative to the pedestal center. The magnitude, therefore, indicates the fraction of clouds with cloudiness relative to their center. This figure is only to be used as a visualization aid. It shows that anvils narrow and rise with increasing SSTs.

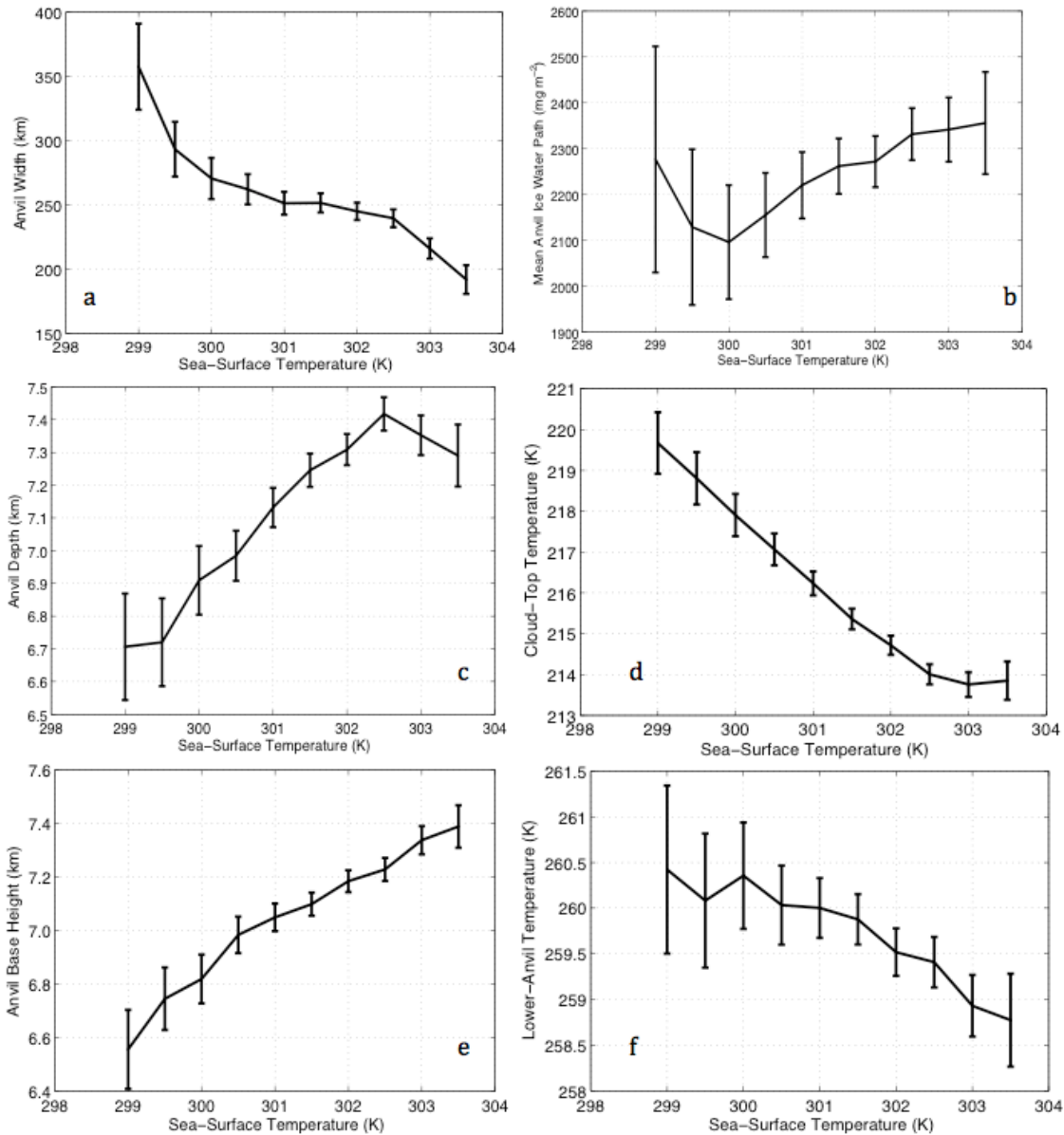


Figure III.2: a) Binned mean anvil widths (as a function of SST with confidence intervals in vertical bars); (b) Anvil ice water path; (c) Physical mean anvil depth; (d) ECMWF analysis temperature at the level of cloud top; (e) Anvil base height; (f) ECMWF analysis temperature at the level of anvil base. Error bars indicate 95% confidence intervals for the mean in each SST bin.

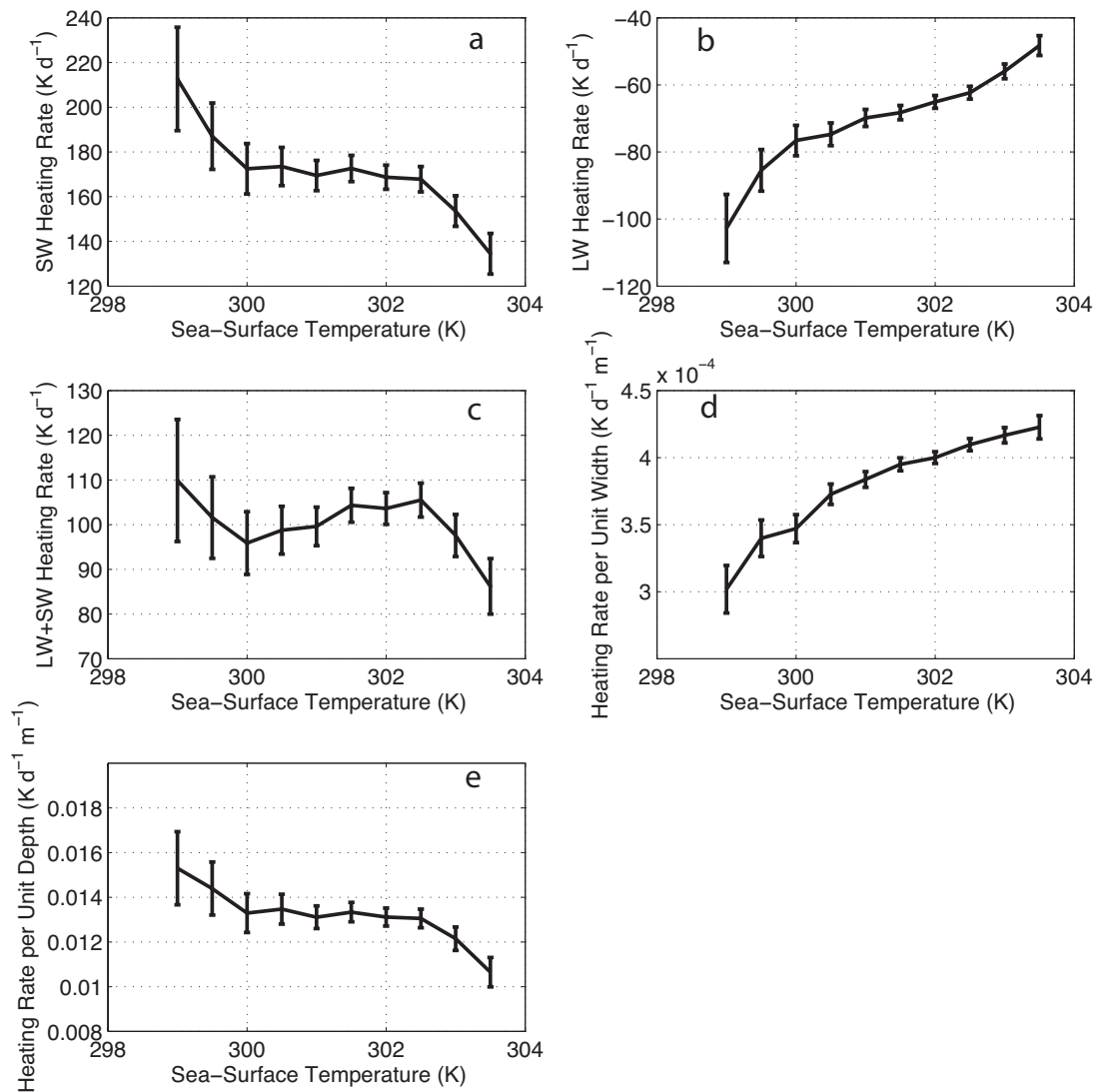


Figure III.3: All panels show total cloud object column radiative heating rates as a function of SST. a) shortwave total heating rate. b) longwave total heating rate. c) longwave plus shortwave total heating rate. d) longwave plus shortwave total heating rate normalized by anvil width. e) longwave plus shortwave total heating normalized by anvil depth.

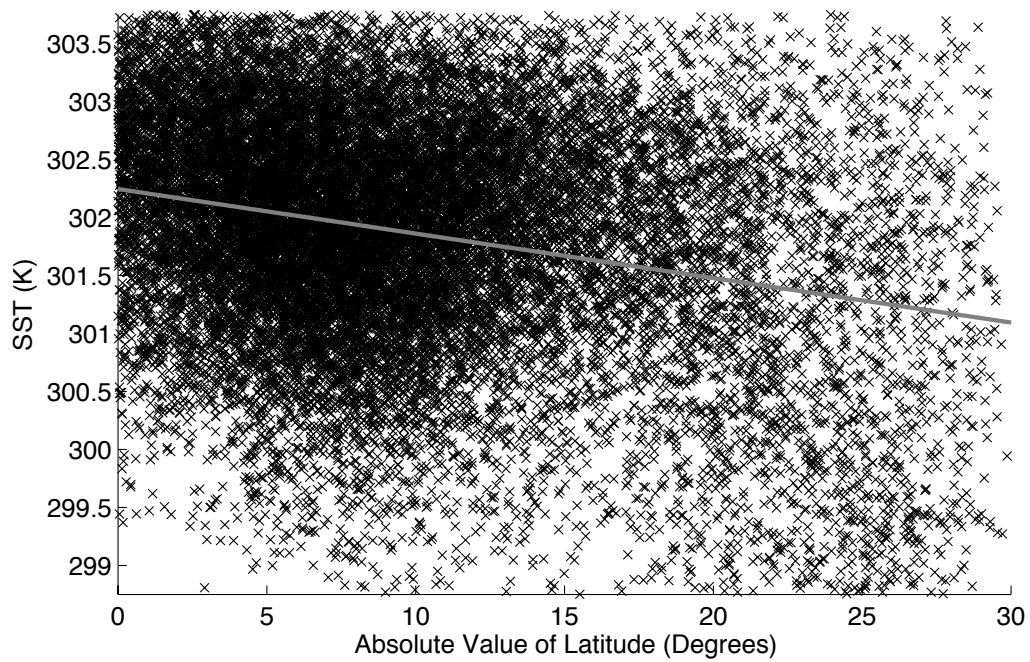


Figure III.4: Scatter of cloud objects occurrences by the magnitude of latitude and SST. The gray line shows the simple least squares fit to the cloud of data as a function of latitude.

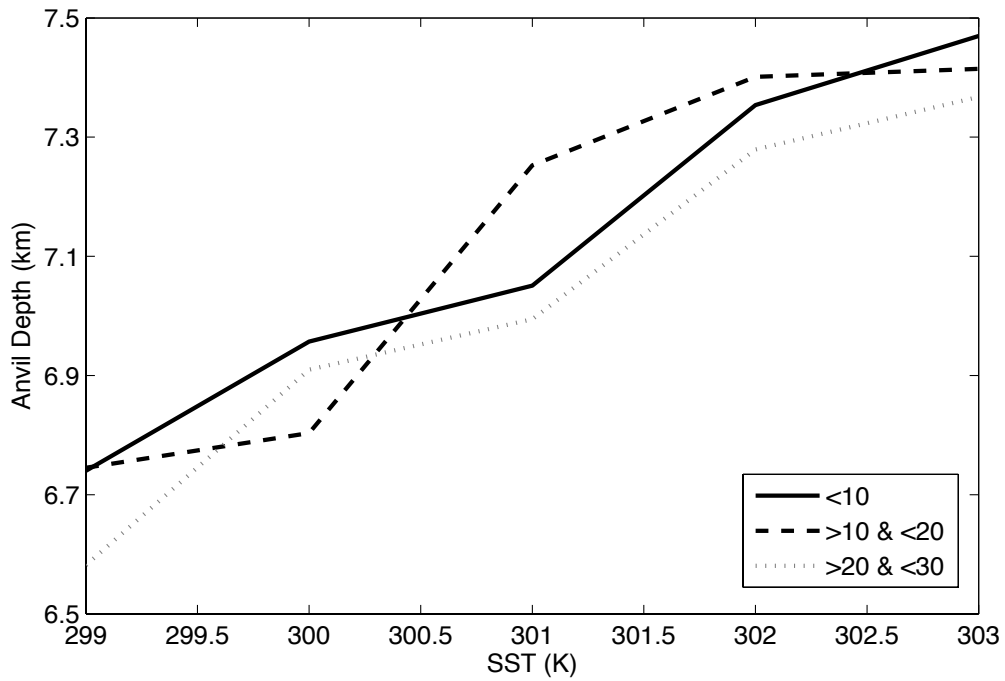


Figure III.5: An example of the randomly resampled data wherein each 10° latitude bin and each 0.5K SST bin is artificially limited to have the same number of samples. This figure shows the trend in anvil depth as a function of SST (as in Fig. III.2c) for the three latitude bins.

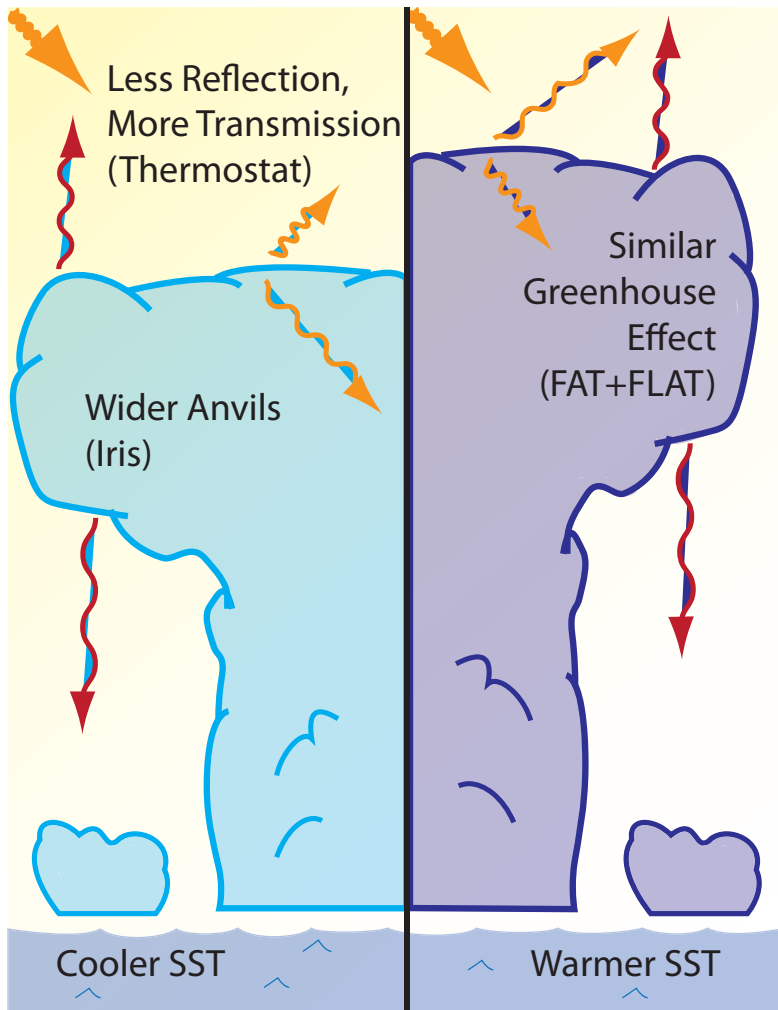


Figure III.6: Schematic illustration of the various dependencies of cloud object properties on SST. A representative low-SST cloud object is shown in blue and a high-SST object is shown in purple. Longwave emissions are shown in red arrows and shortwave effects are shown in orange. The parenthetical statements list the corresponding climate hypothesis.

CHAPTER IV: DEEP CONVECTIVE CLOUD MORPHOLOGY AS OBSERVED BY CLOUDSAT

1. Introduction and Background

Many of the still-unused components of the cloud object dataset developed in Chapter II are utilized here in Chapter IV. The focus now shifts to how components of deep convective clouds influence one another. Much of the discussion below pertains to the smallest scales influencing convective morphology.

Studies of atmospheric phenomenon tend to focus on infrequent, extreme events: droughts, floods, and hurricanes. While these events are those that have the greatest impacts on lives and livelihoods and are certainly worth studying, they do not represent the bulk of everyday weather which tends to be characterized by more unremarkable meteorology. This tends to be particularly evident in the tropics where the focus is often on clusters and superclusters, mesoscale convective systems, tropical storms, and Madden-Julian Oscillations rather than on ordinary, isolated deep convection. Much of the basic study of deep convective cloud scales has focused on tropical squall lines and clusters [see *Houze and Betts* 1981; *Chen et al* 1996; *Mohr and Zipser* 1996; *Liu and Zipser* 2013]. However, tropical meteorology is primarily composed of unremarkable oceanic, ordinary, deep convection – which is only unremarkable *because* of its high frequency. *Riehl and Malkus* [1958] famously recognized this long ago, but it has not been until recently with the launching various high-resolution satellites that the study of a large number of deep convective clouds over a long time has become possible.

In *Chapter II*, it was suggested that examining the length scales of convective elements was both a novel and instructive endeavor. Therein, the discussion pertained to how these length scales of convection related to the climate impacts of deep, tropical, oceanic convection. The objective in this chapter will be to detail convective cloud scales in an effort to elucidate internal aspects of the nature of convection itself. At the behest of *Mapes [1997]*, it will be stated explicitly that “scales” is used throughout this paper to mean “physical dimension.” “Scales” should not be confused with the distance at which the impact of convection is felt by the atmosphere. Lest enumerating length scales seem a trivial endeavor, consider a recently conducted informal, nonscientific survey of scientists in Colorado State University’s Department of Atmospheric Science that asked questionees to list the mean scales of mature, tropical, oceanic convection. The results are shown in Fig. IV.1. The answers varied widely, and as will be shown show below, are fundamentally incorrect and biased when compared to the particular definitions employed below.

Many investigations of convective scales occurred during the early days of the study of tropical convection. Between the landmark field campaigns of the Global Atmospheric Research Program (GARP) Atlantic Tropical Experiment (GATE) [*National Academy of Sciences 1971*] and Tropical Ocean Global Atmosphere Coupled Ocean-Atmosphere Response Experiment (TOGA-COARE) [*Webster and Lukas 1992*] as well as later in KWAJEX [*Yuter et al 2005*] and earlier in general [*Malkus and Riehl 1964; Holle 1968; Lopez 1976*], much was determined about the size and shape of tropical convection [*Houze and Cheng 1977; Houze 1982; Rickenbach and Rutledge 1997; Cetrone and Houze 1998; Johnson et al 1999*]. This was achieved primarily through photogrammetric and radar analysis. What these local area studies and larger campaigns lacked fundamentally, though, was broad spatial and temporal coverage. As stated earlier, even

when combined, GATE and TOGA-COARE covered less than 1% of the global tropics. These works also tended to focus on the entire population of cumulus convection from shallow to deep cloud systems. Analyzing data with this focus rightfully points out the importance of shallow convection to the entire population but fails to adequately detail the characteristics of deep convection given its relative rarity [Wood and Field, 2011]. Other of these studies tended to focus on the scales of various tropical mesoscale convective systems (MCS). While such systems can greatly impact communities, they only make up a small portion of the cloud population. The research presented here will focus on cataloguing the length scales of tropical, deep convection that occurs up scale of frequent, trade wind convection and down scale of synoptic clusters of convection. That being said, MCSs are not excluded from the dataset. As described in *Chapter II*, the clouds composing the dataset occur over all tropical oceans during the first 5 years of the CloudSat mission, 2006-2011. As throughout this dissertation, a cloud object approach will be used. This kind of technique has been utilized recently in a number of ways [e.g. Bacmeister and Stephens 2011; Riley et al 2011; Dias et al 2012]. The goal behind employing such a technique is to isolate individual clouds from the larger-scale environmental meteorology. It also allows for thorough statistical analysis by combining information from many individual clouds. The strength of the statistics will allow for a variety of quantities that will be treated as both independent and dependent variables through this chapter.

Previous studies have applied a scientific methodology to what is in some ways an intuitive field: the physical size of deep convective clouds. Size is something even the layman could describe from everyday observations, but given the results of an informal poll conducted within the Department of Atmospheric Science at Colorado State University (see Fig. IV.1 for description and results), it would seem that many different impressions of clouds exist. The first

measurements from GATE were of radar reflectivity area, echo top heights, and echo-region longevity [Houze and Cheng 1977]. TOGA-COARE results showed the ubiquity of isolated convection as it was present 48% of the time through the 80-day campaign [Rickenbach and Rutledge, 1998]. However, even after these two campaigns, a thorough detailing of many potential length scale characteristics of these ubiquitous clouds is still lacking in the literature. While the discussions that do exist have made significant contributions they tend to be limited by temporal, spatial, instrument constraints, or study scope [Machado et al, 1993; Mapes and Houze, 1993; Masunaga et al, 2006]. This may be partially a function of radar domain sizes. The results in *Chapter II* would seem to suggest why. Therein, it was found that many tropical convective cloud objects are too large to fit in a single ship-borne radar's domain. This idea would certainly be consistent with both the truncation of areal coverage data in *Houze and Chen* [1977] and with the author's experience operating a radar on board the R/V *Revelle* during the recent Dynamics of the Madden-Julian Oscillation (DYNAMO) campaign [Zhang et al, 2013] in the Indian Ocean. Given these limitations of surface based radar, one of the goals of this chapter is to enumerate length scales of tropical convection with the developed cloud object database. By thoroughly examining these length scales, simple theories for various characteristics of tropical convection will be derived.

In addition to listing the physical scales of tropical, deep convection, the discussion in this chapter will demonstrate the ways in which convective cores and anvils are related. Results will show their mutual growth and interactions. *Li and Schumacher* [2011] suggested that large-scale areal coverage of anvils and of convecting regions are related, with more convective coverage yielding larger anvil coverage. Figure 18c from their manuscript, together with a linear regression through the local maxima of their data, suggest a nearly one-to-one relationship of

regional anvil coverage over tropical oceans to regional convective coverage. *Feng et al* [2012] also note somewhat similar behavior. The applicability of these ideas to individual clouds will be tested here. It will be shown that the relationship between anvils and cores among single-core and multi-core convective storms behave in similar and dissimilar ways and that the differences arise transitionally rather than abruptly as the number of cores increases. It is hoped that by analyzing scales of convection that simple, theoretical conclusions may be drawn regarding the nature of tropical deep convection. Establishing these theoretical ideas is the primary goal of this chapter.

2. Methods

The cloud object definition and partitioning method developed in *Chapter II* will be used here in *Chapter IV*.

When relevant, the results presented in Section 3 will be limited to small, isolated convective events by screening the database for cloud objects with few cores or small pedestal sizes. However, other results will necessarily include cloud objects from this scale all the way up to large multi-cellular cloud clusters or MCSs since no upper limit on length scales is applied. The goal of the analysis though will be to focus on the most highly populated, smaller scale clouds of the dataset. It was implied in *Chapter II* that this was possible and because these make up the vast majority of potential cloud objects. These objects have often only one or two cores within their pedestals. They have well-developed anvils as a requirement of the object definition procedure, but are unlikely to have organized mesoscale structures. However, as is ultimately demonstrated here, focusing on just the smallest, most frequent deep convective clouds is not necessary. Clouds appear to transition smoothly from small to large objects.

2.1 The Radiative-Convective Equilibrium Simulation

Later in this paper, the results from a large-domain cloud resolving model simulation will be compared to those obtained from CloudSat. This is the same simulation briefly discussed in *Chapter III*. The simulation is conducted with the Regional Atmospheric Modeling System (RAMS) [*Pielke et al. 1992; Cotton et al. 2003; Saleeby and van den Heever 2013*] model. The model is integrated forward for a sufficient time such that it achieves a statistical equilibrium (all atmospheric energy and moisture tendencies are negligible) often referred to as a state of radiative-convective equilibrium (RCE) [*Manabe and Strickler 1964*]. The model is run with a fixed ocean surface temperature of 300 K and utilizes bulk surface flux parameterizations. A horizontal grid spacing of 1 km is used and 65 vertical levels are employed, which is more than sufficient to meet the moisture resolution requirement of *Tompkins and Emanuel [2000]*. The model is run with a very large number of points in a “canyon” type configuration [*Tompkins 2001*] with 3000 “zonal” and 200 “meridional” points. While only 200 km in one direction is rather small to resolve all possible cloud scales, the 3000 km direction allows for more complex, large-scale structures. Periodic lateral boundary conditions are used.

3. Results and Discussion

3.1 The Average Cloud

The goal inspiring this work was to enumerate the average, deep, oceanic convective cloud. This is a simple task given the use of cloud objects. Figure IV.2 shows a composite of all single core cloud objects. *Chapter II* contains an explanation of how this figure is constructed. Briefly though, Fig. IV.2 illustrates the percent of cloud objects that would overlap if all cloud objects were centered at the same place in time and space. This overlap percentile composite represents the average cloud object from the data set at each percentile threshold. However, the

figure is mostly for the purpose of visualizing the data and trends therein, and it should not be taken as precisely numerically indicative. The most surprising aspect of this composite is both the width and depth of the anvil. Table IV.1 includes the statistics of the average cloud as computed using the entire dataset. The pedestal width is ~11 km which is broadly in keeping with mostly graphical (i.e. not specifically enumerated) results from past studies [e.g. *Zipser* 1977; *Leary and Houze* 1979; *Rickenbach and Rutledge* 1998] although this value dwarfs the measured updraft widths of *LeMone and Zipser* [1980] as might be expected. Exhibiting high population density power, 11 km is not only the mean, but also approximately the median pedestal width. Anvil width is 95 km, which is much larger than many ground-based radar studies would be able to measure consistently, given that for a 250 km radius radar domain, a pedestal would need to be centered within 205 km of the radar to contain the entire anvil or within the inner 67% of the domain. In fact, 95 km very nearly fits the minimum threshold of 100 km to be referred to as a “cloud cluster” in the GATE nomenclature [*Houze* 1982], despite this being the average for single core clouds. Interestingly, anvils of ~100km horizontal scale would be difficult to observe visually as the anvil would stretch beyond the horizon. Also, many ground-based radars may not be especially sensitive to the types of particles making up the anvil. These facts suggest why anvils are often assumed to be smaller in the cloud poll than they actually are. Again, one of the surprising results is the near similarity of anvil and pedestal depths. Certainly the cloud poll (Fig. IV.1) takers did not think this would be the case, and there is seemingly no universal conclusion drawn on this subject from the literature [*Zipser* 1977 and citations therein]. The measured anvil depth (6.4 km) falls within the range of these early observations cited in *Zipser* [1977] of anywhere between 1 and 10 km. It’s worth noting that the measured anvil cutoff is primarily a measure of the height at which the object transitions in the

vertical from pedestal-like, nearly constant width with height, to anvil-like, wide and overhanging clear air or pedestal, characteristics. The cutoff height may not reflect the anvil base height away from the pedestal especially if ice mass falls out from anvil base away from the pedestal. The standard deviations of sizes in table IV.1 are often quite large. These are due to a small population of very large objects.

An “average cloud” may also be examined for those cloud objects with 2 cores. As it will be demonstrated, the 2-core results (statistics in Table IV.1) provide better insight when compared to the single-core results, than when examined alone. The pedestal width is almost exactly twice that of the single-core. The anvil width of two-core systems is larger than that of a single-core system, but not greatly so. As shown in Table IV.1, cloud top height, anvil cutoff height plus anvil depth, increases as cloud objects could presumably grow more easily in the vertical with two cores than with one due to multiple cores converging cloud mass into the same volume of air. Anvil depth also increases both because anvil tops get higher and bases, lower for the same reason (more mass). The three-or-more core results broadly follow the same trends. Interestingly, the pedestal width of each object divided by its number of cores, a crude measure of the width of convective cores (as measured by the methodology), is ~12 km per core and remains nearly constant as the number of cores increases.

The composite image of cloud objects with 2 or more cores (Fig. IV2) is much wider and appears to exhibit basic characteristics consistent with MCSs [Houze, 2004] especially at low percentages originating from the largest objects. It has a wide pedestal and deep anvil across a wide range of percentiles unlike the single cell composite. The highest overlap percent is centered in the mid-troposphere, whereas in the single core composite it is centered in the lower troposphere. This result shows the slight dissimilarity of mid-level structures between multi-

celled clouds and single cells and may imply differences in the updraft structure as in *Luo et al.* [2008] who discuss three stages of cloud growth. The statistics support a colder cloud top and wider anvil. The causes and implications of some of these results will be revisited later.

Interestingly, pedestal top or anvil base (cutoff) height stays almost constant from one to two to potentially many core systems, although there is a statistically significantly different population of lower cutoff heights in the three-or-more core clouds than either the single or double core clouds. However, it is primarily the anvil depth that changes in such a way that increases the total cloud object height. These trends hint at different roles for cloud objects with different core numbers. Single-core clouds have an anvil area that is already ~30% as wide as the 3-or-more-core cloud objects. Naively assuming constant mass flux per core, the small increase in anvil width with increasing core number would imply much more detrainment into the environment per amount of convective mass flux for single core cloud objects than for multi-core cloud objects. Perhaps this helps to explain why single-cell clouds tend to precede multi-cell clouds. Single-cell clouds might moisten the environment because they flux proportionally too much mass out of their anvils {i.e. perhaps they have low precipitation efficiency (the ratio of moisture precipitated to that fluxed through the cloud base [*Cotton et al.*, 1995])}; then, multi-cell clouds could form in the newly moistened environment; then, they may rain out the excess vapor (i.e. perhaps they have high precipitation efficiency). The dynamics of this evolution are unclear from this study, but the concept works from a system perspective. These ideas have been suggested previously and are conceptually coherent with studies showing the importance of MCSs to total rain production [e.g. *Mohr et al.* 1999; *Rossow et al.* 2013; *Barnes and Houze* 2013].

3.2 Pedestal Widths

In this section, details of trends in convective quantities with increasing pedestal widths will be discussed. In order to help to build the conceptual model of clouds that will be the result of this study, pedestal width necessarily will be treated here as an independent variable from all other meteorological and morphological quantities with the assumption that the local convection itself dictates its own pedestal width. This assumption will not be made in later sections of this paper and also was not made in previous chapters.

The basic trends in morphology with increasing pedestal width are shown in Table IV.2. Unsurprisingly, the number of counted cores increases with pedestal width. In fact, many of the trends are conceptually consistent with increasing cores (as in the previous section). That the anvil cutoff height characteristics are so similar between clouds with pedestal widths less than 25 km and clouds with pedestal widths between 25 km and 50 km is noteworthy despite the other differences between these groups of clouds.

Anvil width tends to increase with pedestal width. Detailing the characteristic way in which anvil width functionally depends on pedestal width was one of the motivating goals of this study. It was expected that some relationship would exist between pedestal and anvil width such that as pedestals got wider so too would anvils. Two types of linear scaling are possible. The first is one in which anvil widths grow faster than pedestal width. The anvil-to-pedestal width scaling would be 2:1 or more. The second is in which anvil widths grow more slowly than pedestal widths. The scaling exhibited by such clouds would be 2:1 or less. To our knowledge, such a scaling relationship has not been proposed in the literature. Figure IV.3 shows composite clouds for different pedestal width bins. As pedestal width increases, so too does anvil width. However, from visual inspection, it would appear that pedestals tend to increase in width more

than anvils. For example, the 10th percentile cloud at narrow pedestal width (<25km) is ~20% as wide as the corresponding anvil while that of the wide pedestal width (>25km) is ~50%. This result fits well with the latter results presented in § 3.1.

Individual cloud object pairs of pedestal and anvil widths are plotted in Fig. IV4a. Due to the inclusion of a minimum detrainment index [*Bacmeister and Stephens 2011; Chapter II*], cloud objects are required to have an anvil width to pedestal width ratio of 1.5. There is considerable spread given the large number of cloud objects. However, there is a group of points located just above the 1:1.5 line in Fig. IV4a that seems to both cluster and trend. A simple linear regression fit to these data implies a scaling of 1:1.9 as shown in the dashed gray line. Any linear fit with a slope of less than 2 implies that the ratio of anvil width to pedestal width is decreasing. Table 2 implies the same result -- the ratio of anvil width to pedestal width for cloud objects with pedestal widths of less than 25 km is 7.4 while for the ratio of those larger than 50 km is only 2.7. Figure IV.4b illustrates that the scatter of ratios of anvil width to pedestal width decreases as pedestal width increases.

The linear fit in Fig IV.4a leaves something to be desired. For example, it is not highly accurate at either high or low pedestal widths nor does it provide much physical insight into convective processes. Figure IV.5 shows a slightly different kind of regression fit for the data. The data are binned logarithmically by pedestal width. The bins are logarithmically spaced to account for the relative paucity of data at high pedestal widths. The mean of anvil widths within each bin is calculated. Then, powers of pedestal width are taken in an attempt to linearize the data in order to better fit a simple linear regression. Pedestal width to the 2/3rd power was determined to yield the best correlation coefficient for the available data. This implies that

statistically, the population of anvil widths grows at a retarded rate relative to pedestal width. This result is consistent with the results in the previous section.

But why would a $2/3^{\text{rd}}$ power be the most appropriate relationship for these data? If a deep convective cloud can be thought of as a pedestal that fluxes mass into an anvil, then a simple geometric construct can be imagined that helps to explain this $2/3$ parameter value. Assuming morphological isotropicity in the mean, then a convective pedestal is approximately cylindrical with its axis oriented vertically. Neglecting any lateral organized detrainment or stochastic entrainment through the sides of the cylinder, the cloud fluxes mass up through the depth and out through the top of the cylinder. Thus, the total flux through the pedestal is

$$F_p = \rho \pi R_p^2 w \quad (1)$$

where F_p is the mass fluxing out of the pedestal top, ρ is the air density, R_p is the pedestal radius, and w is the flux velocity. Anvils might be thought of as a spherical balloon being filled by the mass fluxing out of the top of the core within the pedestal. When integrated from the initial time of anvil genesis to some final time, its mass flux is

$$F_A = \rho \frac{4}{3} \pi R_A^3 / \Delta t \quad (2)$$

where F_A is the anvil flux (total mass per total time) and R_A is the anvil radius. Upon equating the fluxes and performing some algebra, the expectant relationship between anvils and pedestals is

$$R_A = \sqrt[3]{\frac{3}{4} w \Delta t R_p^2} = \sqrt[3]{\frac{3}{4} w \Delta t R_p^{2/3}} = \alpha R_p^{2/3} \quad (3)$$

where α is just the third root of the proportionality constants. The densities are assumed to cancel in (3) for simplicity, but if they don't, R_A 's functional dependence on R_p is unchanged. The neglect of entrainment has a direct consequence if w in (1) in fact depends on R_p .

Perhaps, however, an anvil does not really behave like a sphere. Certainly, in the mean (see Table 1), anvils are much wider than they are deep. In such a case, an anvil may be assumed to be ellipsoidal with major axes in the horizontal plane and a corresponding flux relationship as

$$F_A = \rho \frac{4}{3} \pi R_1 R_2 D / \Delta t \quad (4)$$

with R_1 , R_2 , and D representing the different major axes, radius 1, radius 2, and depth, respectively, of the ellipsoid. As long as each length continues to grow as any other one of them does, such that, for example, R_2 and D are both a function of R_1 , then $R_1 * R_2 (R_1) * D(R_1)$ results in a third power of R_1 and the functional $2/3^{\text{rd}}$ power may reasonably hold. Assuming isotropicity, R_2 is identically equal to R_1 . In the data, it turns out that D is only a very weak function of R_1 where R_1 is taken to be one half the measured anvil width and D is the anvil depth (not shown but implied by Table 2). Of course, these derivations are far from physically precise predictors of anvil growth for any one cloud. The goal is only to derive the basic functional form suggested by the $2/3^{\text{rd}}$ scaling for the population of clouds.

The question then becomes to what extent this $2/3^{\text{rd}}$ scaling is predictive in the mean. If it has any power to predict anvil width based on pedestal width, then a physically based anvil width parameterization scheme might be created. Of course, such a scheme could only maximally be as accurate as the prediction of pedestal width. The prediction intervals calculated from the binned data are very large relative to the overall trend (not shown but implied by the large spread of data points in Fig. IV.4a). So, anvil width and pedestal width data were both independently rank ordered and then plotted against one another. No individual “data point” is necessarily representative of any actual cloud object in our dataset. Every point is potentially artificial. That being said, if the same $2/3^{\text{rd}}$ scaling still holds, then a 1-to-1, monotonic predictor

of anvil width will be pedestal width to the $2/3^{\text{rd}}$ power. While this relationship will create clouds with overly consistent anvils for each pedestal width, when considering any individual cloud, it should recreate the appropriate statistics of the true $2/3^{\text{rd}}$ scaling in the mean, if pedestal widths are predicted in the proper proportions. Figure IV.6 shows the results of the artificial, rank ordered data. Again, the degree of fit is remarkable. Interestingly, the regression fit to this line is steeper than the fit of the mean (Fig. IV.6). This is due to the, in some senses, limitless upper bound to anvil width in the binned data in Fig. IV.6.

This $2/3^{\text{rd}}$ scaling relationship seems to work across a wide range of horizontal scales – from single to many cored systems. One might ask why this scaling relationship would have any relevance across such different physical regimes especially given the thought experiment of a cylinder and sphere. Figure IV.7 shows the scaling relationship for just single and double core cloud objects and for clouds objects with 4 or 5 cores. The $2/3^{\text{rd}}$ relationship is still a good fit for both of these datasets. It would seem that the only conclusion to be drawn from this result is that the physics governing the interrelationship between pedestals and anvils is somehow universal in tropical deep convection. The most significant difference between the two lines in Fig. IV.7 is the range over which the bins occur. In the region of pedestal width overlap, 11 km – 70 km or $(500 \text{ m})^{3/2}$ – $(1700 \text{ m})^{3/2}$, the slopes of the data are very similar. The single and double core data exhibits some interesting flat behavior below 11 km or $(500 \text{ m})^{3/2}$. This result is likely the consequence of small, young anvils growing in inconsistent ways among different cloud objects (as in discussion of composite clouds in *Chapter II*).

These results may provide a possible explanation for the poor correlation between convective core (pedestal) coverage and anvil coverage presented in *Li and Schumacher [2011]* and *Feng et al [2012]*. These studies failed to account for the power-law non-linearity observed

here although what is being measured in these previous papers is slightly different from what is being detailed here, even if the aims are similar. While these other studies tended to focus on slightly larger objects than are the focus of this chapter, our results are inclusive of their scales.

Finally, it is mentioned that section 5 contain a variety of geometric arguments concerning sampling of clouds. These are especially relevant to the $2/3$ scaling. In brief, it is determined that off center sampling of cloud objects is unlikely to influence the form of the scaling but could influence the precise regression coefficients. It is also found that even if cloudy regions are not horizontally circular, the numbers quoted herein are unlikely to be far from the true characteristic horizontal length scales of convection.

3.3 Base Height

It is assumed sometimes in convective parameterization schemes that convective core width scales with the boundary layer depth [e.g. *Arakawa and Schubert* 1974]. If, in the tropics, it can be assumed that cloud base height rests on the boundary layer [*Oruga and Cho* 1974], admittedly a potentially questionable assumption, then it is possible to test this parameterization. The term “base” is used here to mean the bottom of the pedestal. Table 3 shows trends in cloud object characteristics with increasing base height and if the assumption above is valid, increasing boundary layer depth. As cloud base height increases, pedestal width actually decreases.

Masunaga [2013] saw a similar trend and attributes it to subcloud layer cooling. In contrast to *Holle* [1968], cloud top height also decreases with increasing base height. These two trends would seem to imply weaker convection with increasing boundary layer depth. It could be that these results are also a reflection of differences in cloud age with clouds exhibiting high base heights being younger, less vertically developed, less rainy clouds. This argument is only logically consistent for the ensemble lifetime of clouds; it is not strictly correct of any individual

cloud whose lifecycle will be more nuanced than that of the mean cloud. Unfortunately, the range of cloud base heights in the data is necessarily low due to various requirements of the selection algorithm [*Chapter II*] and its component data. Also, the >1000 m bin only contains ~0.1% of the cloud objects. But decrease in pedestal width with increasing base height trend is noted, even if it is far from conclusively proven, especially given the amount of attenuation that is likely by cloud base and the potential radiometric influence of the surface.

3.4 Anvil Top Height

Tropical, deep convective clouds of all types contribute to both local and global scale circulations. *Riehl and Malkus* [1958] estimated the contribution of undiluted hot towers to the Hadley circulation. *Gray* [1973] and *Houze* [1982] considered the effects of convection on regional circulations at the convective and meso scales. There is currently no way to examine explicitly such responses to convection from any current satellite since no earth observation platform provides any direct measure of velocities above the surface level either in cloud or clear air. An attempt will be made to infer such contributions per cloud object by using the clouds as a simple diagnostic.

In convective circulations, air is forced upward through convective cores and then outward through anvils. Deep convection actually “pushes” upper tropospheric air (see next section) through local perturbations to the mass field. At first glance, it might be assumed that wider anvils are more likely to contribute to farther afield circulations than narrower anvils are. That is to say, that it could be assumed that wide anvils are the result of a cloud’s ability to influence the motion of air over a large area and therefore could be an indication of the cloud contributing to large-scale, horizontal circulations in addition to local, vertical circulations. Wide aspect ratio clouds could be indicative of wide aspect ratio circulations. If this assumption,

that in the ensemble mean, wider clouds are better able to influence upper level horizontal flow than narrower clouds, can be made, then other cloud morphological quantities can be regressed against anvil width to determine their controls on large-scale circulations. Figure IV.8 shows the scatter of anvil widths as a function of anvil top height with the best-fit linear regression line. From this figure, it would seem that higher topped anvils can also be horizontally wider. A similar result could be deduced from *Cetrone and Houze* [2006] who implicated subtle humidity increases as resulting in larger overall clouds. *Yuan and Houze* [2013] also made analogous conclusions (wider and higher clouds) but assumed the anvil width implies some portion of the height. This fails to explain explicitly the relationship between cloud top height and anvil width. Thus, to a first order guess, it would seem possible from Fig. IV.8 that higher topped clouds contribute more mass to large-scale circulations. This result is consistent with, but not necessarily implied by, previous results presented above. Differences in theoretical heating profiles between young and mature convection in which mature convective heating exhibits a greater magnitude at high altitudes [e.g. *Schumacher et al* 2004] also imply a similar result.

Anvil air detrains into clear air with a maximum available altitude dictated by cloud top height. Once fully detrained to clear air, parcels will descend at a rate dictated by longwave radiative cooling [e.g. *Kuang and Hartmann*, 2007]. If it can be assumed that no dynamic descent is forced in clear air, then the descending time scale for air is a function of a parcel's height and ability to interact with radiation (dependent on water vapor content both locally and in the column above the parcel [*Igel* 2011]). Of course, it cannot be assumed with much confidence that clear air descent is unforced near any particular cloud. However, it is hoped that for the ensemble of clouds for which this analysis is valid that the assumption is at least acceptable as an avenue for understanding the active physical processes. First discussing the clear-sky

momentum tendencies, to first order, water vapor content decreases exponentially with height in the moist tropics. Since drier air has less impetus to cool by longwave emission than moist air, higher air has both more depth through which to descend and less motivating force to do so. Now linking the clear-sky to the cloudy-sky mass flux, if the upper-level winds in the direction of the large-scale circulation are constant over a layer deep enough to capture most of the detrained anvil air, then parcels with longer descent times will reach their minimum height farther away from the core. *Riehl and Malkus* [1958] implied that hot towers are the driver of far-field circulations and *Gray* [1973] and *Houze* [1982] implicated MCSs. From the data, it would appear that since wider cloud objects tend to be taller, the suggestion by *Gray* [1973] and *Houze* [1982] might be correct and that MCSs are more impactful to large-scale circulation. This result does not take into account the much greater population of the smallest cloud objects than of the large. It could still be that due to the relative infrequency of MCSs, they are less important to the climate system despite their more important role per object.

3.5 Two-Dimensional Histograms

Two-dimensional histograms (2DH) are examined here. The 2DHs span a height-reflectivity space. However, rather than showing the frequency of height-reflectivity bin occurrence across all cloud objects, these 2DHs show per cloud object frequencies. The contributions from all cloud objects are included in the initial frequency distribution and then the counts in each bin are normalized by the number of cloud objects. Number densities therefore represent the average number of occurrences within each bin, within each object. This method represents another way of viewing an “average cloud.” It should be emphasized that these 2DHs are not normalized at every height like the familiar CFADS of *Yuter and Houze* [1995].

In this chapter, the relationship between cores and anvils has been a central focus. As such, 2DHs can be used to expound on some of the sensitivities of anvils and cloud objects in general to either pedestal width or core counts. Figure IV.9 shows 2DHs for cloud objects with 1-2 cores and 4-5 cores within the pedestal in an effort to separate out the reflectivity signatures of cloud objects that exhibit less and more organization respectively. Figure IV.9c shows the normalized difference of the 4-5 core 2DH minus the 1-2 core 2DH. Cloud objects with more cores exhibit anvils that are thicker with a less homogeneous relationship between height and reflectivity. Cores are less well defined, as indicated by the lack of a strong “bullseye” of frequency centered at 10 dBZ and level 20 in Fig 9b, and yield a generally weaker reflectivity. Otherwise, the 2DHs are remarkably similar which implies that analyzing cloud objects regardless of horizontal extent and number of cores, which is often done in this dissertation, is justifiable for an instrument like CloudSat. Of course, the similarity is also partially a function of the measurement instrument sensitivity and attenuation characteristics as well as the explicit assumptions made in *Chapter II*.

In *Chapter III*, the sensitivity of Cloud objects to sea surface temperature (SST) was assessed with respect to a variety of climate-response hypotheses. High morphological sensitivity to SST was shown. That focus inspires an examination here of cloud object 2DHs binned by SST regime. As in *Chapter II*, SSTs are defined for the approximate center of the cloud object from the ECMWF analysis data appended to the CloudSat granules. Figure IV.10a and b show 2DHs for SSTs of 299K - 300K and for SSTs of 302K – 303K. Figure IV.10c shows the normalized difference. Here the trends with SST are quite clear, even if rather small. With increasing SST, the amount of low-reflectivity, high-altitude anvil cloud increases while the heaviest core reflectivities decrease in frequency. The results of *Chapter III* suggest that the

positive region in upper levels is the result of anvils getting thicker with increasing SST. The locally-significant negative region in the core is more curious. It seems to be the result of narrowing pedestals with increasing SST by a few kilometers per degree SST and a stronger decrease (by $\sim 10\%$) in core number (neither shown), which would imply narrowing cores and consequently fewer occurrences at the high reflectivity bins per cloud object. That with increasing SST cloud objects exhibit fewer cores and narrower pedestals but deeper anvils could imply invigoration of individual cores as climate warms. This result was hinted at in *Chapter III* with the identification of a Thermostat-like response [Ramanathan and Collins, 1991]. Though, the effects of attenuation from thicker anvils should be considered.

3.6 Simulation Results

It is worth testing some of these observationally derived conclusions against results from the RCE simulation. In principle, none of the above results are in any way built into RAMS. However, if the RCE simulation exhibits some of the same pedestal-anvil behavior, then a compelling case can be made that these results are in some way fundamental to the physics of clouds at scales resolvable even at 1km horizontal grid spacing.

Attempting to compare model results and observational results from CloudSat introduces several problems. First, at low levels especially, the simulation exhibits a higher resolution than do the CloudSat observations. Second, the simulation results are not subject to attenuation or any random sampling errors. This leads us to suggest that only certain kinds of comparisons between the simulation data and CloudSat are likely to be warranted. We attempt to identify the 2/3 relationship in the model, which relies on easily observable and highly accurate data in both datasets and explain the physical processes occurring at the anvil base.

3.6.1 Simulated 2/3 Scaling

To examine whether the RCE simulation exhibits a 2/3 scaling, an RCE object identification and anvil cutoff algorithm were run over the model output from the equilibrated period of the simulation. Cloud objects were defined to be contiguous cloudy grid boxes of total condensate mixing ratios of greater than 0.01 g kg^{-1} that stretched from 1km above the surface to 11km in order to be consistent with the CloudSat data. They are sampled along the long axis of the simulation to yield 2-dimensional width-height cross-sections reminiscent of the CloudSat objects. An anvil cutoff height was determined for each RCE cloud object by subjecting each object to the cutoff algorithm [*Chapter II*] used on the CloudSat objects with only minor changes made to accommodate the different data. Results are shown in Fig. IV.11. It can be seen that while a 2/3 scaling does exist in the simulation data, it is perhaps less well constrained. The range of cloud sizes for which this analysis is valid is much less than observed by CloudSat due to constraints imposed by the domain size. However, it is encouraging that such a relationship is evident at all.

3.6.2 Anvil Dynamics

To investigate the controls of anvil morphology, a composite cloud has been made from the simulated output. Figure IV.12a shows the composite cloud vertical velocity field in colored contours and the median cloud outline in thick white. The slight asymmetry of the anvil is due to a small mean shear that is established by the convection over the course of the simulation. The horizontal dashed line indicates the mean level of the objectively found anvil-cutoff height. The most striking result of this composite is the collocation between the maximum velocity and the anvil-cutoff height. Figure IV.12b shows the horizontal divergence implied by the vertical velocity composite in Fig. IV.12a. Through this application of anelastic continuity (for

simplicity) it can be seen that horizontal divergence occurs at all levels in the convective column above the vertical velocity maximum. Consequently the base of the anvil occurs at the level of the velocity maximum as air is dynamically forced outward above this level. Figure IV.12b shows that maximum divergence occurs just below the tropopause layer (14-18 km) [Fueglistaler et al, 2009]. The maximum in divergence might be a result of capping or neutral buoyancy processes. Certainly this idea cannot be rebutted conclusively here. However, it can be suggested that the vertical asymmetry in horizontal divergence is unlikely to result from cloud vertical velocity maxima colliding with a level of neutral buoyancy. In the tropics where temperature profiles are rarely very far from moist-convectively neutral stability, the level of neutral buoyancy is unlikely to be strictly deterministic. In fact, the results of *Takahashi and Luo* [2012] suggest only a weak control by the level of neutral buoyancy on tropical deep convection.

Additionally, it could also be asked why the velocity maximum and anvil base, occur at the height they do. We suggest it is the result of microphysics within the pedestal. Previous analyses have shown that the mid-tropospheric velocity maximum in deep convection is the result of latent heating of deposition and condensation [Fierro et al. 2012; Storer and van den Heever 2013; McGee and van den Heever 2014]. This heating positively accelerates convecting air parcels. Figure IV.12c confirms this assumption. The figure shows a composite of depositional and condensational heating rates from a subset of the simulation for which this information is tracked. It is important to remember that depositional heating results in an *acceleration* of the velocity field and so should be maximally important below the level of peak velocity. Because of the accumulated acceleration due to deposition, the vertical velocity peaks at ~8 km. Above the velocity peak, air begins to diverge horizontally and to form an anvil.

3.6.3 Fixed Lower-Anvil Temperature

In *Chapter III*, it was shown that anvil base temperature remains fixed across different SSTs. This response was dubbed the Fixed Lower-Anvil Temperature (FLAT) hypothesis. Previously, it was suggested that some balance might exist at the lower edge of the anvil between a variety of temperature-dependent diabatic processes that would keep mean anvil base temperature constant across a wide range of deep convective clouds. The RCE simulations seem to indicate that the arguments in *Chapter III* are potentially only partially correct. The parameterized processes that control microphysical deposition onto ice species are strong functions of temperature in RAMS [*Walko et al 2000*] and reality [*Wexler 1977*]. Therefore, the anvil base may be assumed to occur where it does due to the temperature dependent level of acceleration from vapor deposition. This temperature level would be the same regardless of surface or climate conditions. The validity of FLAT could be further tested in the future by altering the temperature dependence of deposition in RCE and other numerical simulations.

It should be noted that the mean height of the velocity maximum seen in these clouds is somewhat lower than in recent observations by *Heymfield et al [2010]*. The maximum is ~9 km in the simulated clouds and ~10.5 km in the subset of oceanic clouds in their Fig. 7c. Although, the results here are not dissimilar quantitatively or conceptually to those presented in *Mapes and Houze [1995]* and *Yuter and Houze [1995]*. However, much of their convection seems to reach generally higher heights than the clouds in this simulation which often top out around 14 km. So, the cloud population among all these studies may be slightly different. Furthermore, the differences observed are only indicative of height, not temperature – which is the more important quantity to the arguments being made for FLAT. Finally, it will be noted that FLAT implies that the total depth of anvils may not only be the consequence of mass building down from the anvil

top's being capped by the tropopause or level of neutral buoyancy but also from a bottom up process resulting from the convergence of mass at the midlevel velocity maximum.

3.7 Basic Sampling Caveats

Two specific caveats to many of the conclusions above should be discussed – the effects of daytime-only sampling and the effects of near-meridional sampling by CloudSat. It is well established that differences exist between daytime and nighttime clouds even over ocean [e.g. *Gray and Jacobson, 1977; Yang and Slingo, 2001; Liu et al, 2008; Waliser et al, 2009*] where the high thermal capacity of the ocean surface layer should minimize daily fluctuations in surface fluxes. As such, the scales of convection listed above are only strictly relevant for clouds occurring at 13:30 local time. The 13:30 sampling may bias the results to a particular lifecycle stage of clouds and/or to a certain size. Since *Sassen et al [2009]* suggest little difference in convective activity between day and night over ocean, their higher cloud fraction during night may be attributed to larger clouds. This result would indicate that enumerated cloud length scales in this study are smaller than they would be at night if all high clouds were attached to pedestals. *Liu et al [2008]* find differences in the relationship between raining cores and total cloud cover between night and day. This result would imply that the $2/3$ scaling is potentially only relevant during the daytime as well as that the measured scales of cloud components are only representative of daytime values. Obviously, the shortwave heating rates discussed in *Chapter III* are only meaningful for the 13:30 solar zenith angle. It would be useful in the future to include observations from the nighttime overpass if the issues discussed in *Chapter II* can be mitigated.

The second concern is that because CloudSat observes primarily along a north-south line that measurements of length scales are biased if clouds have a preferential orientation that does

or does not align with the sampling. This issue is discussed additionally in Section 5.2. The primary concern arises from the preferential orientation of deep-layer shear in the tropics along the zonal direction both in the mean and during specific weather situations. It is thought that this shear will act to blow an anvil away from its parent pedestal. While the effects of shear are discussed at length in *Chapter V*, it will be mentioned here that it does appear to be a significant predictor of morphology and so its anisotropy is worth considering. Because shear is primarily zonally oriented, the (meridional) measurements of width above could be consistent underestimates. If true, this could lead to the volume estimates in *Chapter II* being potentially somewhat unrepresentative. Depending on the precise mean orientation of highly organized systems with respect to shear (and sampling), measures such as the number of convective cores in a system could also be biased. This consideration that the combination of meridional sampling and the geometric arguments made in section 6.2 might result in a significant underestimate of convective cores should be made. A geometric under sampling of cores might be artificially raising the average anvil width for low-core number clouds. Shear is crucial to many aspects discussed above. However, it is impossible to know its importance with the current observing system. The launch of a future CloudSat-like instrument with a different sampling orientation would be the only way to assess the sampling bias' importance. The zonal orientation of shear and its influence are discussed additionally in *Chapter V*.

4. Conclusions

The discussion above has focused on analyzing cloud scales from a unique CloudSat dataset of mature deep convective clouds [*Chapter II*]. The “average cloud” discussed was seen to be fundamentally different than the perceived average cloud, as generally thought of in the

highly subjective, informal cloud poll (Fig. IV1). These differences arise for several reasons. First, the vertical partition of pedestal and anvil depths is assumed to be different than in reality. In nature, clouds are much more equally distributed in the vertical between anvil and pedestal. Most cloud objects do not resemble the deep-pedestal with shallow-anvil cloud often depicted. Nature also tends to generate clouds that are much wider than imagined. Both the pedestal and anvil widths were underestimated by those surveyed. The underestimation of width could have wide ranging implications from the validity of scale separation assumptions in parameterization schemes, especially as grid scales shrink with increasing computing power, to the climate implications of tropical deep convection. Overall, personal impressions from the poll tend to show understandable biases. The vast majority of convection that individuals are likely to observe is isolated, young, continental convective clouds which are inherently skinnier and exhibit narrower anvils than seen in this large scale, temporally long data set. Larger storms typical of the mean storm observed here with CloudSat are likely to be more difficult to observe non-scientifically. Gauging the physical size of such a large cloud would be difficult. Also, obscuring visual reference, clouds will often stretch to the horizon.

A central goal of this chapter was to better understand the interrelationships between and among various components of deep, convective clouds through the detailing of length scales. Of primary consequence was the scaling relationship exhibited between anvil and pedestal widths that was shown to follow a $2/3^{\text{rd}}$ power. This particular power led to the suggestion that deep convective clouds flux convective mass through a cylindrical convective pedestal into a spherical (more likely, ellipsoidal) anvil such that the $2/3^{\text{rd}}$ power is a fundamental result of 3 dimensional space. A recasting of the data into rank-ordered pairs showed that the $2/3^{\text{rd}}$ scaling could potentially provide a physically based anvil area parameterization for large-scale models.

Anvil top height was examined in an attempt to determine which kinds of tropical clouds (single-core or MCSs) are more likely to contribute to large-scale circulations. It was found that MCS (multi-core) generally obtain higher cloud top heights than single cells and could in principle more easily detrain air to farther afield per cloud object. Finally, some of these CloudSat results were compared with results from a large domain RCE simulation. While the statistical fit was not as good as in the observations, a $2/3^{\text{rd}}$ scaling was still apparent in the simulation data. The temperature dependence of depositional growth of ice species was implicated as a potential explanation for the FLAT response seen in *Chapter III*.

As cloud pedestal width grows, a number of morphological and physical changes appear to occur in cloud objects. The anvil will widen but at a slower rate than the pedestal. The number of cores will increase, the base height will drop, and the cloud top will rise. Thus, the growth of the pedestal width presents much the same tale as the temporal evolution of the cloud system. This theory, the stretched building block hypothesis [Mapes *et al* 2006], is, in contemporary understanding, well established locally. However, this study which utilizes 5 years of tropics-wide data serves to illustrate the theory's applicability to the global tropics. It was suggested that as pedestal width grows, individual cloud objects become increasingly influential to circulations and precipitation – a result that also compliments contemporary theory.

5. Sampling Issues

It has been implicitly assumed throughout the analysis that CloudSat's curtain-type sampling of clouds does not introduce any biases in the data. In this section, we will show that the effects of sampling along track do not affect greatly the kinds of relationships derived above.

5.1 Off Center Sampling

It has been assumed throughout this manuscript that clouds objects are quasi-circular in the horizontal and it will be assumed here. Figure IV.A1 shows a potential anvil/pedestal combination in plan view. The outer circle is meant to trace the edge of the anvil; the inner circle traces the pedestal edge. The radii of the pedestal and anvil are labeled as R_p and R_a , respectively. Thus, the true anvil radius to pedestal radius ratio is R_a/R_p for the object in the figure. The gray lines labeled A-D represent possible CloudSat orbits that would sample this cloud object. Transect A would not yield a cloud object as it does not sample the pedestal. However B through D would result in cloud objects. Each sample of this single cloud would yield a different pedestal to anvil width ratio. But how important is this?

Determining this is mathematically tractable. If the sampled radius of the cloud is defined to be along the x-axis, with the sampled pedestal distance defined as x_p and the sampled anvil distance defined as x_a , then the equation of the circles defined by R_a and R_p at any y value are:

$$R_p^2 = x_p^2 + y^2 \text{ and}$$

$$R_a^2 = x_a^2 + y^2.$$

Upon trivially rearranging and taking the ratio of x_a to x_p :

$$\frac{x_a}{x_p} = \sqrt{\frac{R_a^2 - y^2}{R_p^2 - y^2}}.$$

Figure IV.A2 shows the result of this equation for values of R_a and R_p of 100 km and 50 km, respectively. This results in an assumed ratio of R_a to R_p of 2-to-1. Values in Fig. IV.A2 are normalized by this ratio (i.e. $[x_a/x_p]/2$). Curly braces will be used below to indicate a value is normalized by the true ratio, R_a/R_p . The value of 2 in the figure exaggerated the importance of sampling issues as the lower this ratio is, the higher the mean x_p to x_a since the ratio depends on

the difference between R_a and R_p . It can be seen from Fig. A2 that while the true R_a/R_p is 2 that the measured x_a/x_p is everywhere higher than 2 {1}. However, for the lowest 90 percent of ratios the mean x_a/x_p is 2.4 {1.20}. While for the lowest 50 percent of ratios, the mean x_a/x_p is only 2.1 {1.04}. This is a mean high bias of only 10% for the lowest 50% of samples. But, a R_a/R_p of 2 is actually rather low. For a more physically relevant R_a/R_p of 10 like that of the “average cloud” from above, the mean x_a/x_p below the 90th percentile is 12.8 {1.28}, and the 50th percentile mean x_a/x_p is only 10.7 {1.07}.

Given these values, it is possible to artificially resample our data. By creating PDFs of all relevant real R_a/R_p and randomly sampling from among and within these distributions to adjust our cloud objects, we get these new PDFs of pedestal widths and anvil widths. Each data point is randomly sampled from within the PDF at values of R_p less than x_p . This process is run many times and new, synthetic data sets are created. The new, raw datasets look similar to the original dataset except for an approximately linear shift toward higher synthetic x_p and lower x_a/x_p .

For a wide variety of true R_a/R_p values, it can be shown that only the top 10% of x_a/x_p values are likely to be greatly affected by sampling biases. If these top 10% are synthetically eliminated from the dataset, a new scatter can be created. While the precise regression fit changes to reflect the lack of high x_a/x_p 's (higher slope, lower intercept), the linearity of a $x_a/x_p^{2/3}$ fit is little diminished. The biggest concern is that these measurement biases somehow yield an artificial 2/3 scaling in our data, but this does not appear to be the case analytically or numerically.

It will also be mentioned here that fractal theory would suggest that any cloud edge is not perfectly circular [*Lovejoy, 1982*]. Cloud area is a function of diameter as

$$A = \sqrt[1.35]{(\pi D)^2}$$

with the obvious functional deviation from the equation for a circle being the 1.35 power root. The addition of this root would complicate our results. It would imply that the degree to which our assumption of circularity becomes less good for larger cloud component widths. There may be some evidence of this in the rank ordered data. When extended out to very large diameters (700 km), the linearity of the scattered data decreases.

5.2 Non-Circular Objects

There also arises the issue of non-circular but still geometric anvils in the horizontal plane. *Cetrone and Houze* [2006] state that their echo objects were often oriented at +/- 45° to the pole once only objects with an ellipsoidal axis ratio of 1.5 or greater had been accounted for. The mean axis ratio of their ellipsoidal echo objects was 2.4. *Liu and Zipser* [2013] find that ~70% of their precipitation features (approximately a “cloud object” here) have axis ratios between 1.5 and 10. The radius measured of an ellipse at 45° to its major axis is

$$R_m = \sqrt{2 a^2 b^2 / (a^2 + b^2)}$$

Upon applying the results of *Cetrone and Houze* [2006], R_m becomes 1.31. The area of the actual echo object would be $\pi * 2.4$ whereas the implied circular area would be $\pi * 1.31^2$ or $\pi * 1.70$. This means the circularity assumption could be off by as much as -40% on average. However, if we assume the variance is such that the orientation varies from 30 to 60 with regularity, then the assumption will be off by -53% to +10% with radii factors or 1.26 to 2.63. Thus assuming anvils are circular is likely to under-represent their area. However, their measured radii should be acceptably representative of the characteristic radius of any individual object. And again, it should be reiterated that these calculations are for objects that are preselected to be ellipsoidal and for *mean* not *median* values of axis ratios. So while admitting the potential bias in certain

quantities observable from the dataset developed in Chapter II, it will be stated that only worst case scenarios are likely to be of concern. What is truly unknown is the frequency of these worst case occurrences. The *Cetrone and Houze* [2006] results would indicate that they do not constitute the majority of cases, but this is impossible to know for sure.

5.3 Gridding Size

In keeping with geometric arguments, presented here is a brief discussion of why measuring length scales is a more relevant practice than examining areal coverage (i.e. cloud fraction) in some coarse geographic binning method. For example, cloud coverage data are often examined as a percent cover in 1 degree boxes. It just so happens, that the average cloud (Table 1) has a length scale that is on the order of 1 degree (~100 km). Unfortunately this coincidence leads to some ambiguity in coverage. An anvil cloud with a 100km diameter in a concentric areal grid box 100 km on a side would have ~80% coverage. If that cloud increased in length by 10% and its areal coverage by 20%, some of it would extend into the adjacent boxes. The coverage in the box concentric to the cloud would increase to ~87% coverage while the four surrounding boxes would now exhibit 2% coverage. So, the resultant analysis of the areal increase would be 2-7% depending on the 1-degree box despite the actual areal coverage increasing by 20%.

This problem could be solved in two ways. Analysis regions need to be either much larger or much smaller than the average convective cell. For example, 1-degree boxes would be much smaller than the typical MCS and so would not result in much error. Or, boxes should be ~5 degrees such that the 10% increase in length example as above does not leak out of box edges. Or, cloud object techniques, like the ones employed in this study, should be used when assessing length scales due to the continuousness of length scales.

6. Tables

Table IV.1: Means of various length scales as a function of the number of cores. 3+ signifies that values are for cloud objects with 3 or more cores. Standard deviations of each measurement are in parentheses.

Cores	Pedestal Width (km)	Anvil Width (km)	Cutoff Height (km)	Anvil Depth (km)
1	11 (7)	95 (98)	7.2 (1.5)	6.4 (1.5)
2	20 (9)	121 (101)	7.3 (1.4)	6.7 (1.5)
3+	116 (109)	335 (243)	7.1 (1.4)	7.7 (1.6)

Table IV.2: Means of various length scales and number of cores as a function of binned pedestal width. Standard deviations of each measurement are in parentheses.

Pedestal Width (km)	Mean Pedestal Width (km)	Anvil Width (km)	Cutoff Height (km)	Anvil Depth (km)	Cores
<25	14 (5.9)	104 (106)	7.2 (1.4)	6.5 (1.5)	1.6 (1.2)
25-50	36 (71)	175 (124)	7.2 (1.4)	7.2 (1.5)	3.4 (1.9)
>50	156 (119)	414 (250)	7.0 (1.3)	8.0 (1.5)	10.9 (8.5)

Table IV.3: Means of various length scales and number of cores as a function of binned base height. The >1000 m row constitutes less than 1% of the cloud objects. Standard deviations of each measurement are in parentheses.

Base Height (m)	Pedestal Width (km)	Anvil Width (km)	Top Height (km)	Cores
<500	96 (114)	282 (250)	14.6 (1.3)	7.0 (8.3)
>500	40 (58)	175 (174)	14.1 (1.3)	3.3 (4.5)
>1000	14 (12)	10 (9.4)	13.7 (1.0)	1.6 (1.1)

7. Figures

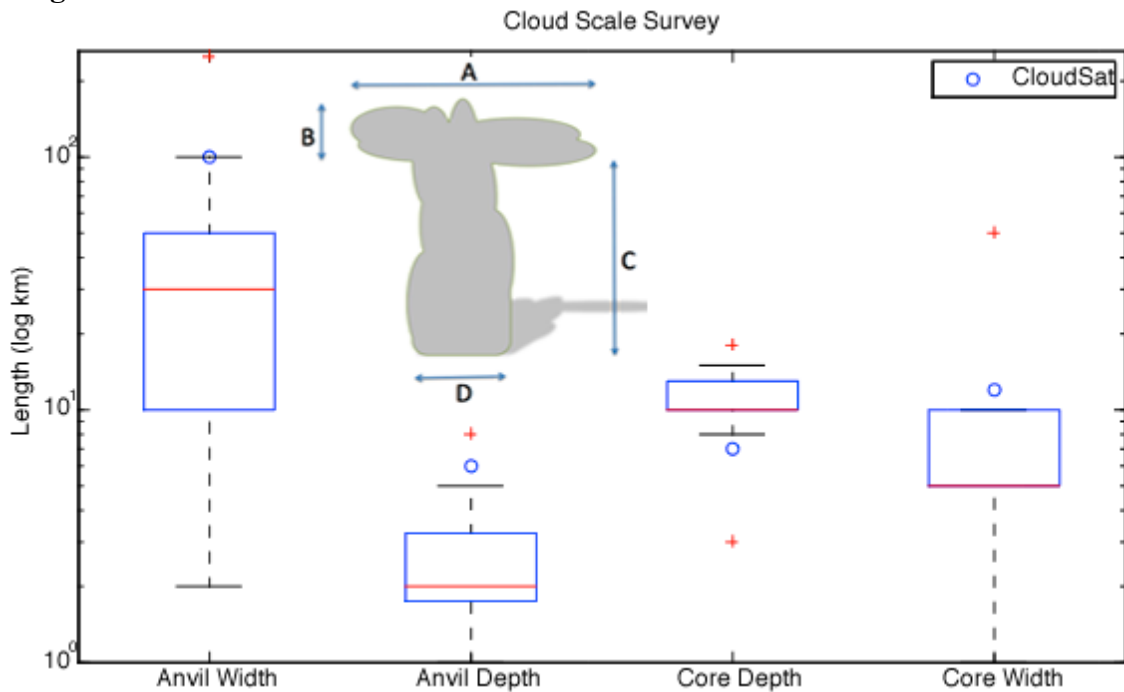


Figure IV.1: An informal poll was taken within the Department of Atmospheric Science at Colorado State University. The poll asked questionees to detail how large they thought various components of an average tropical deep convective cloud over ocean are. The scales cloud survey takers were asked to identify: (A) the anvil width; (B) the anvil depth; (C) the pedestal depth; and (D) the pedestal width. The results of the cloud survey shown in box and whisker plots with the red line being the mean and red '+' symbols being statistical outliers. The blue circles show the results from CloudSat reported in Table 1.

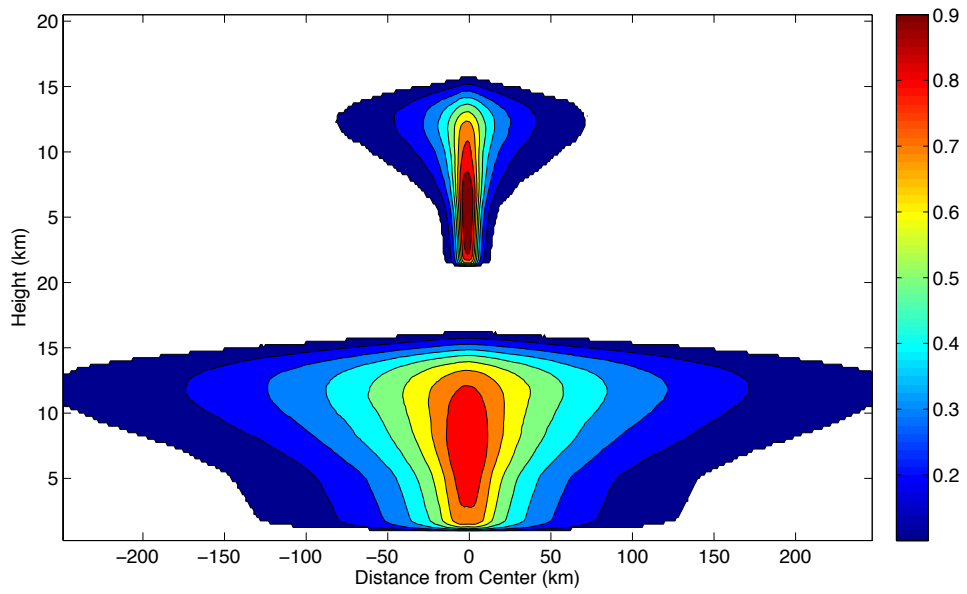


Figure IV.2: Overlap percent for cloud objects of 1 (top), and 2 or more identified cores (bottom). The compositing method is detailed in Chapter II.

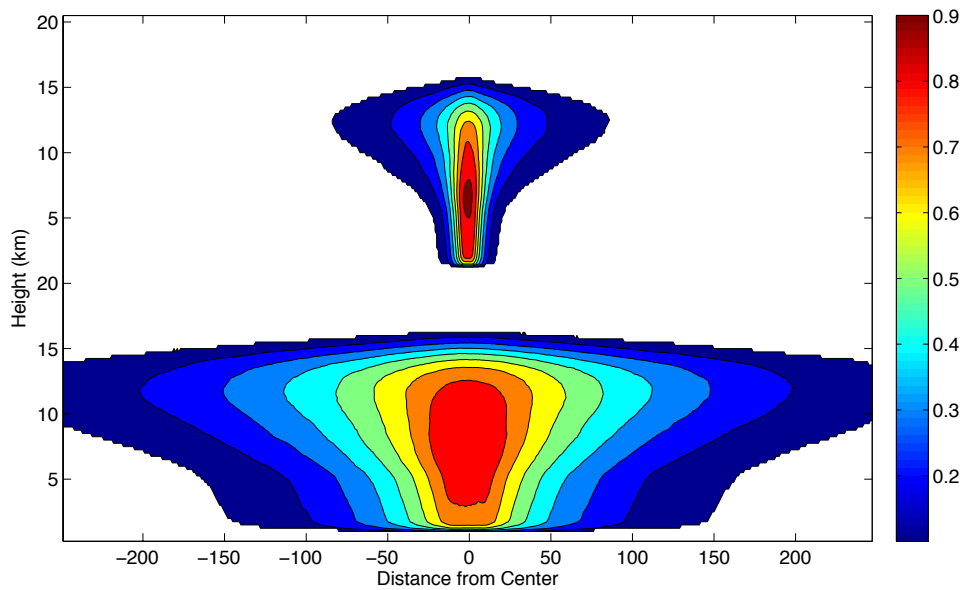


Figure IV.3: Overlap percent for cloud objects with pedestal widths of less than 25km (top) and greater than 25km (bottom).

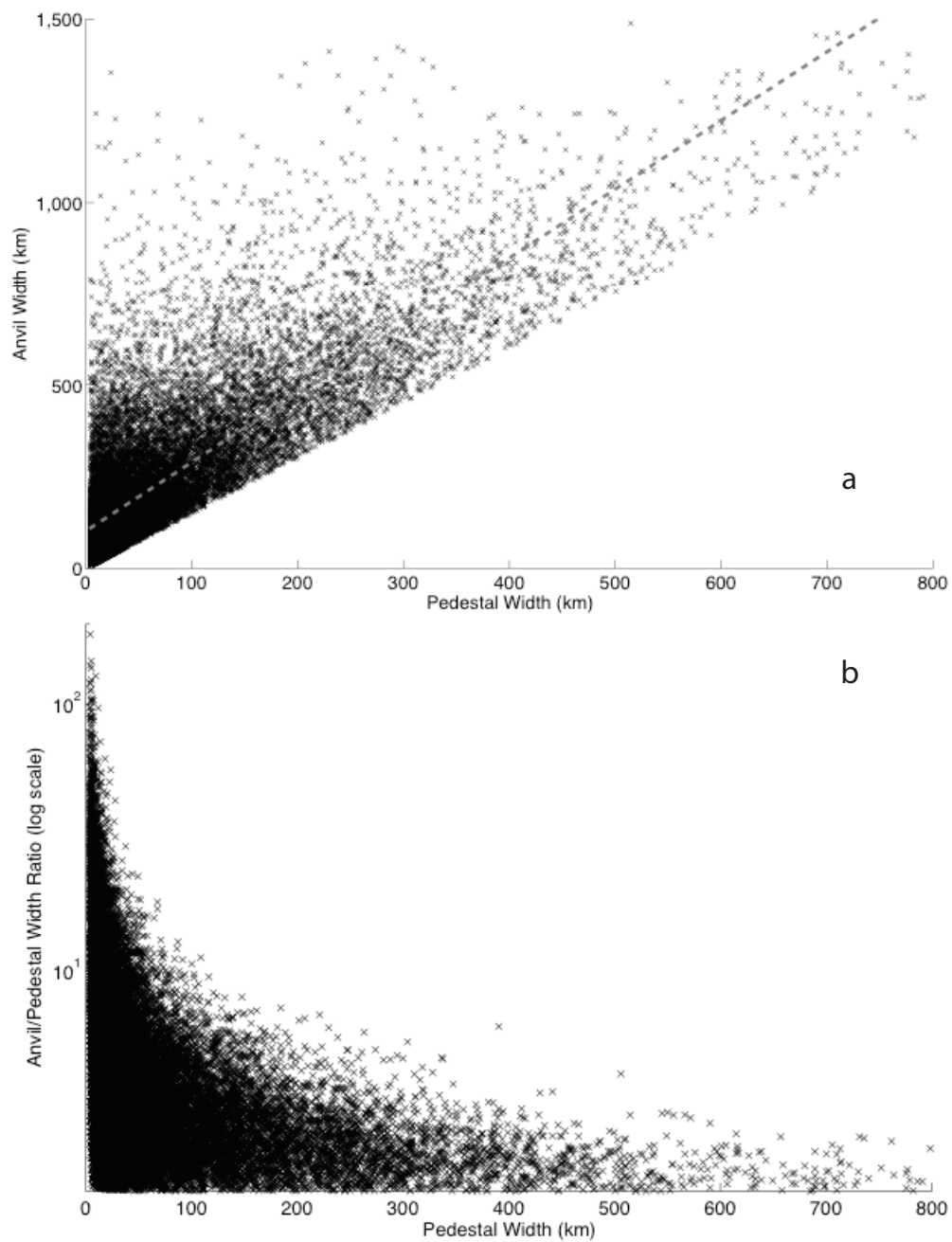


Figure IV.4: a) Scatter plot of cloud object anvil and pedestal width pairs up to 1 500km and 800 km, respectively. The gray dashed line is a linear best fit to the data. The best fit has a slope of 1.9. 75% of the population lies in low-valued pairs with pedestal widths less than 100 km and anvil widths less than 500 km. b) Scatter plot of the ratios of anvil width to pedestal width.

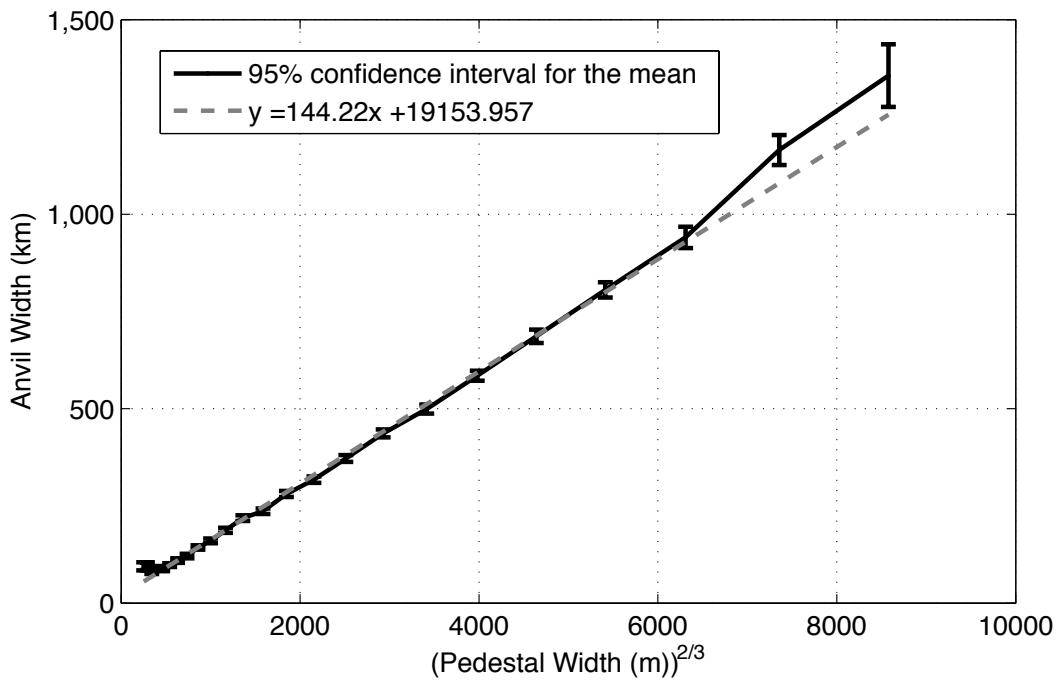


Figure IV.5: The black solid line illustrates the mean anvil width binned by base width. Error bars show the 95% confidence interval for the mean. The gray dashed line shows the linear best fit to the data. Note that abscissa is pedestal width to the 2/3 power.

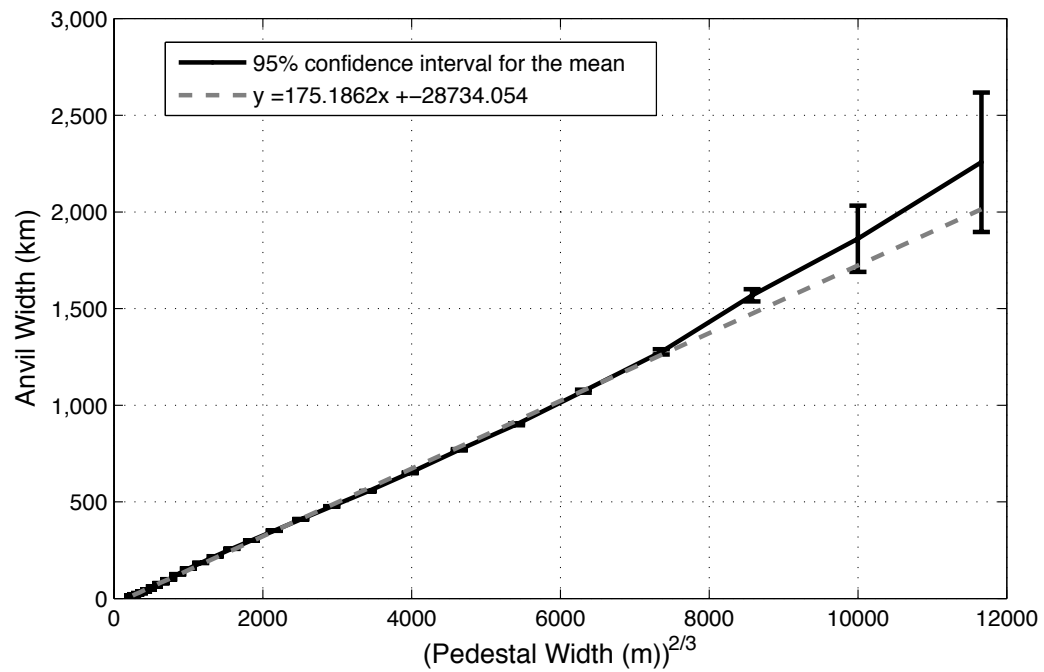


Figure IV.6: Same as Fig. IV5 except for the rank ordered and re-paired data.

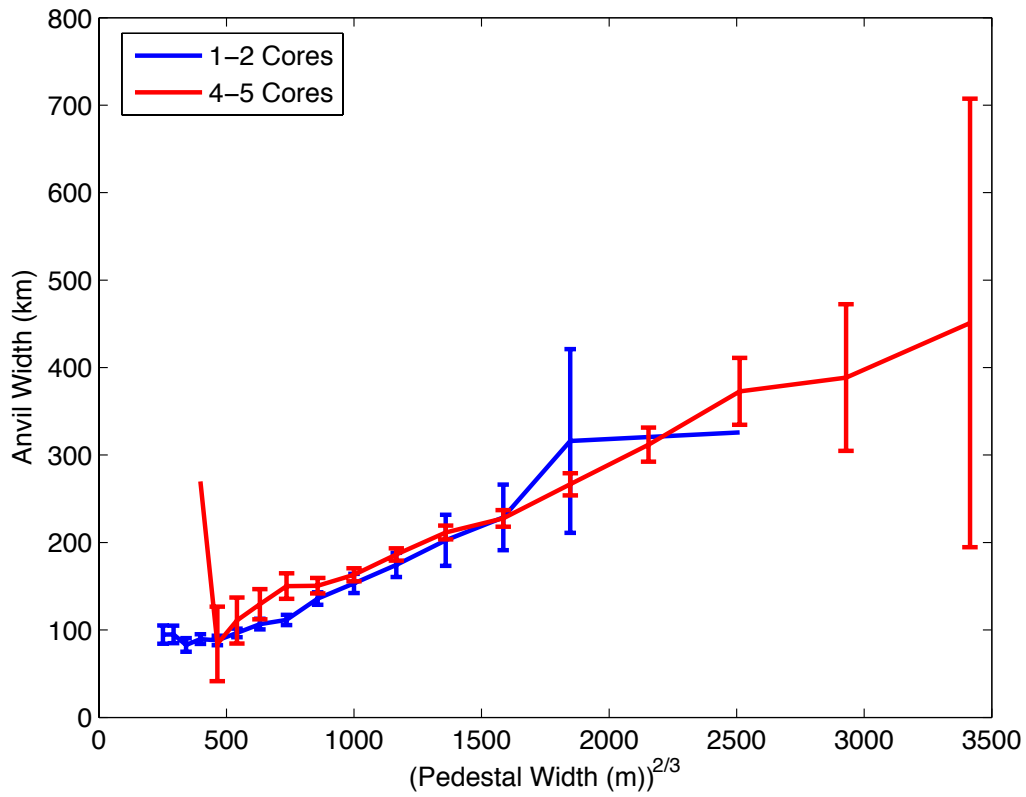


Figure IV.7: Same as for data plotted in Fig. IV.5. The blue data are for cloud objects with 1 to 2 identified cores. The red data are for those with 4-5 cores.

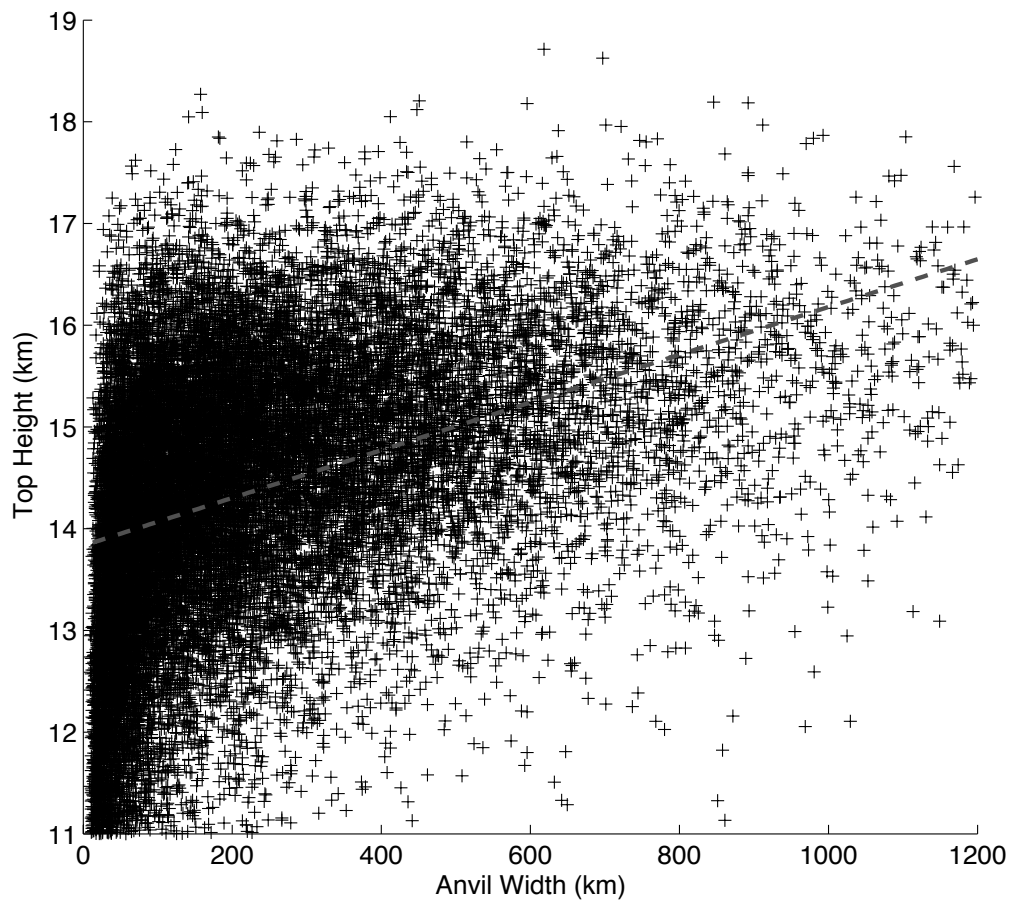


Figure IV.8: A scatter of cloud object pairs of anvil width and top height. The data have been truncated to the region that exhibits frequent occurrences.

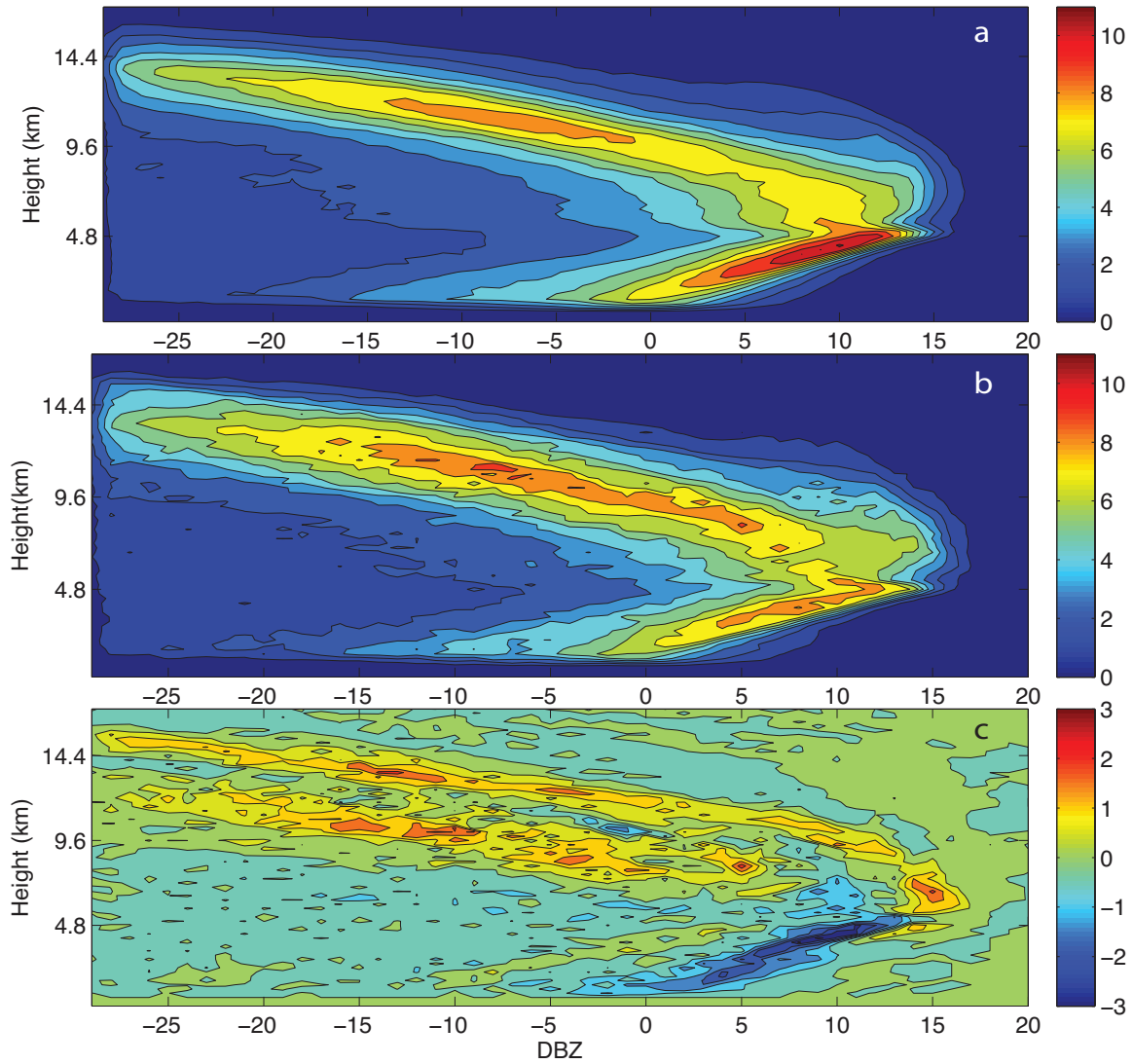


Figure IV.9: 2DHs per object by binned core counts. The contoured values show the average number of occurrences within each bin *per cloud object* for each core count bin. Contour bins are 1dBZ by 1 CloudSat level. The vertical scale is CloudSat levels above the surface. a) 1-2 Cores. b) 4-5 cores. c) The simple difference of values in (b) minus those in (a).

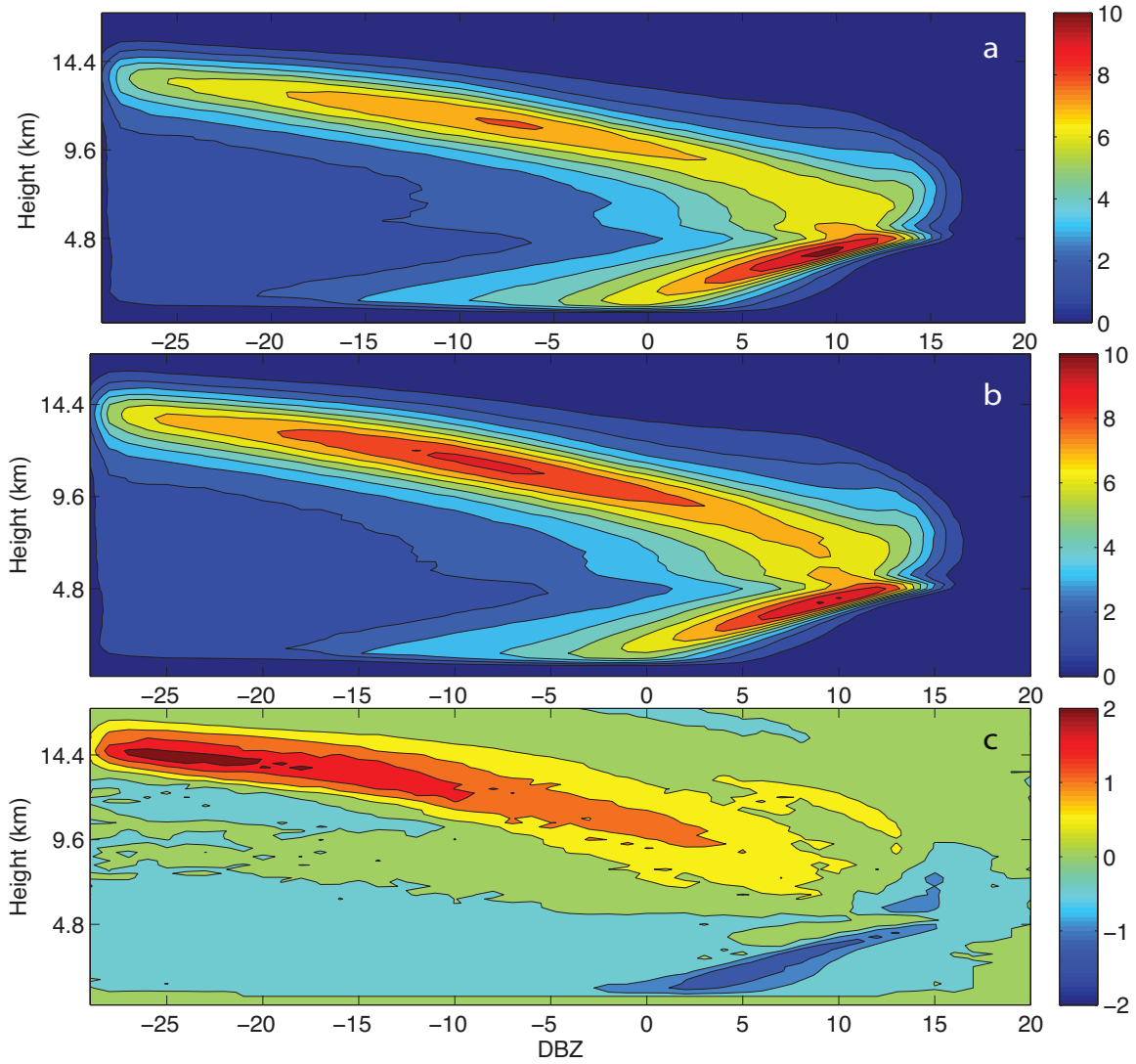


Figure IV.10: Same as Fig. IV9: but for various SST ranges. a) SSTs between 299K and 301K. b) SSTs between 301K and 303K. c) same as Fig 9.

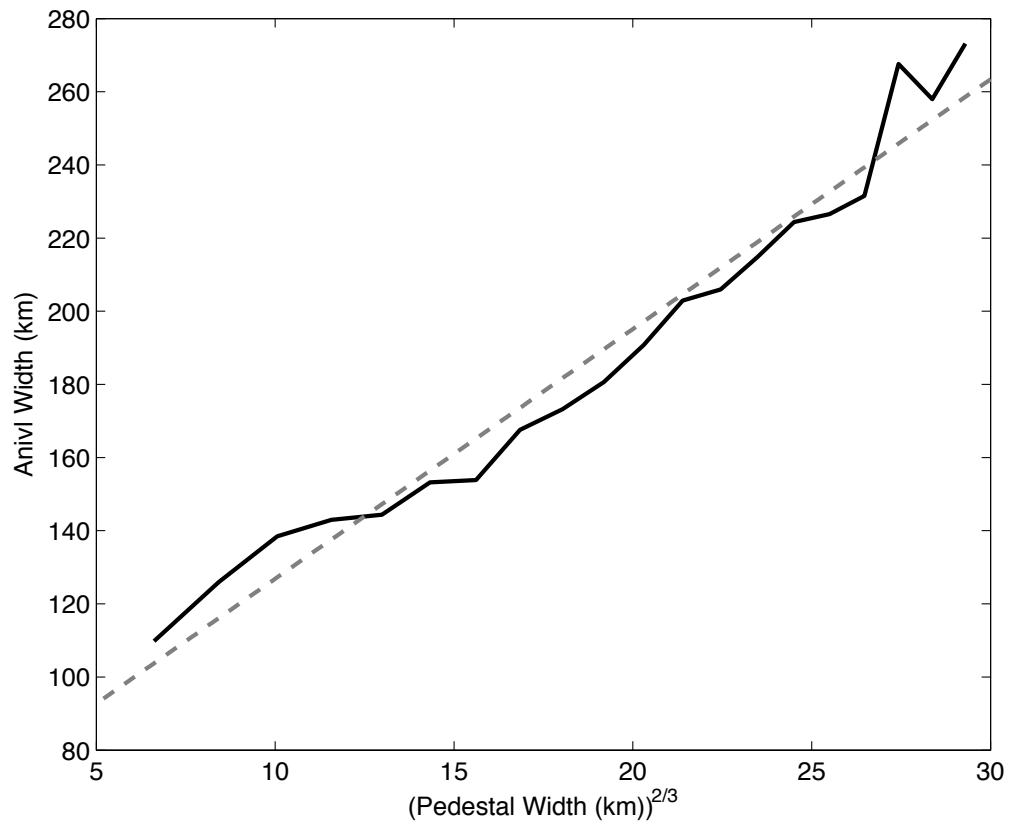


Figure IV.11: Mean anvil width as a function of binned pedestal width to the $2/3^{\text{rd}}$ power in black. A linear fit is shown in the gray dashed line.

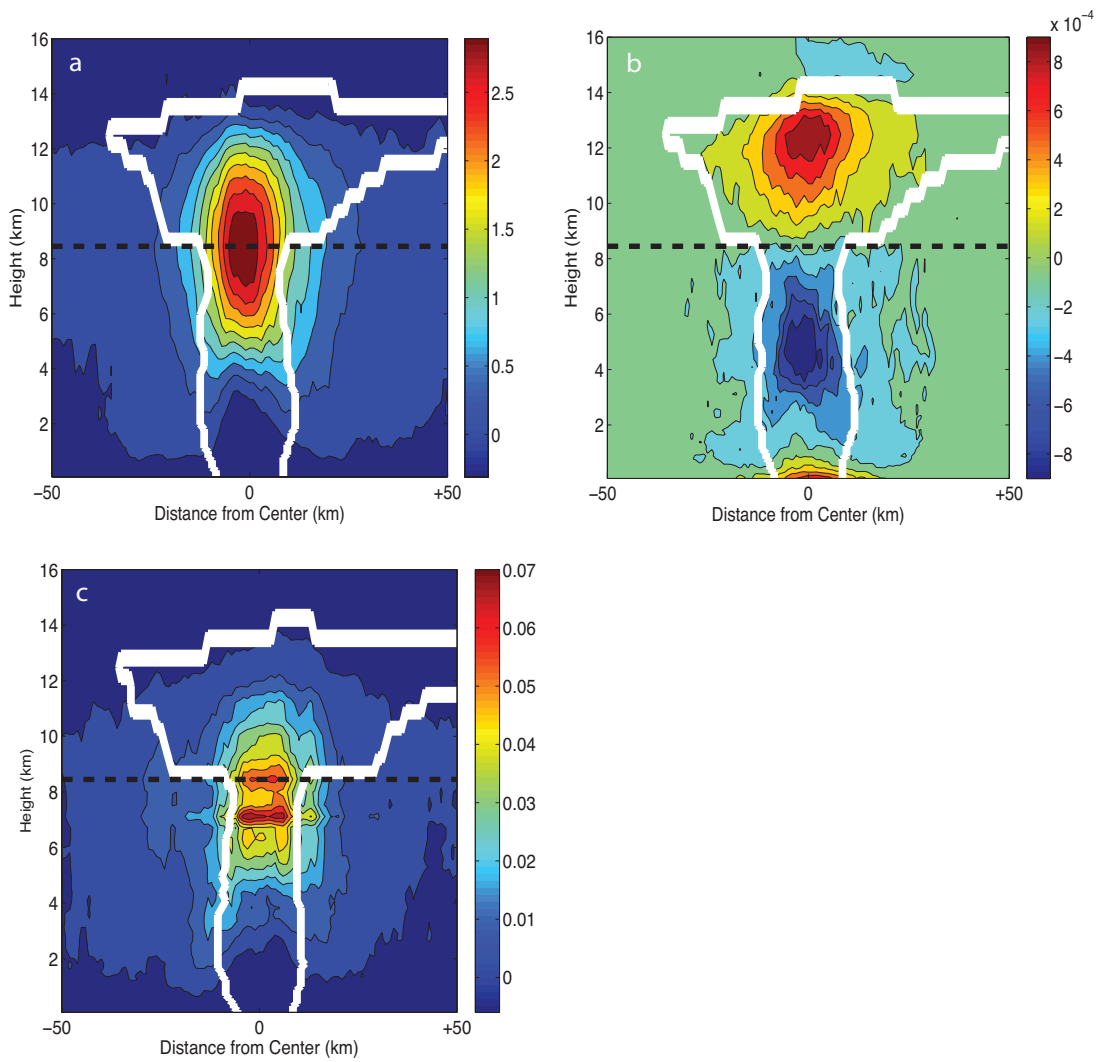


Figure IV.12: a) composite of vertical velocities in colored contours, 50th percentile cloud outline in white, and mean anvil cutoff height in black dashes. b) composite of mean horizontal divergence. c) composite of mean depositional heating rates (K/hr) from only the final 5 days of the simulation.

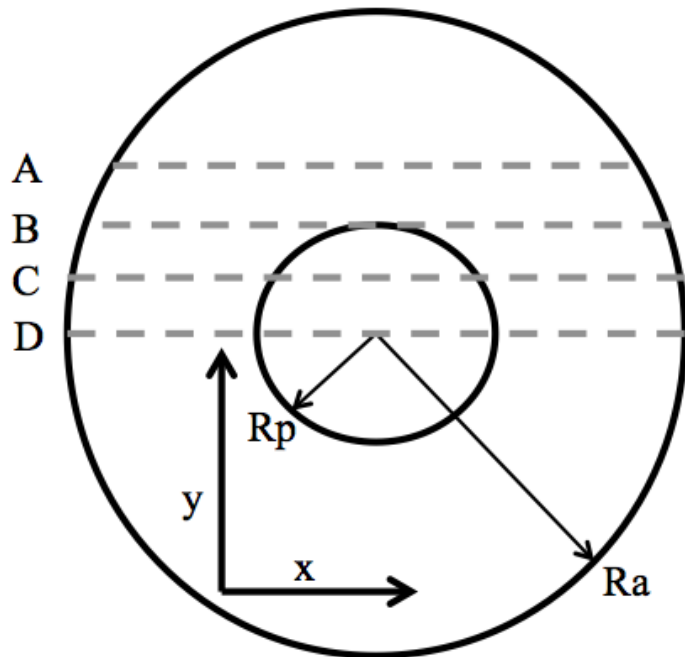


Figure IV.A1: A potential plan view of a sampled cloud object with the outline of the convective pedestal and anvil in the thick, black circles. These have actual radii of R_p and R_a , respectively. Dashed, grey lines A-D are possible sampling tracks of CloudSat of this cloud object. Coordinates are labeled with the x-axis along the sampling path

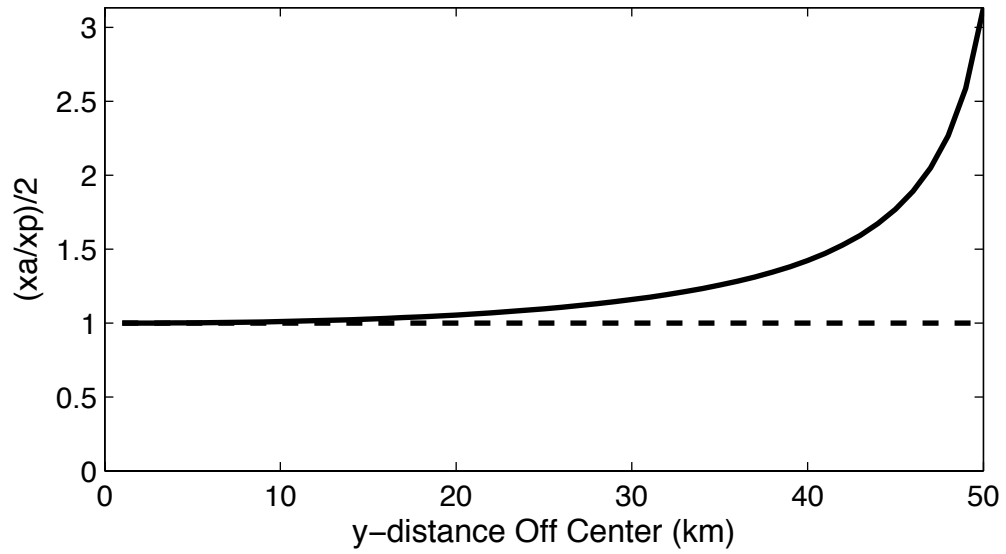


Figure IV.A2: The factor by which off-center sampling affect a cloud object with Ra of 100km and Rc of 50km as a function of off-center distance.

CHAPTER V: THE SENSITIVITY AND RELATIVE INFLUENCE OF ENVIRONMENTAL CHARACTERISTICS TO DEEP CONVECTIVE MORPHOLOGY OBSERVED BY CLOUDSAT

1. Introduction and Background

So far, the affects of the meteorological environment on clouds have largely ignored in the examination of cloud scale populations, of climate influences, and of morphology. This chapter seeks to rectify this fact by adding additional data to each cloud object. In doing so, the influence of the meteorological environment on deep convective cloud size and shape is ascertained.

Deep, moist convection occurs within many meteorological environments and regimes over the open tropical oceans. Because of the importance of these clouds, it is crucial to understand their sensitivity to their local environmental characteristics. Some work has focused on the sensitivity of the bulk effects of clouds such as precipitation or cloud cover to local meteorological environment in the tropical, oceanic atmosphere [*Saxen and Rutledge, 2000*], while a limited number pursue quantifying the sensitivity of composite cloud morphology to such variables [*Riley et al., 2011; Masunaga, 2013*]. In this chapter, we focus on examining the sensitivity of the morphology of individual clouds to various near-field environmental characteristics. How this premise and the one used in *Chapter II* integrate is discussed in *Chapter VI*.

The question may be asked as to why such properties of the cloud matter? The size and shape of clouds influence the resultant effects of the clouds on the immediate atmospheric state.

For example, a cloud with a higher, and hence colder cloud top, emits less radiation to space than does a lower cloud which results in a locally enhanced warming of the column. Examining cloud size and shape may also provide insight into the inner workings of deep convective clouds [e.g. Nesbitt *et al.*, 2006; Liu and Zipser, 2012; Chapters II-IV]. Determining simple relationships between clouds' morphology, local meteorological environment, and the physics that govern them are crucial to improving parameterization methods of deep convection for use in weather and climate models. As stated previously, much of what is known about the size and shape of deep convection below anvil top has been derived from ground-based radar data gathered during several seminal field studies [Houze Jr. and Cheng, 1977; Brown and Zhang, 1997; DeMott and Rutledge, 1998; Demott and Rutledge, 1998; Johnson *et al.*, 1999; Del Genio and Kovari, 2002]. These campaigns often allowed for the collocation of sounding data in order to characterize the environment of the radar derived morphology data. However, while thorough and in-depth investigations were performed on these datasets, such field studies are limited in their spatial and temporal coverage.

The exact morphology of any individual deep convective cloud is a function of many variables. Cloud occurrence and morphology are assumed frequently to be strong functions of external variables, such as convective available potential energy or shear. This chapter examines the impacts of such external variables on cloud morphology. Because the potential parameter space of external influences on convection extends to many dimensions, several previously postulated direct environmental influences on convection are examined here. These are:

- (i) *Convective available potential energy* (CAPE). CAPE is often used as the primary driver of convection in parameterization schemes of convection [Arakawa, 2004; Yano and Plant, 2012]. The reason for its frequent use is that it links the energy cycle of the

atmosphere with convection in a very direct manner. CAPE represents a potential upper limit on the amount of latent heat of condensation that a cloud can release in any particular environment. Therefore, it is canonically argued that that more CAPE should yield deeper and wider clouds. The problem with this interpretation becomes that CAPE is an upper limit to energy release and no physical process requires convection to reach this limit. In the moist tropics, CAPE is often found to have a “skinny” profile [*Lucas et al.*, 1994; *Cetrone and Houze*, 2006]. As a consequence, energy release tends to be slow and steady as convection develops vertically and a cloud is susceptible to having its growth stunted by various processes such as entrainment of drier air.

- (ii) *Shear*. The term “shear” is used throughout this paper to mean the vertical shear of the horizontal wind. Shear has been shown to affect the dynamical flow structures around deep convection [*Moncrieff and Miller*, 1976; *Rotunno et al.*, 1988; *LeMone et al.*, 1998; *Weisman and Rotunno*, 2004; *Coniglio et al.*, 2006]. Different magnitudes of shear can result in different storm types and orientations [*Barnes and Sieckman*, 1984; *Johnson et al.*, 2005; *Cetrone and Houze*, 2006]. One of the defining results of the TOGA-COARE field campaign conducted in the early 1990s was the attribution of storm morphology to shear, including the fact that more highly sheared clouds are often assumed to have wider anvils as the anvil is advected away from the main convective region [*Hildebrand*, 1998; *Halverson et al.*, 1999; *Saxen and Rutledge*, 2000a; *Rickenbach et al.*, 2008].
- (iii) *Mid-level vertical velocity (ω_{500})*. ω_{500} is indicative of several physical occurrences potentially influential to convection [*Bony et al.*, 1997; *Peters et al.*, 2013; *Kumar et al.*, 2014]. First, through continuity arguments, ω_{500} can be taken to imply the magnitude and sign of surface convergence. High surface convergence can act as a direct dynamic

trigger for convection; it can also act as a potential convective trigger through increasing low-level moisture. Second, ω_{500} is broadly diagnostic of the convective state. A negative ω_{500} potentially indicates the existence of convection, and a more negative ω_{500} probably indicates the existence of stronger convection or of broader spatial coverage of updrafts.

- (iv) *Aerosol concentration* (AOD, as aerosol optical depth will act as a proxy for concentration [Andreae, 2009]). Aerosol amount is often assumed to impact convection through its influence on the total latent heat release of deep convective storms [Andreae et al, 2004; Khain et al, 2005, van den Heever et al, 2006, Koren et al, 2008, 2010; Storer and van den Heever, 2013]. Through a process commonly referred to as “aerosol induced convective invigoration”, high number concentrations of aerosol may delay warm rain processes thus allowing more water to loft and freeze. This increase in freezing results in more in-cloud net latent heat release and higher updraft velocities. Higher vertical velocities might then result in higher cloud tops and/or more detrainment. For a comprehensive review of aerosol effects on deep convective clouds see Tao et al. [2012].

Between these environmental influences, (i)-(iv), there is also interesting evidence for complicated mutual regulation of clouds [e.g. Fan et al., 2009; Storer et al., 2010, 2014; Wall et al, 2013]. Because of the particular analysis method used here, several other potential influences on convective morphology are examined also and compared to factors (i)-(iv) in an effort to be more exhaustive in this analysis. These include location and sea surface temperature.

The influences of these environmental parameters on convection are examined through the analysis of trends in convective length scales. Analysis as simple as enumerating anvil

widths and cloud top heights (CTH) has been the goal of this dissertation and has resulted in multiple insights into the inner workings of convection [Chapters II-IV]. Finally, it is noted that the results included in this chapter are not meant to be conclusive for all clouds. The dataset examined has a very strict applicability to mature, deep convection over tropical oceans. This strict applicability results from the highly selective identification of clouds. This benefits the discussion. It allows us to examine a very specific subset of clouds important to the properties of the over-ocean tropical atmosphere in a way never before possible.

2. Methods

This study makes use of two families of data. One set of data includes details on individual deep convective clouds, while the other dataset contains information about the characteristics of the meteorological environment in which each cloud occurs. The environmental measures come from multiple sources, which are discussed at the end of this section. The approach to combining the cloud and environmental data is detailed in §3.

2.1 Cloud Data

The Cloud dataset used is the one developed on *Chapter II*.

2.2 Environmental Data

The environmental dataset makes use of a variety of observational and reanalysis platforms. AOD is taken from the Moderate Resolution Imaging Spectroradiometer (MODIS) [Remer *et al*, 2005] onboard the Aqua satellite. Collection 5.1 data is used at 10km resolution. Because MODIS is aboard Aqua in the A-Train, the observation of AOD occurs nearly simultaneously to the CloudSat observation. Only the highest quality assured (QA) data are used

in order to limit the influence of cloud contamination. This necessarily means that the aerosol and cloud are not precisely collocated.

CAPE values are calculated from profiles of temperature and humidity from the Atmospheric Infrared Sounder (AIRS) instrument onboard the Aqua satellite [Aumann *et al.*, 2003]. The aim of AIRS data is to provide measurements within 1K RMS and 20% RMS for temperature and relative humidity, respectively [Suskind *et al.*, 2006]. Data are taken from the AIRSX2RET product version 6. Depending on the surface and tropopause characteristics, relevant data are recorded on ~12 standard vertical pressure levels spaced ~100hPa apart. Due to the relatively coarse vertical resolution of the components contributing to the CAPE calculation, it is undertaken in a simple way so as to converge for every profile. CAPE is calculated between the lowest available level of data (very often the bottom layer) and the AIRS observed tropopause level. The equivalent potential temperature of the lowest layer is calculated and then the vertically integrated deficiency of equivalent potential temperature at each level above the lowest up to the tropopause is converted to equivalent CAPE. Thus, this method represents an absolute upper limit to the real CAPE. Other methods for calculating CAPE were attempted including iterative techniques. Ultimately, the simple CAPE calculation described above was chosen due to its successful convergence for every single column. Its interpretation is also easy as it is totally unambiguous. The QA values of ‘Good’ and ‘Best’ were used since a statistical approach is taken in this study. The distribution of CAPE values is similar to that noted previously [Ye *et al.*, 1998; Roff and Yano, 2002].

Both shear and ω_{500} are obtained from the European Center for Medium-Range Weather Forecasting (ECMWF) ERA-I reanalysis product [Simmons *et al.*, 2007]. The shear value for any column is calculated as the magnitude of the vector difference between two layer vector-

averaged winds. These two layers are the surface layer, 1000hPa to 900hPa, and the anvil outflow layer, 300hPa to 100hPa. The sensitivity of the results to the choice in layers is discussed in §4.3. ω_{500} is simply the vertical pressure velocity at 500hPa.

3. Theoretical Framework

In this study, simple relationships between observed environmental characteristics and tropical, deep convective clouds are sought. Both cloud and environmental quantities are assessed from instantaneous measures, which limits the strict attribution of cause. However, in order to infer such relationships, it is assumed that given enough clouds and enough observations of environmental quantities that physically meaningful statistical relationships between clouds and environments can be created that offer insights into the physical processes at play. Caution must be exercised in attempting to take the implications of these relationships too far [Gryspeerd *et al.*, 2014b]. Therefore, throughout what follows, appropriate caveats are provided alongside the proposed relationships. The overarching goal, however, is to try to gain insight into the dependence of clouds on their near-field environment.

Each environmental dataset in §2 is obtained at its highest possible resolution. MODIS is acquired at level-2 resolution, 10 km. AIRS is obtained also at level-2 resolution, 45km at nadir. ECMWF 0.75° (~80km) data are used. These data are therefore of a spacing comparable to the size of convective pedestals $O(10\text{km})$ and anvils $O(100\text{km})$, which implies some actual horizontal resolution of spatial features in the near-convective environment outside of QA issues.

These environmental data need to be collocated with the cloud objects in some way. Given the central location of a cloud object from the database [Chapter II], the nearest available measurement (observation or reanalysis) is found. For gridded data from ECMWF, the

collocation requires an assessment of time and of location. First, the nearest time is found; then the nearest pixel from that time slice is selected. For swath data, from AIRS and MODIS, only spatial displacement is considered. All the swath data from the day on which the cloud object occurred are constructed onto a grid at the data's native resolution. The nearest pixel to the cloud object with quality assured data is taken as the value for that cloud. Since AIRS and MODIS are both part of the A-train, the observation times of the cloud and environment are close.

Other studies have used interpolation to fill in missing data, to stitch together granules from observations, or to infer temporal evolution from gridded, time sliced data [Meskhidze *et al.*, 2009; Koren *et al.*, 2012; Gryspeerd *et al.*, 2014a]. This approach is not taken here as it is not obvious how to do this in a self-consistent way or even what kind of interpolation is appropriate in either time or space. The atmosphere could act in many different, potential non-linear ways. The ultimate result of the approach described is the addition of environmental information to cloud objects in a simple, but logically consistent way. The approach should not introduce many uncertainties or errors beyond those inherent in the retrievals or reanalysis.

Finally, it should be noted that the analysis is performed with respect to existing cloud objects. As in *Chapter III*, no attempt has been made to account for changes in the frequency of clouds with respect to different environmental conditions. Analyzing frequencies, total sky coverage, or changes in lifetime would be impossible given the nature of this CloudSat data subset. Therefore, while simple trends are examined, caution is required in extending the results beyond what they actually show.

In the first part of the analysis below, cloud morphology trends with respect to the environment are conducted with each environmental variable in isolation from the others. For

example, trends with increasing AOD and CAPE are shown without any attempt to understand the covariations in AOD and CAPE that might be dependently working to yield the observed trend. In the second part of the analysis, possible covariations between environmental variables are then taken into account.

With the particular variables analyzed, CAPE, shear, AOD, and ω_{500} , we have tried to span an environmental parameter space across which theory suggests potential convective sensitivity. *Jones and Christopher* [2010] spanned an even larger parameter space in their attempt to assess the sensitivity of low clouds to AOD. Their results would suggest that in some cases the environmental data included here are only a subset of the potentially influential factors affecting cloud morphology. Nevertheless, the goal of this chapter is to further understand existing deep convection-environmental relationships.

4. Results and Discussion

4.1 Single Variable Trends

4.1.1 CAPE

First, we examine the dependencies of deep convective morphology on CAPE. Figure V.1a-f shows six different morphological trends as a function of CAPE. Similar figures are recreated for all of the environmental predictors, so it is worth describing the structure of Fig. V.1. Each panel shows a different aspect of cloud morphology plotted as a function of the observed environmental CAPE in two ways. The red line is a linear regression fit to the entire data scatter of each individual morphology-environment pair. The blue line shows mean morphological quantities for cloud data binned to the nearest thousand CAPE value. 95% confidence intervals are then calculated within each bin. These are then plotted with error bars.

In the case of CAPE, bin sizes are chosen so as to evenly span the range of data. Therefore, some bins only have few contributing data. Again, specifically looking at Fig. V.1, the very first bin, -1000 J/kg, has only five contributing data while the middle bins often have thousands. The -1000 J/kg bin and the highest AOD bin (Fig. V.2), which only has seven data pairs, are the least populated bins across all the various environmental predictor bins by a full order of magnitude, but these bins are included for completeness. The low CAPE bin has a very large spread (Fig. V.1) and should probably be discounted, but the high AOD bin (Fig 2) often fits with trends. No other bin has fewer than 80 data pairs. The red trend line provides an unambiguous tendency in the data, and the blue line is included to provide statistical information about the data in lieu of showing the full scatter plot of data pairs. While the same data go into computing both lines, the red regression fit is *not* computed directly from the blue, binned data.

Trends in cloud morphology are discussed and are arranged in Fig. V.1 from the cloud top down. That is, they start with cloud top properties in (a) and move downward to cloud base properties in (f). The trend in CTH with CAPE is shown in Fig. V.1a. Over the range of CAPE values in the data, CTH is seen to increase by approximately 100m from ~14.35km to ~14.45km. This is likely due to the enhanced potential buoyancy of high CAPE atmospheres. Although an increase in CTH is observed, a larger trend may have been expected (discussed in §4.4). Anvil width decreases slightly from ~250km to 230km. Mean anvil ice water path remains approximately constant in the red, regression fit but decreases somewhat in the blue, binned data. Taken together, these results imply that anvils tend to get slightly higher and narrower with increasing CAPE but remain as dense. In Fig. V.1d, anvil base temperature is shown to be nearly constant. Figure V.1e demonstrates that the trend in the number of identified convective cores within each convective pedestal is slightly negative. A decreasing number of cores would

seem to indicate that higher CAPE environments favor individual, isolated, single core cloud objects over clusters or mesoscale convective systems, although this would be in contrast to that found in midlatitude storms [Weisman and Klemp, 1982]. The trend in cloud base height with increasing CAPE is interesting. The red, regression fit decreases by 20m while the blue, binned data generally decreases but in a non-linear way. A decreasing cloud base height could imply that as CAPE increases, rain is more intense, which leads to more subcloud layer cooling [Masunaga, 2013], or that updrafts are stronger and therefore initiate cloud at lower heights, or that boundary layer RH is higher and the lifted condensation level is lower.

4.1.2 AOD

Cloud morphology trends with increasing aerosol concentration are analyzed using Fig. V.2 with an eye toward identifying evidence of aerosol invigoration. CTH increases substantially as AOD increases (Fig 2a). The red, regression fit increases by ~1km over the range of AOD included here. Increasing CTH with increasing AOD is physically consistent with aerosol invigoration of deep convection [Andreae et al, 2004; Khain et al, 2005, van den Heever et al, 2006, Koren et al, 2008, 2010; Storer and van den Heever, 2013] and with past results from CloudSat [Storer et al, 2014]. Anvil width also tends to increase with increasing AOD. The combination of increasing CTH and anvil width with increasing AOD has been observed and discussed previously in Koren et al. [2010] with different methods. Fan et al. [2013] postulated that since clouds in more polluted environments have smaller hydrometeors due to the increase in the number of particles able to serve as cloud condensation nuclei, anvils get wider because smaller hydrometeors could advect farther from the parent convection before precipitating. IWP exhibits an interesting behavior that is somewhat unique to AOD. The red, regression line decreases while the blue, binned line decreases before increasing significantly.

These are actually somewhat independent behaviors since the AOD data is highly skewed toward low values. In this particular case, the binned data are more indicative of the behavior exhibited by the statistical scatter of the data at high AOD. So, at high AOD, there seems to be an increase in mean IWP with higher AOD while at lower AOD it decreases. This dependence is remarkably similar to *Storer et al* [2014](their Fig 4d). This result, along with the wider anvils, would imply more lofting of moisture in the clouds with highest AOD – a result consistent with aerosol induced invigoration of updrafts and observed in *Storer and van den Heever* [2013]. Anvil base temperature increases slightly although the total trend is of a smaller magnitude than many of the error bars. While a warming anvil base would seem inconsistent with invigoration, the potential implication of this result is discussed in the next paragraph. Figure V.2e shows that the number of convective cores per cloud object increases with increasing AOD. A similar result was suggested by *van den Heever et al* [2011]. This could be due to the strengthening of weaker updrafts in the presence of enhanced aerosol concentrations. Or, this could be the result of some upscale process by which invigoration creates higher levels of organizational structure in the storm due to the wider or higher anvils (Fig. V.2a & 2b). Finally, Fig. V.2f shows that at low AOD, increasing AOD may lower cloud bases [as in *Wall et al.*, 2014] but that beyond an AOD of ~ 0.4 , that there is no discernible trend.

Returning to the possible increase in anvil base temperature, the result seems counterintuitive as it might be expected that invigoration would result in colder (higher altitude) anvil bases. We will argue that it is not. In *Chapter IV*, it was postulated that the temperature at which anvil base occurs is a consequence of the maximum in depositional heating occurring at a defined temperature just below anvil base. Aerosol could, in principle, affect the precise temperature at which this maximum occurs by affecting microphysical process rates. If aerosol

invigoration is occurring at high AOD, then more numerous, smaller hydrometeors of both a higher cumulative mass and cumulative volume are freezing heterogeneously within the updraft. These hydrometeors will continue to advect upward at the invigorated, higher vertical velocity. Deposition onto a distribution of particles that is higher in number and total mass occurs at an unambiguously higher rate [Meyers *et al*, 1997; Pruppacher and Klett, 2010]. Therefore, the maximum in deposition will occur at a lower altitude and higher temperature. Thus, not only could more latent heat of deposition be released due to a greater mass of hydrometeors advecting above the freezing level, but also this latent heating could be occurring at a faster rate and at a lower height and higher temperature.

In summary, the AOD-morphology trends are broadly consistent with the idea of convective invigoration. Storms get taller and wider and contain more anvil ice. Also noteworthy is the relatively high magnitude of some of the AOD trends in comparison to the weak trends seen in the CAPE discussion previously.

4.1.3. ω_{500}

Mid-level vertical velocity trends are shown in Fig. V.3. For consistency, trends are discussed with respect to increasing pressure velocity (increasing subsidence). The population of ω_{500} is clustered mostly between values of -0.3 hPa s^{-1} and 0.2 hPa s^{-1} with a median value that is slightly negative at $-0.035 \text{ hPa s}^{-1}$. This indicates a slight preference for cloud objects to occur in ascending regimes. This is discussed in greater detail in §4.3. Interestingly, the results below often show a subtle difference between the red, regression fits and the blue, binned data at the extreme ends of the ω_{500} regime. At this time, we have no specific explanation for this behavior other than to suggest that individual clouds may respond non-linearly outside of nearly neutral

ω_{500} environments. The high percentage of cloud objects occurring in low magnitude ω_{500} regimes would suggest a preference to occur at these near-neutral values.

Figure V.3a shows the trends in CTH as a function of mid-level pressure velocity. As the flow becomes increasingly subsident, CTH tends to decrease. The red, regression fit decreases more substantially than the blue, binned data, but both decrease by $\sim 1\text{km}$ over the range of ω_{500} . This CTH trend makes physical sense as environmental velocity becomes increasingly subsident, CTH vertical growth is stunted [Bony *et al.*, 2004]. Anvil width is one of the morphological measures for which the blue and red lines behave somewhat differently. The regression decreases by $\sim 30\%$ while the binned data decreases then increases. For the regression fit, it would seem that as the environment becomes more characterized by subsidence, anvils are becoming narrower. However, in the binned data the global minimum in anvil width is actually at 0 hPa s^{-1} . This would mean that increasing the magnitude of ω_{500} would seem to favor wider anvils regardless of whether the air is rising or sinking. Certainly upward velocities could logically favor wider anvils by delaying hydrometeor fallout and through enhanced convective mass flux and detrainment, but how downward velocities do so is unclear. Anvil IWP is more logically consistent in its dependence on ω_{500} ; it generally decreases with increasing mid-level pressure velocity. Given that anvil base temperature rises slightly (Fig. V.3d) with increasing ω_{500} , it would seem that this decrease in IWP can be attributed to shallower anvils arising from the decrease in CTH. The fall in anvil base temperature due to invigoration by ω_{500} (now, with respect to decreasing ω_{500}) stands in contrast to the rise associated with AOD. This result serves to emphasize the potential importance of the microphysical influence in the AOD results. The number of cores drops as subsidence increases (Fig. V.3e) which is indicative of the idea that rising air leads to a better chance of convection [Bony *et al.*, 1997, 2004; Zelinka and

Hartmann, 2009] in the tropics. The cloud base height measure is not especially telling. It increases slightly for mid-range of ω_{500} values, but the total trend is less than the error bars for those three bins. At the extremes of ω_{500} , cloud bases seem to lower significantly.

4.1.4 Shear

Figure V.4 shows trends with respect to increasing troposphere-deep vertical shear of the horizontal wind. As stated above, the total shear is the magnitude of the vector difference of the mean winds between a surface layer (1000hPa to 900hPa) and the upper levels (300hPa to 100hPa). Of note is the general consistency between the binned data and the regression fits throughout Fig. V.4. As such, it is suggested that shear is a good monotonic predictor of cloud object morphology as has been found using other methods [Rotunno *et al.*, 1988; LeMone *et al.*, 1998; Weisman and Rotunno, 2004; Coniglio *et al.*, 2006].

Since all of the trends in morphology are consistent between the regression fits and the binned data, and since the trends form a cohesive picture of how the dynamics of clouds depend on shear, all of the trends are listed next and then discussed. As shear increases, CTH decreases, anvil width increases by close to a factor of two, IWP decreases, the anvil base temperature increases, the number of cores increases, and the base height decreases. As observed elsewhere [Halverson *et al.*, 1999; Saxen and Rutledge, 2000; Rickenbach *et al.*, 2008], with increasing shear, anvils tend to become wider as they are blown away from parent convection. The anvil thickness decreases for the same reason. Not only do their cloud top heights decrease, but it would also appear that their base heights decrease as well. This fact indicates that shear tends to shrink storms vertically by enhancing horizontal widths at the expense of vertical development. The increase in core number is consistent with the observations that shear provides a means of storms organization [Saxen and Rutledge, 2000; Houze, 2004]. The decrease in base height is

consistent with the other vertical scales decreasing, but it is not obvious why we see such a result.

4.2 Trend Attribution

In this section, the relative importance of each of the environmental variables discussed above is compared for each of the morphological trends presented. The goal is to determine which environmental factors contribute the most to cloud size and shape. Knowing which environmental characteristic or characteristics are the most influential to cloud morphology could serve to inform convective parameterizations. For example, if AOD is shown to be the most influential factor in determining CTH, then the trend shown in Fig. V.3 could be used as a first order predictor of that quantity.

The trend attribution is done with a series of multiple-linear regressions. Environmental measures are used as “predictors” for morphological “dependents.” All the predictors are normalized so as to occur over a range of (0,1) so that the regression coefficients can be compared easily. A higher regression coefficient therefore indicates a greater sensitivity of the dependent variable to the respective predictor. Despite this normalization, the statistical distributions of various predictors over the range (0,1) are often very different. For example, AOD is highly skewed toward zero while ω_{500} is nearly normally distributed about 0.5. Finally, once regressions are computed, the coefficients are all normalized by the magnitude of the most significant predictor to ease interpretation. R^2 values for the regressions are often low given the spread in the dependent data, but residuals are often approximately Gaussian, so these values are not a cause for concern from a statistical point of view.

Sea surface temperature (SST) and latitude is now added to the predictors already discussed. SST was used in *Chapter III* as a dependent variable for convective morphology and

is suggested by *Ramanathan and Collins* [1991], *Demott and Rutledge* [1998], and *Lindzen et al.* [2001] as being influential to convection. Latitude is included as a proxy for time-mean global-scale flow regime. Not surprisingly, in *Chapter II*, it was shown that the number of cloud objects exhibited a pattern in latitude similar to total cloud fraction as a function of latitude [*Sassen et al.*, 2009]. They did not show any trends in morphology as a function of latitude.

A priori, it would seem likely that many of the environmental predictors would be highly correlated. Figure V.5 shows the linear correlation coefficients among all of the environmental predictors. The highest magnitude off-diagonal correlation is between SST and ω_{500} at -0.21, which is indicative of that fact that there is more ascent over higher SSTs [*Lau et al.*, 1997]. Next both SST and shear, and latitude and CAPE are negatively correlated with coefficients of -0.16 and -0.15, respectively. These results imply that shear increases over cooler SSTs and that CAPE decreases poleward because in the zonal mean, shear increases and CAPE decreases as the tropics transition to the midlatitudes. Shear and ω_{500} are positively correlated at 0.093, which indicates higher shear in subsiding regions. All the other correlation coefficients are below 0.05. Most correlations are very small and while some physically based correlations are evident in the data, there is no reason to believe that any one of the environmental predictors is redundant. To confirm this, component analysis was conducted on the predictors. The analysis failed to successfully reduce the order of the data by more than one component despite the large number of samples. Nonetheless, the predictors do not appear to be linearly dependent on one another. So, we may progress with some confidence in the knowledge that our predictors are mostly independent and well behaved.

The linear regression results are shown in Fig. V.6. Each panel shows a bar plot of the regression coefficients for a different morphological dependent similar to the previous figures.

Figure V.6a shows the regression coefficients for CTH. SST is the leading predictor with shear and AOD approximately half as important as SST. SST is positively correlated with CTH, which indicates higher cloud tops and stronger convection with increasing SST as shown in *Chapter II*. Anvil width correlations are shown in Fig. V.6b with four leading predictors indicated: Shear, SST, AOD, and ω_{500} . For IWP, the leading predictor is ω_{500} followed by AOD and SST. Surprisingly, given the results above, the leading predictor of anvil base temperature appears to be ω_{500} . The number of cores is most strongly correlated to shear strength. And finally, Fig. V.6f shows that base height is most strongly dependent on SST followed by AOD and latitude.

Taken together, the results of these multiple linear regressions imply that a certain subset of the environmental predictors is most influential to cloud morphology. Based on qualitative assessment for Fig. V.6, SST appears to be the most significant predictor followed by ω_{500} . AOD appears frequently in the list above but always lags the leading predictor in magnitude for any individual morphological trend. Shear is also frequently important. What is also impressive is that CAPE is never a leading predictor. Not only is the magnitude of the scaled regression coefficient often small for CAPE, but it also is sometimes 2 orders of magnitude smaller than the leading predictor.

Finally, all of these multiple linear regressions were recomputed with an additional predictor – one that would imply a constant value of the morphological dependent. In all of the cases presented, this became the leading order predictor. This result does not imply that cloud morphology is totally insensitive to the environment. But, it does imply a weak dependence on environment and a strong influence on morphology by the cloud itself. Lending further support to this suggestion, it was found in *Chapter IV* that very strong correlations between sizes of

various components of individual deep convective clouds exist. Although *Sherwood*, [1999] cautions us explicitly against taking such conclusions too far.

4.3 Data Control

In this section, we attempt to ensure that decisions made in appending the environmental data to the cloud objects do not unduly affect the analyzed trends. Toward that end, data are reanalyzed in various ways in order to test some of the conclusions drawn above. It will be shown that the data used above constitutes an appropriate set. Table 1 lists the original (control) and the new (test) data.

An interesting comparison between slightly different AOD datasets was conducted. In general, the highest possible resolution environmental data were used in this study (see §3). However, different resolutions of AOD have been examined. Each cloud object has both a 10 km resolution and 1-degree resolution AOD appended to it. The mean, median, standard deviation, and distribution shapes of these two quantities are remarkably similar. However, individual pairs of these values are often quite different. For example, a randomly chosen cloud object had a 5km AOD of 0.24 and a 1-degree AOD of 0.33. Thus, the precise dependence of the cloud objects on AOD is slightly different. The mean and median distance between the observation center of AOD and the center of the cloud object are similar between the two sets of data, but the standard deviation and top 10% of distances are much greater for the 1-degree data. Thus, with no obvious cloud contamination at 10 km, or at least no more than exists at 1-degree, the 10 km data appears to be more representative of the clear sky AOD local to the cloud.

Gryspeerd et al. [2014b] also note that potentially unphysical conclusions can be drawn from correlating clouds and aerosol due to humidity swelling [*Twohy et al*, 2009], cloud contamination [*Kaufman et al*, 2009], and 3D radiative effects [*Wen et al*, 2007]. However, the

methodology employed here should help to minimize such systematic errors that have been a problem previously. We use well-resolved clouds instead of cloud fraction, and as such, all of our AOD retrievals should be similarly biased in the ways described above. Over a large number of cloud objects, only the systematic biases from swelling, contamination, and radiative effects should be left. Since we then do analyses with *trends* in AOD, not *magnitudes*, the bias is precluded from influencing the conclusions.

The remaining conceptual issue with ω_{500} as an environmental variable is interpreting precisely of what it is a measure. Because of the conditional sampling method used here where a cloud object is a necessary condition for ω_{500} to be measured, understanding how much of the ω_{500} field is due to what is traditionally thought of as ω_{500} , some kind of broad environmental characterization, and how much is due to the presence of cloud updraft is impossible. A reassignment of the data has been conducted in which ω_{500} is defined to occur between 0 to 6 hours prior to the observation of the cloud object. This leaves approximately half of the ω_{500} data points the same as before. The data that was sampled originally between 0 and 3 hours after the cloud object observation is replaced with data occurring 3 to 6 hour prior to the cloud object observation. This shift is due to the 6-hour time resolution of the ECMWF reanalysis data. If cloud object lifetime is relatively short, this new “ $\omega_{500_earlier}$ ” measure will not be contaminated by the cloud-associated vertical motion. Independence from cloud contamination is obviously not a realistic assumption, but this is just an illustrative check of the data quality. The mean arithmetic difference between the original ω_{500} and the new $\omega_{500_earlier}$ indicates slightly more vertical motion in the original ω_{500} . This suggests that ω_{500} is indeed slightly contaminated by convection. Using this newly defined “ $\omega_{500_earlier}$,” all the trends in Fig. V.3 were recalculated. In general, the trends became weaker, as would be expected for data

characterizing physics that are less impactful to convection or data that are less influenced by the convection itself. These new ω_{500_ealier} data were also less influential when run through the multiple linear regressions. It may be concluded from this resampling that the original ω_{500} is potentially influenced by the convection itself, and that if this is the case, then trends attributed to ω_{500} above are actually over estimates.

A conceptually different version of shear was also calculated. $Shear_low$ is calculated as the magnitude of the vector difference between the 1000 hPa-900hPa and 800hPa-700hPa layers. Often times, this low-level shear is assumed to be important for morphology due to its ability to interact with the storm-produced cold pool [Rotunno *et al.*, 1988]. $Shear_low$ was run through the same analysis as the deep layer shear. The trends obtained were similar to those in Fig. V.4, although not as strong, except for the decrease in cloud base height, which was stronger and more linear. The strengthening of the relationship between cloud base height and $shear_low$ could be indicative of a coupling between low level shear and sub-cloud properties as postulated. The multiple linear regression coefficients were mostly slightly weaker. The only noteworthy change in the correlation coefficients was between $shear_low$ and SST which increased to 0.18. Given its cumulative performance, the original shear value is better suited for the analysis than $shear_low$ for the tropical deep convection examined herein.

SST has been re-assessed in terms of its departure from its 20-year (1991-2010) mean (ΔSST) of its geographic location. The mode of the histogram (Fig. V.7) of cloud objects occurs at +1.5K with a long tail toward positive anomalies and a short tail toward negative anomalies with the lowest ΔSST of a cloud object occurring at just -3.6K. In rerunning the multiple linear regression with ΔSST replacing SST, ΔSST proved to be less influential than SST in every case. Only for IWP did it retain much predictive power. Another revealing assessment was also

performed. In this case, trends were examined with respect to Δ SST for a certain climatological-SST bin. For example, the anvil widths for cloud objects with a climatological SST of 300K were regressed as a function of their Δ SST. In these cases, Δ SST was influential. Like the SST value used in §4.2, this second Δ SST casts morphology as a function of an absolute surface temperature – in this case as a departure from a specific value. The real conclusion to be drawn from the investigation of Δ SST is that a pure anomaly in SST does not appear to be particularly influential to cloud morphology, however absolute temperature does.

Finally, shear has been reexamined in another way. In the tropics, the shear vector is primarily oriented in the zonal direction, yet CloudSat samples along a primarily meridional path. So the question becomes to what extent this combination influences the results above. To test this, shear has been reanalyzed, not as the total magnitude (as above), but in terms of its zonal and meridional components. The results of the multiple linear regression run for anvil width with the magnitudes of shear (the operational variable), the zonal shear, and the meridional shear are shown in Fig. V.8a. The first-order result from the figure is that the magnitude of the total shear does appear to be an important predictor of (meridional) morphology. This confirms its relevance to the study. That being said, the other interesting finding is the sensitivity of measured morphology to individual vector directions of shear. For example, the data show a negative sensitivity to the linear component of zonal shear that varies independently of the total shear. Thus, for a given total shear an increase in zonal shear decreases the measured (mostly meridional) anvil width. This is presumably occurring due to a competition for detrainable mass between components of the shear. However, when only the components of shear are used as predictors (Fig. V.8b), both the zonal and meridional components act to increase anvil width. This serves to reconfirm the power of the total shear as the predictor of morphology since both

components are now positive like the total was while indicating sensitivity to each component. Other morphological components run against the components and total shear imply similar conclusions, although often less clearly.

4.4 Potentially Surprising Insensitivities

The two results uncovered that are potentially the most surprising are the almost complete lack of sensitivity to CAPE given that it frequently forms the basis of a number of parameterization schemes [Arakawa, 2004; Yano and Plant, 2012], and that sensitivity to ω_{500} does not overwhelm the statistical signal coming from the other variables given past results [Lau *et al.*, 1997]. These results are discussed next.

The issue that needs to be addressed is why convective morphology exhibits such slight dependence on CAPE. After all, CAPE is used in convective parameterizations, and high sensitivity to CAPE has been demonstrated in mid-latitude clouds [e.g. *Bluestein and Parker*, 1993; *Weisman*, 1993]. There are potentially two primary reasons for this result. The first, reason is that the retrieval and/or calculation of CAPE may be unrepresentative. AIRS data are relatively coarse and subject to contamination in high cloud fraction layers at low levels [Yue *et al.*, 2013]. Potential contamination by low-level clouds is a possible concern here. Consequently, it is possible that the CAPE measurement is often poorly representative of the real environmental CAPE. The second possible reason for CAPE's poor predictive skill is simply that in the tropics, deep convective clouds are insensitive to the precise magnitude of CAPE. This conclusion has been made before [e.g. *Mapes and Houze*, 1992]. The tropical atmosphere over open ocean tends to be characterized by constant, deep, and skinny CAPE [Lucas *et al.*, 1994]. It has also been suggested that convection over the ocean is more prone to entrainment [Lucas *et al.*, 1994], thus diluting the potential influence of CAPE. To date, nothing has been

shown to require any cloud to eliminate all CAPE in its environment; CAPE is simply an upper bound on the amount of latent heat release a cloud can realize. In areas of weak lapse rates, total CAPE may be difficult for any storm to realize. Also, large CAPE values in the tropics would tend to result from anomalously dry upper levels. This condition, though, is mostly anathema to deep convection [Brown and Zhang, 1997]. Finally, the convective cloud itself might be depleting CAPE [Masunaga, 2012].

That ω_{500} is not *the* leading predictor of convective morphology is likely to be especially surprising given past results to the contrary [Lau et al, 1997]. Again there are two potential explanations for this result. The first is that precisely what constitutes the ω_{500} field in the ECMWF reanalysis is somewhat ill defined. In regions conditionally sampled to include deep convection, the field seems to be a convolution of both background environmental vertical velocity and convective vertical velocity. This obscures its role. Second, it may simply be that while ω_{500} is a highly useful quantity in predicting where deep convection will occur, that it is not *the* defining factor of what those clouds will look like. To confirm that cloud occurrence and morphology are different, Fig. V.9 shows the normalized population densities (PDFs) of ω_{500} associated with cloud objects and all ω_{500} across the entire tropics. The PDF of cloud object ω_{500} is consistent with the first-order statistics listed above (§4.1.3), and the tropics-wide ω_{500} PDF exhibits expected behavior: a peak and skewness toward slightly positive values. Where these PDFs differ is at moderately negative values. The ratio of the two PDFs is also shown and exhibits a peak at -0.3 hPa s^{-1} . Therefore, cloud objects do occur more frequently in rising regimes, as would be expected. The implication of this figure is that the cloud object database does not exhibit an unrepresentative dependence on ω_{500} in cloud object occurrence. So, it is consistent with past results and first principles and yet ω_{500} still is not the sole dictate of

morphology. ω_{500} does not provide any inherent mesoscale organization to clouds. Upward ω_{500} is not even a necessary condition for convection. *Mapes and Houze* [1992] also drew this same conclusion previously (in addition to illustrating insensitivity to CAPE).

5. Summary

The sensitivity of mature tropical deep convective clouds to environmental characteristics has been evaluated. Environmental characteristics, such as CAPE, were shown to influence convective morphology only weakly, while others, including aerosol and SST, were shown to influence convection in significant and physically telling ways. The primary mechanisms elucidated through the various analysis methods above appear to include the following:

- Convective invigoration by both aerosol and midlevel rising motion and to a lesser extent, CAPE. Higher AOD was shown to correlate with clouds that were both deeper and wider, and it was suggested that these were manifestations of aerosol induced deep convective invigoration. The aerosol invigoration result also led to the new suggestion that anvil bases might lower in response to more intense updrafts due to microphysical processes. Mid-level rising motion correlated to similar characteristics. It was suggested that this was the result of enhancements to convection from large-scale dynamics. Environments with higher CAPE also exhibited deeper and wider clouds, but the trends were small in comparison to those from aerosol and mid-level motion.
- Storm organization and “shrinking” by troposphere-deep shear. Cloud objects that exist in regions of larger tropospheric-deep shear were generally shorter than those in regions of weak shear. But, they were often wider with more convective cores.

- Significant control of morphology by sea surface temperature. Multiple-linear regression revealed that sea surface temperature was among the important influences to convective morphology. This result strengthens those of a *Chapter III*.

As was deemed appropriate, the sensitivity of results to choices made in defining the environment was tested. It was found that the data used throughout formed a reasonable basis set. The lack of sensitivity to CAPE and only moderate control on morphology by mid-level vertical velocity were discussed.

The goal in performing this analysis was to assess the sensitivity of oceanic, tropical, deep convective cloud morphology to the near-field meteorological environment. While we have made no specific recommendations concerning convective parameterizations, the implication of these results is that cloud morphology probably can be parameterized based on simple diagnostics of the environmental characteristics. Certainly, CAPE is already used extensively and aerosol is beginning to be [e.g. *Abdul-Razzak and Ghan, 2000*]. Any parameterization that seeks to be more inclusive of environmental parameters will be challenged to determine the right set of predictors. But, the results above would suggest that aerosol, mid-level velocity, deep layer shear, and SST would be a useful basis set from which to continue development.

6. Tables

Table V.1: For each environmental variable, a list of the control definition of the data used throughout and a test definition of the data used in §4.3.

	Control Definition	Test Definition
AOD	10 km resolution	1° resolution
ω500	Nearest-in-time	0-6 hr prior
Shear	Troposphere-deep	Low-level
SST	Local	Climatological anomaly

7. Figures

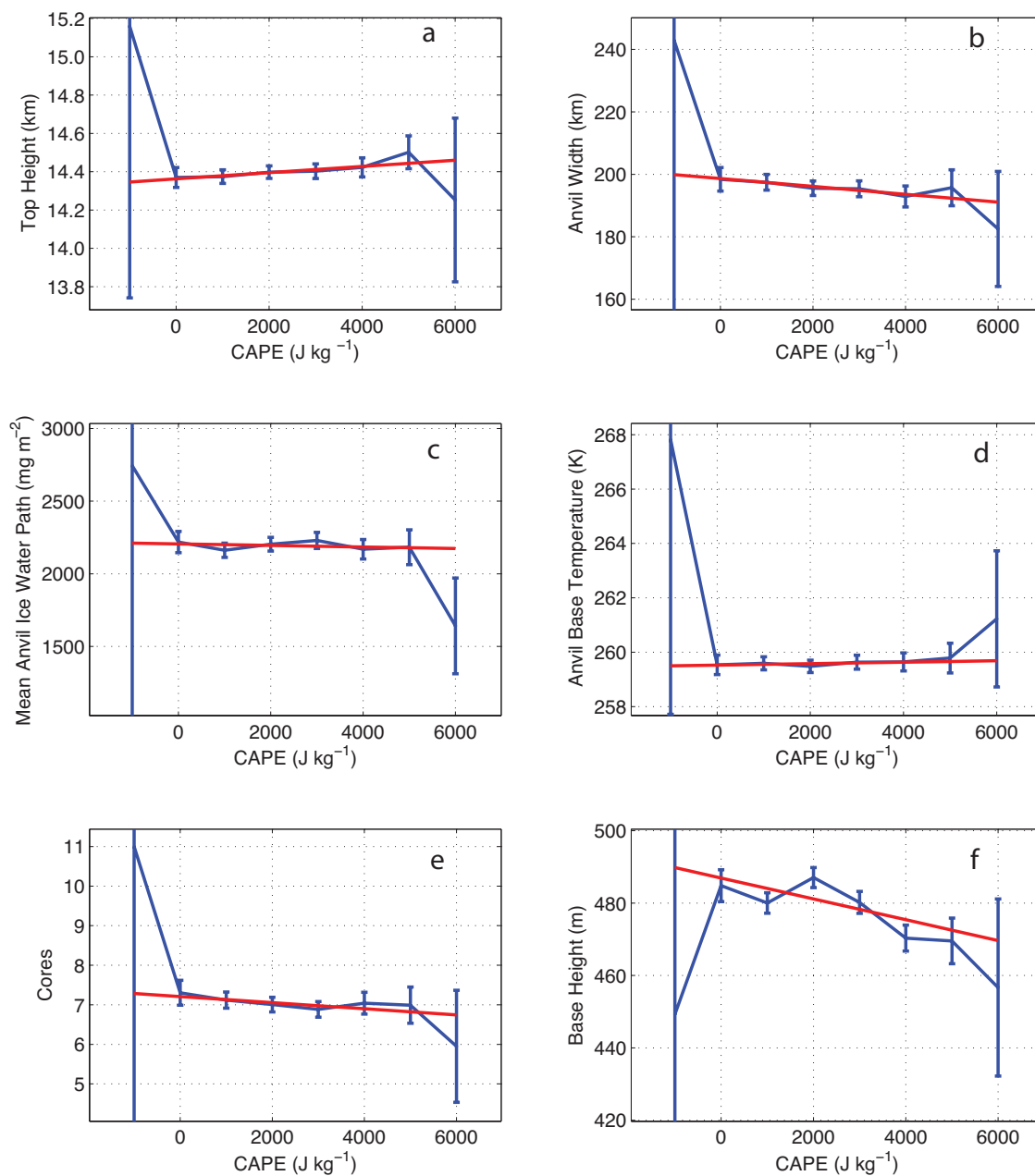


Figure V.1: Each panel shows binned (1000 J kg^{-1} width bins) means as a function of CAPE in blue. 95% confidence intervals for the mean of each bin in shown with the error bar. A linear regression to the unbinned data is shown in red. (a) Cloud top height. (b) Anvil width. (c) Mean anvil ice water path. (d) Anvil base temperature. (e) Number of convective cores. (f) Base height.

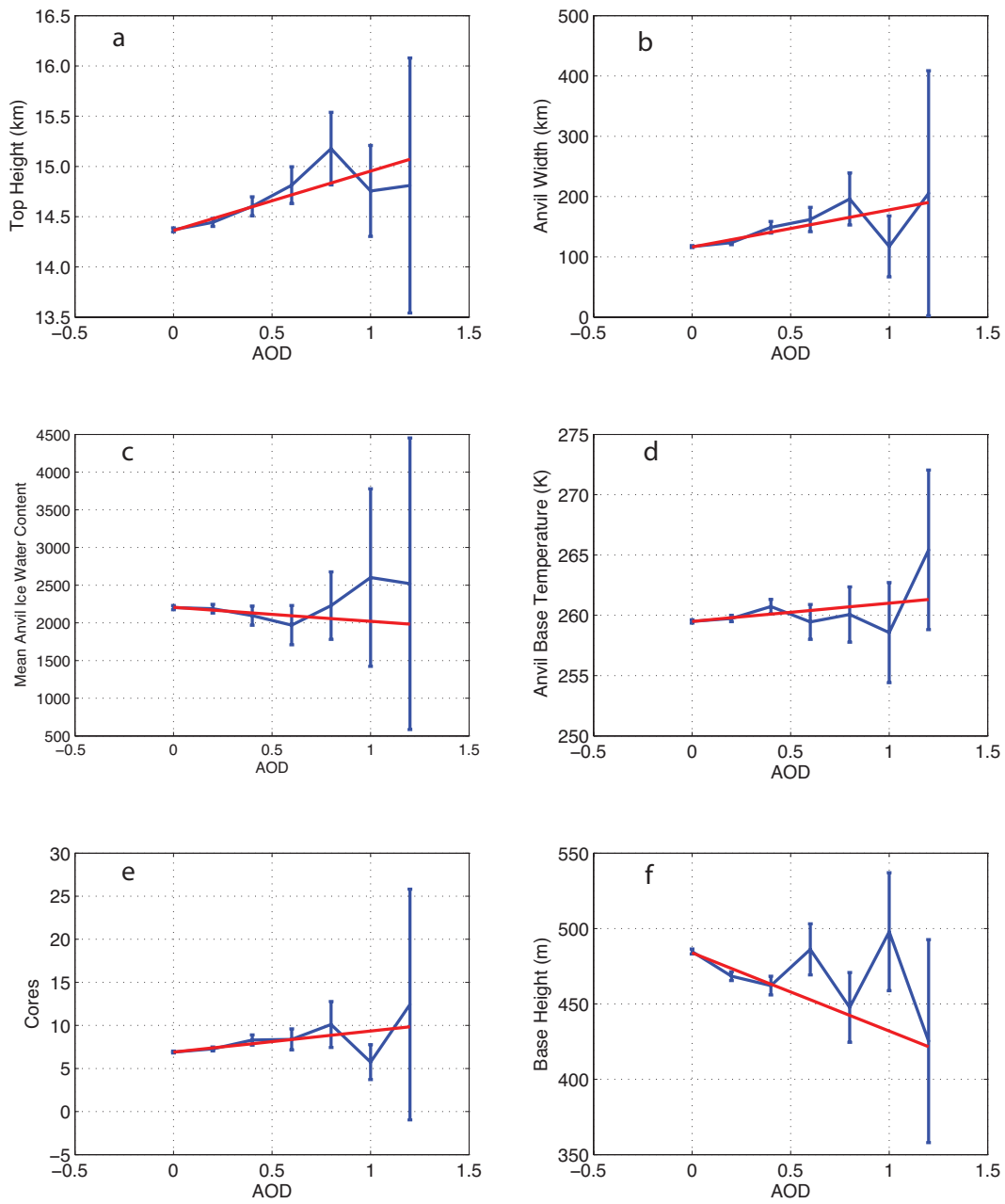


Figure V.2: Same as for Fig. V.1 except for AOD. Bin size is 0.25.

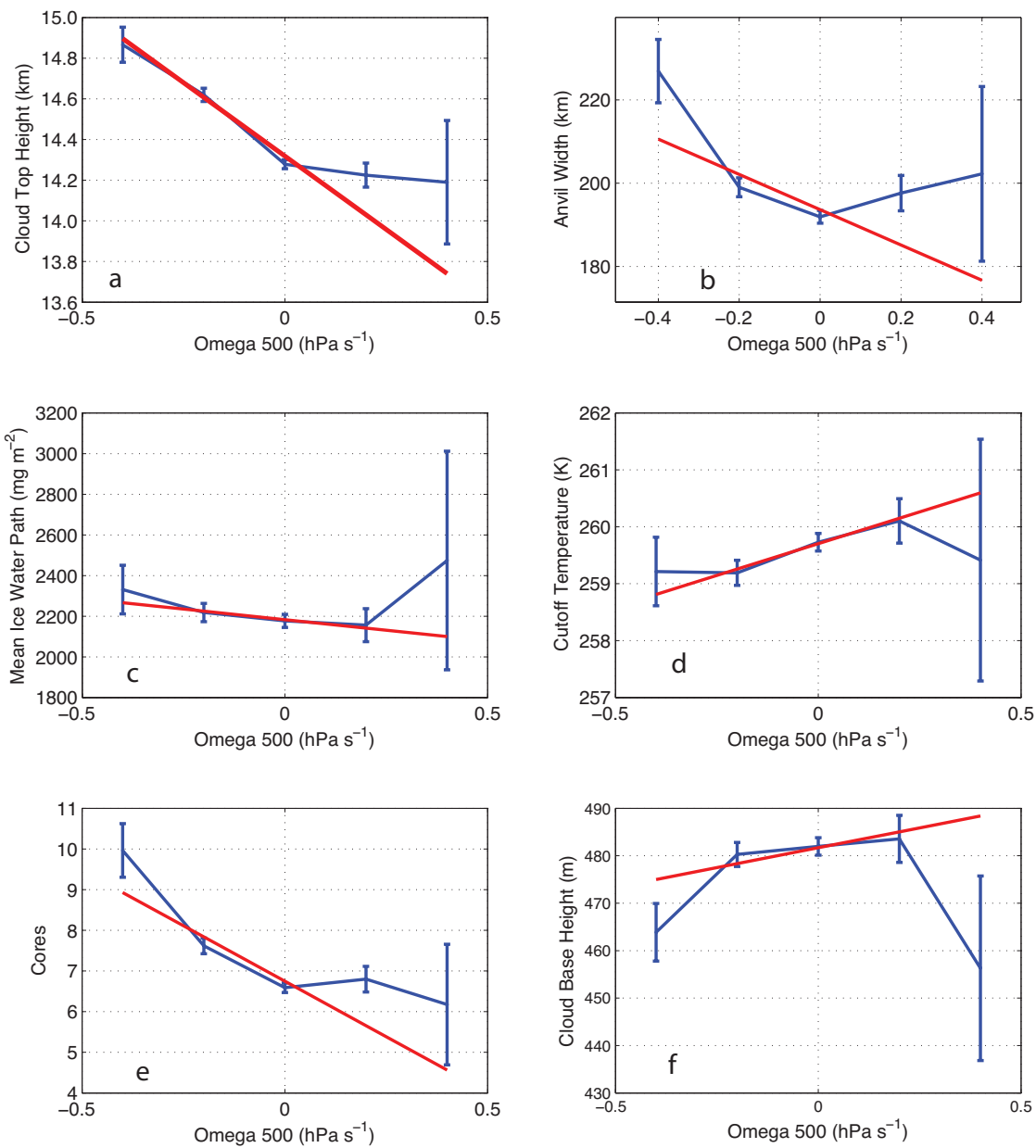


Figure V.3: Same as for Fig. V.1 except for ω_{500} . Bin size is 0.25 hPa s^{-1} .

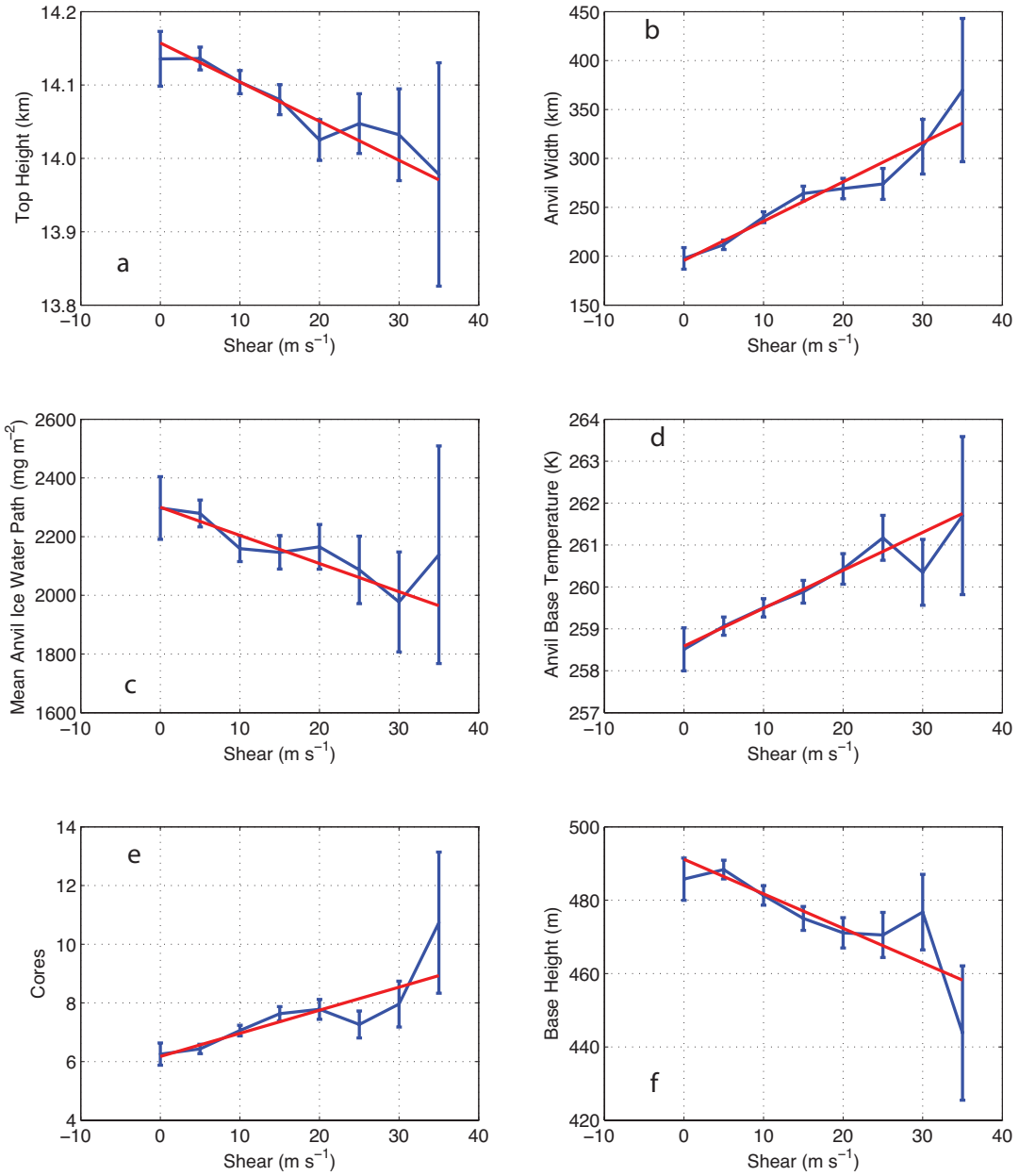


Figure V.4: Same as for Fig. V.1 except for shear. Bin size is 5 m s⁻¹.

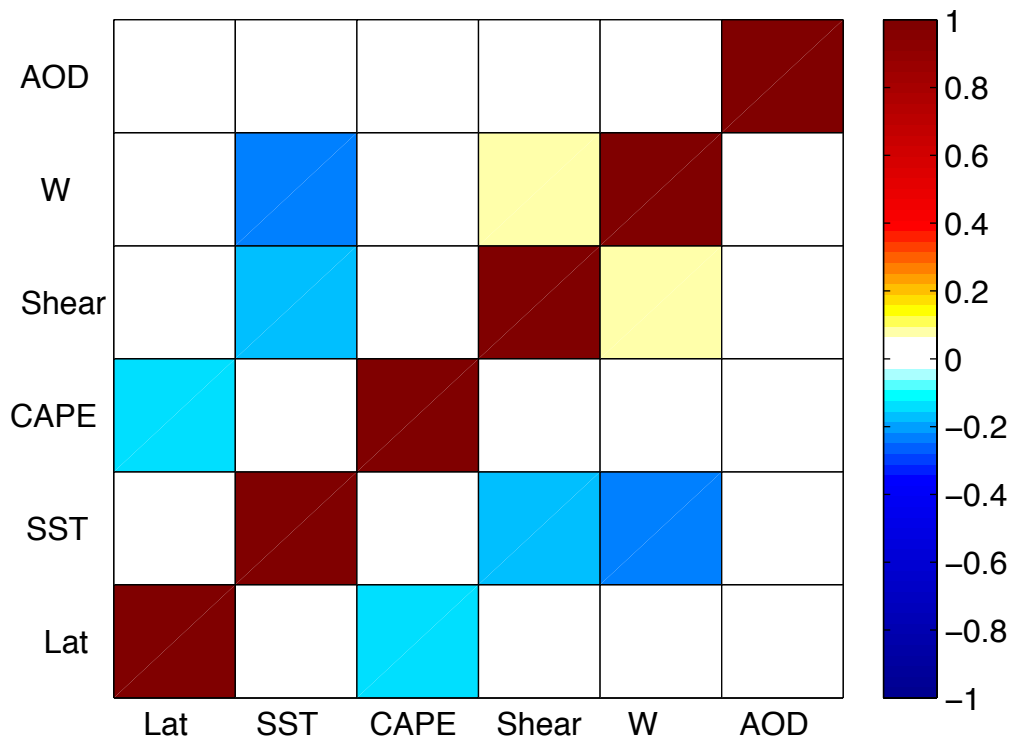


Figure V.5: Correlation coefficients among the environmental predictors used in the multiple linear regressions.

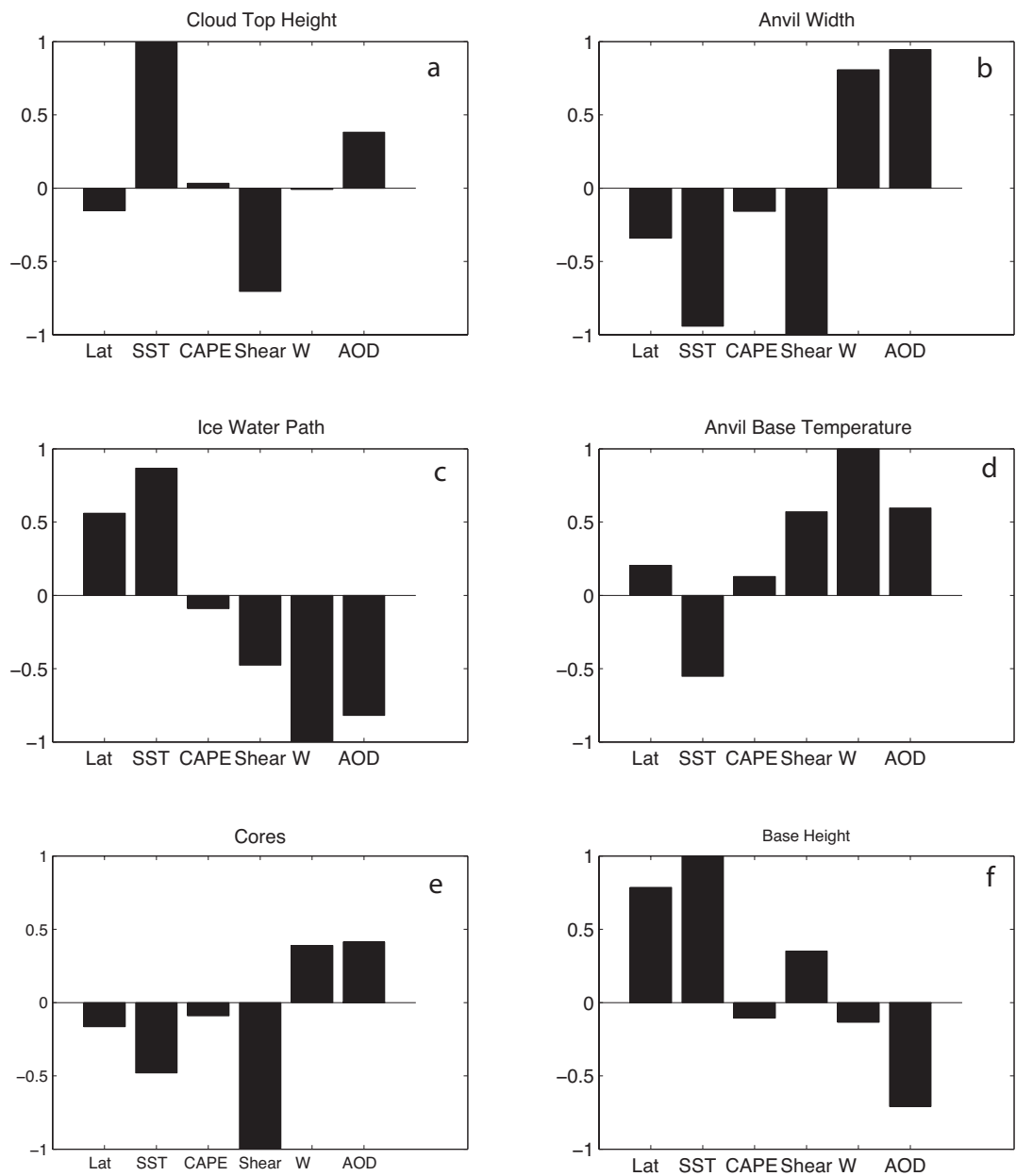


Figure V.6: Normalized multiple linear regression coefficients for each predictor (each bar) for the six morphological dependents (each panel) arranged as in Fig. V.1.

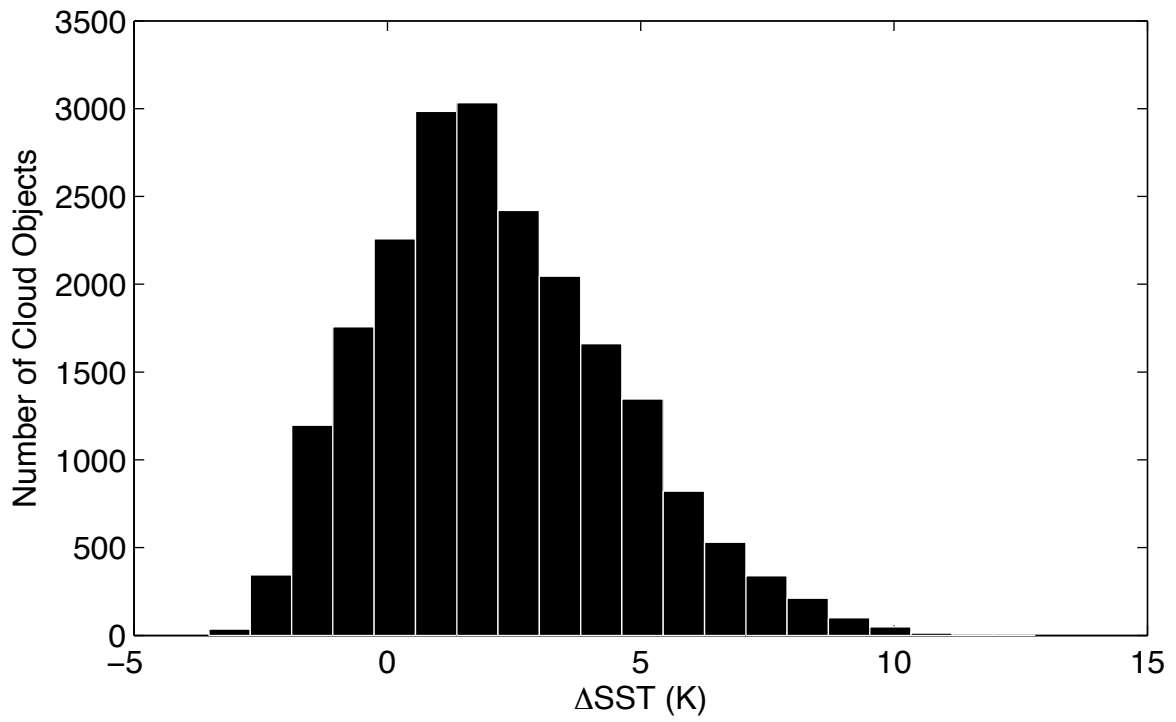


Figure V.7: Histogram of ΔSST .

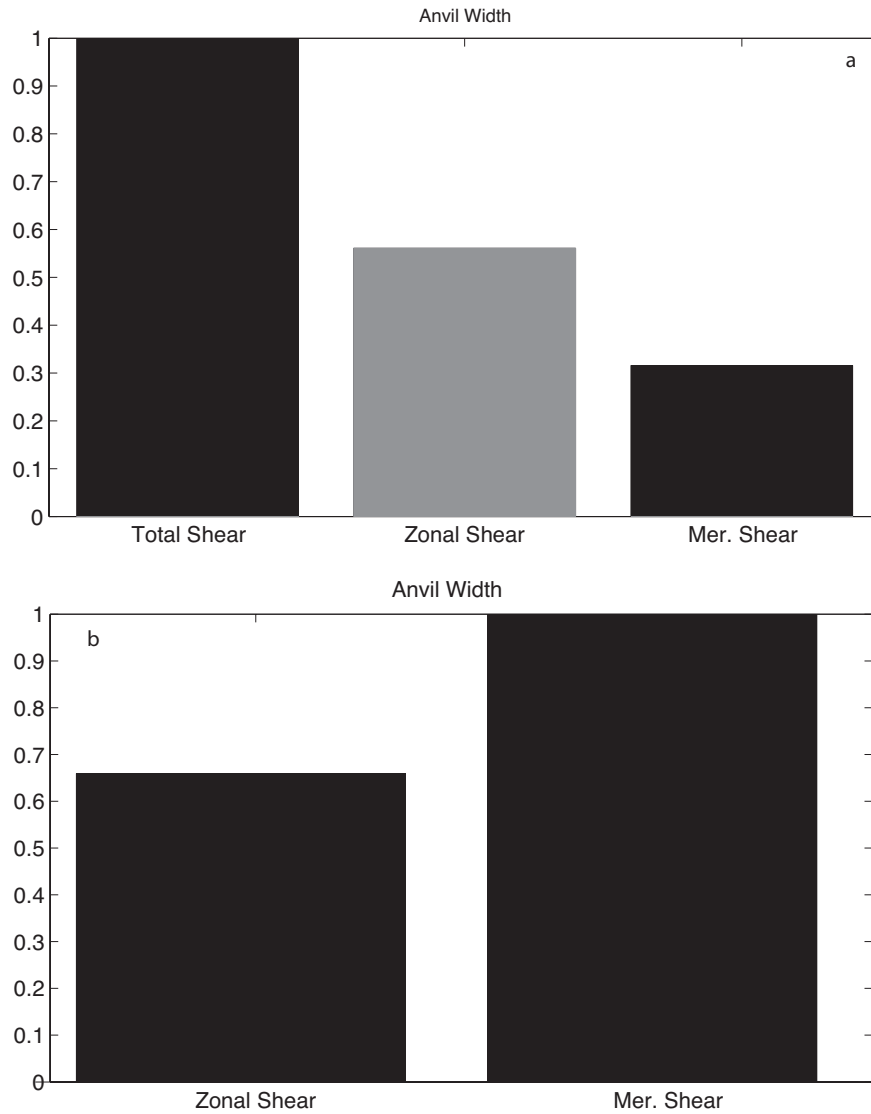


Figure V.8: Linear regression coefficients for the prediction of anvil width using a) total shear, zonal shear, and meridional shear and b) just zonal shear and meridional shear. Gray bars indicate negative values.

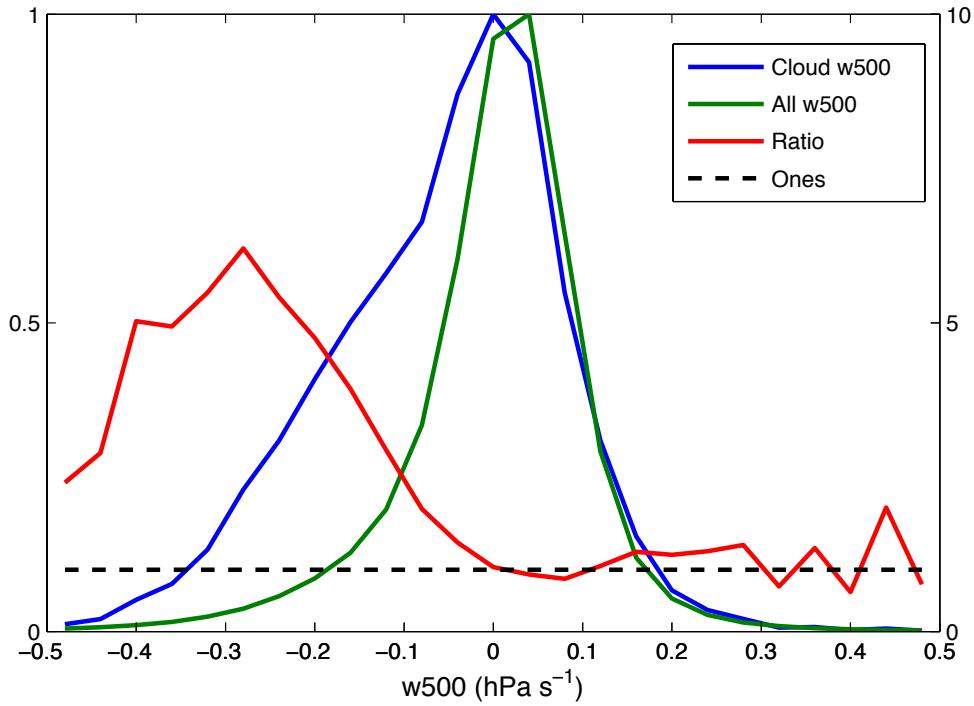


Figure V.9: The blue and green lines illustrate the normalized population density of the cloud object-associated ω_{500} and the all-environment ω_{500} , respectively. These values are read off the left axis. The red line is the ratio of blue to green and is read off the right axis. The black, dashed line illustrates a constant ratio of 1.

CHAPTER VI: CONCLUSIONS AND SUMMARY

Summary

The results contained in previous chapters focused on detailing the physical length scales of convection as observed from CloudSat and on discussing what controls these length scales. Analysis and consideration were limited to oceanic, tropical deep convection because of its importance to the tropical atmosphere. Details of the method of measurement were included first. The method inclusively selects tropical deep convective clouds from along the CloudSat track. Then, the scale invariant nature of the observed clouds was discussed briefly. This result had the crucial implication that because clouds behave in a similar manner at many sizes, scale separation can probably never truly be assumed. It also meant that knowledge can be applied across scales. Next, the climate impacts of clouds were discussed. The focus in that chapter was on examining several previously postulated anvil-climate feedbacks, including the Fixed Anvil Temperature, the Iris, and the Thermostat Hypotheses, within the dataset. Together with the Fixed Lower Anvil Temperature Hypothesis, these responses were all conceptually integrated. It was argued that they all work together. The morphology of these clouds was examined in *Chapter IV*. An “average” tropical cloud was discussed. That section also focused on the relationships between deep convective “pedestals” and “anvils.” It was shown that through simple methods, dynamical conclusions could be drawn. Critically, anvil widths were shown to grow at a slower rate than pedestals. The $2/3^{\text{rd}}$ scaling relationship was introduced. Trends in morphology with base height and core number were shown in order to shed light on convective parameterization assumptions and mesoscale organization, respectively. And, geometric

assessments of CloudSat sampling of deep convective objects were made. Finally, the dependences of many of the previously discussed aspects of convection were examined in light of the near-field thermodynamics and dynamic environment. Links between the local environment and individual clouds were made in order to address the leading question. Aerosol and upward mid-level vertical velocity were shown to result in “invigorated” clouds. Troposphere deep shear acted to widen clouds. The most influential factors affecting deep convective morphology overall were shown to be sea surface temperature, aerosol, and deep-layer shear.

Conclusions

To return to the beginning of this work, in *Chapter II*, it was shown that the total population of deep convective cloud objects seemed to exhibit power-law characteristics. This simple fact was then reasoned to imply that some scale-invariant physical process(es) was allowing clouds to grow to random, potentially self-determined sizes. It is worth considering what the “randomness” (scale invariant, internal control) implied in *Chapter II* means for the successive discussion of deterministic physics. It is possible that cloud volume is unconstrained by anything examined in *Chapters III-V* but that one-dimensional length scales are constrained as was suggested in these chapters. Or, it could be that the calculation of volume is not truly tractable and so results in a random, power-law distribution in some unseen way. Assuming it is the former, then volume is random, but how it is distributed is not. Or it could be that all the factors that dictate length scales operate across time and space to result in a power-law distribution of cloud volume. This is another potential explanation for the results in *Chapter II*. It could even be that if this is the case, that this is the ultimate role of clouds in the tropics -- to organize the environment into its current distribution of meteorological variables. Such a

physical process would obey this causal pathway: clouds are the defining entity of the tropical atmosphere; they conspire to obey a power-law scaling simply by internal processes; the clouds affect the environment in such a way as to result in a particular distribution of shear, SST, CAPE, etc; therefore the meteorological properties of the tropical atmosphere are at the mercy of deep convective clouds. This idea, if true, would be rather jarring to the state of meteorological sciences. Wood and Field [2011] essentially argue in the opposite (normal causal) direction, although with no more specific proof than is presented here, since they predicate their study this way. Testing either idea would be nearly impossible of course. Global models do not currently exhibit the correct distribution of environments so would not be a useful test bed. Observations are always constrained to reality and so would have no experimental control. But, if the author were left to speculate on what may be the most important result of this dissertation, he would be hard pressed to argue against the results in *Chapter II*.

The work presented in this dissertation legitimizes the case for a holistic approach to understanding tropical convection. In *Chapter I*, it was asked what controls the physical length scales of deep convection. It was suggested in *Chapters II-V* that the length scales of individual components of clouds are controlled by internal microphysics, other components of the clouds, the local meteorological environment, and a proxy for climate. Deep clouds do not seem to obey the whims of one simple order parameter, but instead, those of a bevy of influential factors. Many different potentially controlling physics were discussed in order to encircle convection conceptually. From microphysics to macrophysics, clouds depend on physical processes occurring across 12 orders of magnitude in space. This work has attempted to span this space in a very basic way. This dissertation has focused on the use of observational data from a single satellite platform. Yet, snapshot observations cannot be the only approach taken. Mesoscale

modeling is necessary to perform controlled experiments on convection. Until satellite observations improve, cloud modeling will be crucial for understanding the role of microphysics in clouds. Global modeling needs to be a piece of the puzzle too. Balanced global models utilize our best understanding of the myriad of physical processes occurring simultaneously across the entire earth-system and thus link convection in a unique way to other potentially far-field processes. So, there is still much work to be done in order to fully detail the environmental influences on and impacts of clouds and cloud scales.

The chief imitation of the methodology developed is that it does not provide a useful indication of the frequency of objects. The reasons for this are twofold. The first is that the diurnal sampling of CloudSat could bias the frequency of occurrence. Second is that the method willfully pares away questionable data. While it is not obvious how to overcome these limitations, those undertaking future studies building off of the foundational blocks laid here would be well served to consider how to account for cloud number. With a reasonable assessment of cloud number, the full effects (size + frequency) of clouds could be investigated. This would help to place contextually the current assessment of sizes into the broader study of cloud effects. As it stands, though, the analysis of size and the implications of size included above constitute a significant contribution to our understanding of how tropical deep convective clouds behave and why they behave in the way they do.

REFERENCES

Chapter I

- Kummerow, C., W. Barnes, T. Kozu, J. Shiue, and J. Simpson (1998), The Tropical Rainfall Measuring Mission (TRMM) sensor package. *J. Atmos. Oceanic Technol.*, **15**, 809–817.
- Stephens, G. L. et al. (2008), CloudSat mission: Performance and early science after the first year of operation, *J. Geophys. Res.*, **113**, D00A18, doi:10.1029/2008JD009982.

Chapter II

- Arakawa, A., and W. H. Schubert (1974), Interaction of a Cumulus Cloud Ensemble with the Large-Scale Environment, Part I, *J. Atmos. Sci.*, **31**, 674–701.
- Bacmeister, J. T., and G. L. Stephens (2011), Spatial statistics of likely convective clouds in CloudSat data, *J. Geophys. Res.*, **116**(D4), 1–21, doi:10.1029/2010JD014444.
- Bak, P., C. Tang, and K. Wiesenfeld (1987), Self-Organized Criticality: An Explanation of the $1/f$ Noise, *Phys. Rev. Lett.*, **4**, 381–384.
- Behrangi, A., T. Kubar, and B. Lambriksen (2012), Phenomenological Description of Tropical Clouds Using *CloudSat* Cloud Classification. *Mon. Wea. Rev.*, **140**, DOI: 10.1175/MWR-D-11-00247.1
- Bony, S., K.-M. Lau, and Y. C. Sud (1997), Sea Surface Temperature and Large-Scale Circulation Influences on Tropical Greenhouse Effect and Cloud Radiative Forcing, *J. Clim.*, **10**(8), 2055–2077.
- Bony, S., and coauthors (2006), How Well Do We Understand and Evaluate Climate Change Feedback Processes? *J. Climate*, **19**, 3445–3482.
- Cahalan, R. F. and J. H. Joseph (1989), Fractal Statistics of Cloud Fields, *Mon. Wea. Rev.*, **117**, 261–272.
- Cahalan, R. F., and J. B. Snider (1989), Marine stratocumulus structure, *Remote Sensing of Environment*, **28**, 95–107, doi:10.1016/0034-4257(89)90108-9.
- Chae, J. H. and S. C. Sherwood (2010), Insights into Cloud-Top Height and Dynamics from the Seasonal Cycle of Cloud-Top Heights Observed by MISR in the West Pacific. *J. Climate*, **67**, 248–261.
- Chen, S. S., R. a Houze Jr., and B. E. Mapes (1996), Multiscale Variability of Deep Convection in Relation to Large-Scale Circulation in TOGA COATRE, *J. Atmos. Sci.*, **53**(10), 1380–1409.
- Christian, H. J., et al., Global frequency and distribution of lightning as observed from space by the Optical Transient Detector, *J. Geophys. Res.*, **108**, 4005, doi:10.1029/2002JD002347, 2003.
- Clauset, A., C. R. Shalizi, and M. E. J. Newman (2009), Power-Law Distributions in Empirical Data, *SIAM Review*, **51**(4), 661–703, doi:10.1137/070710111.
- Cotton, W. R., R. A. Pielke Sr., R. L. Walko, G. E. Liston, C. J. Tremback, H. Jiang, R. L. McAnelly, J. Y. Harrington, M. E. Nicholls, G. G. Carrio, J. P. McFadden (2003), RAMS 2001: Current status and future directions. *Meteor. Atmos. Phys.*, **82**, 5–29.

- Del Genio, A. D., and W. Kovari (2002), Climatic Properties of Tropical Precipitating Convection under Varying Environmental Conditions. *J. Climate*, **15**, 2597-2615.
- Dias, J., S. N. Tulich, and G. N. Kiladis (2012), An Object-Based Approach to Assessing the Organization of Tropical Convection, *J. Atmos. Sci.*, **69**(8), 2488–2504, doi:10.1175/JAS-D-11-0293.1.
- Grabowski, W. W. (2001), Coupling Cloud Processes with the Large-Scale Dynamics Using the Cloud-Resolving Convection Parameterization (CRCP), *J. Atmos. Sci.*, **58**(9), 978–997, doi:10.1175/1520-0469(2001)058<0978:CCPWTL>2.0.CO;2.
- Harrop, B. E., and D. L. Hartmann (2012), Testing the Role of Radiation in Determining Tropical Cloud-Top Temperature. *J. Climate*, **25**, 5731-5747.
- Hartmann, D. L. and K. Larson (2002), An important constraint on tropical cloud-climate feedback. *Geophys. Res. Lett.*, **29**, doi: 10.1029/2002GL015835.
- Hartmann, D. L. and M. L. Michelsen (1993), Large-Scale Effects on the Regulation of Tropical Sea Surface Temperature. *J. Climate*, **6**, 2049-2062.
- Haynes, J. M., T. S. L'Ecuyer, G. L. Stephens, S. D. Miller, C. Mitrescu, N. B. Wood, and S. Tanelli (2009), Rainfall retrieval over the ocean with spaceborne W-band radar, *J. Geophys. Res.*, **114**, D00A22, doi:10.1029/2008JD009973.
- Haynes, J. M., and G. L. Stephens (2007), Tropical oceanic cloudiness and the incidence of precipitation: Early results from CloudSat, *Geophys. Res. Lett.*, **34**, L09811, doi:10.1029/2007GL029335.
- Houze, R. A., Jr., 1993: *Cloud Dynamics*. Academic Press, 573 pp.
- Igel, M. R., S. C. van den Heever, G. L. Stephens, and D. J. Posselt (2014), Convective-Scale Responses of a Large-Domain, Modeled Tropical Environment to Surface Warming. *Quart. J. Roy. Met. Soc.*, Doi:10.1002/qj.2230.
- Igel, M. R. (2011), A Tropical Radiation and Cloud System Feedback Modulated by Sea Surface Temperatures. Masters Thesis, Colorado State University, 79pp.
- Klein, S. A., B. J. Soden, and N.-G. Lau (1999), Remote Sea Surface Temperature Variations during ENSO: Evidence for a Tropical Atmospheric Bridge, *J. Climate*, **12**, 917-932.
- Kuang, Z. and D. L. Hartmann (2007), Testing the Fixed Anvil Temperature Hypothesis in a Cloud-Resolving Model. *J. Climate*, **20**, 2051-2057.
- Lau, K.-M., H.-T. Wu, and S. Bony (1997), The Role of Large-Scale Atmospheric Circulation in the Relationship Between Tropical Convection and Sea Surface Temperature. *J. Climate*, **10**, 381-392.
- Lebsock, M. D., C. Kummerow, and G. L. Stephens (2010), An Observed Tropical Oceanic Radiative-Convective Cloud Feedback. *J. Climate*, **23**, 2065-2078.
- L'Ecuyer, T. S., N. B. Wood, T. Haladay, G. L. Stephens, and P. W. Stackhouse Jr. (2008), Impact of clouds on atmospheric heating based on the R04 CloudSat fluxes and heating rates data set, *J. Geophys. Res.*, **113**, D00A15, doi:10.1029/2008JD009951.
- Liao, X., W. B. Rossow, and D. Rind (1995), Comparison between SAGE II and ISCCP high-level clouds 1. Global and zonal mean cloud amounts, *J. Geophys. Res.*, **100**, 1121–1135.
- Li, Y., P. Yang, G. R. North, and A. Dessler (2012), Test of the Fixed Anvil Temperature Hypothesis. *J. Atmos. Sci.*, **69**, 2317-2328.
- Lin, B., T. Wong, B. A. Wielicki, and Y. Hu (2004), Examination of the Decadal Tropical ERBS Nonscanner Radiation Data for the Iris Hypothesis. *J. Climate*. **17**, 1239-1246.
- Lindzen, R. S., M.-D. Chou, and A. Y. Hou (2001), Does the Earth Have an Adaptive Infrared Iris? *Bull. Amer. Meteor. Soc.*, **82**, 417-432.

- Liou, K.-N. (1996), Influence of cirrus clouds on weather and climate processes: A global perspective. *Mon. Weather Rev.*, **114**, 1167-1199.
- LeMone, M. A., and E. J. Zipser (1980), Cumulonimbus Vertical Velocity Events in GATE. Part I: Diameter, Intensity and Mass Flux, *J. Atmos. Sci.*, **37**, 2444–2457.
- Lloyd, J., E. Guilyardi, and H. Weller (2012), The Role of Atmosphere Feedbacks Duing ENSO in the CMIP3 Models. Part III: The Shortwave Flux Feedback. *J. Climate*, **25**, 4275-4293.
- Lorenz, R (2011), On the statistical distribution of dust devil diameters, *Icarus*, **215**, 381-390.
- Lovejoy, S. (1982), Area-Perimeter Relation for Rain and Cloud Areas, *Science*, **216**(4542), 185–187.
- Luo, Z., G. Y. Liu, and G. L. Stephens (2008), CloudSat adding new insight into tropical penetrating convection, *Geophys. Res. Lett.*, **35**, L19819, doi:10.1029/2008GL035330.
- Luo, Z., G. Y. Liu, G. L. Stephens, and R. H. Johnson (2009), Terminal versus transient cumulus congestus: A CloudSat perspective, *Geophys. Res. Lett.*, **36**, L05808, doi:10.1029/2008GL036927.
- Mace, G. (2006), Level2 GEOPROF Product Process Description and Interface Control Document Algorithm version 5.3. CIRA Tech. Rep. 5.3, 42 pp., Colo. State Univ., Fort Collins.
- Machado, L. A. T., and W. B. Rossow (1993), Structural Characteristics and Radiative Properties of Tropical Cloud Clusters, *Mon. Wea. Rev.*, **121**, 3234–3260.
- Manabe, S., and R. F. Strickler (1964), Thermal Equilibrium of the Atmosphere with a Convective Adjustment, *J. Atmos. Sci.*, **21**, 361–385.
- Mapes, B., S. Tulich, J. Lin, and P. Zuidema (2006), The mesoscale convection life cycle: Building block or prototype for large-scale tropical waves?, *Dyn. Atmos. Oceans*, **42**(1-4), 3–29, doi:10.1016/j.dynatmoce.2006.03.003.
- Meehl, G. A., and Coauthors (2007), Global climate projections. *Climate Change 2007: The Physical Scientific Basis*, S. Solomon *et al.*, Eds., Cambridge University Press, 747–845.
- Mitchell, T. P. and J. M. Wallace (1992), The Annual Cycle in Equatorial Convection and Sea Surface Temperature. *J. Climate*, **5**, 1140-1156.
- Neggers, R. A. J., H. J. J. Jonker, and A. P. Siebesma (2003), Size Statistics of Cumulus Cloud Populations in Large-Eddy Simulations, *J. Atmos. Sci.*, **60**, 1060–1074.
- Nesbitt, S. W., E. J. Zipser, and D. J. Cecil (2000), A Census of Precipitation Features in the Tropics Using TRMM: Radar, Ice Scattering, and Lightning Observations, *J. Climate*, **13**, 4087–4106.
- O'Brien, T. A., F. Li, W. D. Collins, S. A. Rauscher, T. D. Ringler, M. Taylor, S. M. Hagos, and L. R. Leung (2013), Observed Scaling in Clouds and Precipitation and Scale Incognizance in Regional to Global Atmospheric Models, *J. Climate*, **26**, DOI: 10.1175/JCLI-D-13-00005.1.
- Partain, P. (2007), CloudSat ECMWF-AUX Auxiliary Data Process Description and Interface Control Document, CIRA Tech. Rep. 5.2, 10 pp., Colo. State Univ., Fort Collins.
- Peterson, W. A. and S. A. Rutledge (2001), Regional Variability in Tropical Convection: Observations from TRMM, *J. Climate*, **14**, 3566-3586.
- Polonsky, I. N., Labonnote, L. C., Cooper, S. (2008), Level 2 Cloud Optical Depth Product Process Description and Interface Control Document, Version 5.0. CloudSat Project, CIRA, Colorado State University, Fort Collins, 21 pp.

- Posselt, D. J., S. C. van den Heever, and G. L. Stephens (2008), Trimodal cloudiness and tropical stable layers in simulations of radiative convective equilibrium, *Geophys. Res. Lett.*, **35**(8), L08802, doi:10.1029/2007GL033029.
- Posselt, D. J., S. Van Den Heever, G. Stephens, and M. R. Igel (2012), Changes in the Interaction between Tropical Convection, Radiation, and the Large-Scale Circulation in a Warming Environment, *J. Climate*, **25**(2), 557–571.
- Probst, P., R. Rizzi, E. Tosi, V. Lucarini, and T. Maestri (2012), Total cloud cover from satellite observations and climate models, *Atmos. Res.*, **107**, 161–170, doi:10.1016/j.atmosres.2012.01.005.
- Ramanathan, V., and W. Collins (1991), Thermodynamic regulation of ocean warming by cirrus clouds deduced from observations of the 1987 El Nino. *Nature*, **351**, 27-32.
- Randall, D., M. Khairoutdinov, A. Arakawa, and W. Grabowski (2003), Breaking the Cloud Parameterization Deadlock, *Bull. American Meteor. Soc.*, **84**(11), 1547–1564, doi:10.1175/BAMS-84-11-1547.
- Riley, E. M., B. E. Mapes, and S. N. Tulich (2011), Clouds Associated with the Madden-Julian Oscillation: A New Perspective from CloudSat, *J. Atmos. Sci.*, **68**, doi: 10.1175/JAS-D-11-030.1
- Riley, E. M. and B. E. Mapes (2009), Unexpected peak near -15C in CloudSat echo top climatology, *Geophys. Res. Lett.*, **36**, L09819, doi:10.1029/2009GL037558.
- Romps, D. M. and Z. Kuang (2010), Nature versus Nurture in Shallow Convection, *J. Atmos. Sci.*, **67**, 1655-1666.
- Sabin, T. P., C. A. Babu, and P. V. Joseph (2013), SST-convection relation over tropical oceans, *Intern. Journ. Climatology*, **33**(6), 1424–1435, doi:10.1002/joc.3522.
- Saleeby, S. M., S.C. van den Heever (2013), Developments in the CSU-RAMS Aerosol Model: Emissions, Nucleation, Regeneration, Deposition, and Radiation. Accepted to *J. Appl. Meteor. Climatol.*
- Sassen, K., Z. Wang, and D. Liu (2009), Cirrus clouds and deep convection in the tropics: Insights from CALIPSO and CloudSat, *J. Geophys. Res.*, **114**, 1–11, doi:10.1029/2009JD011916.
- Sassen, K., and Z. Wang (2008), Classifying clouds around the globe with the CloudSat radar: 1-year of results. *Geophys. Res. Lett.*, **35**, L04805, doi:10.1029/2007GL032591.
- Sellers, S., P. Nguyen, W. Chu, X. Gao, K.-L. Hsu, and S. Sorooshian (2013), Computational Earth Science: Big Data Transformed Into Insight, *Eos*, **94**, 277-278.
- Singh, M. S., and P. A. O’Gorman (2013), Upward Shift Of The Atmospheric General Circulation Under Global Warming: Theory And Simulations. *J. Climate*, **25**, DOI: 10.1175/JCLI-D-11-00699.1
- Stephens, G. L. et al. (2002), The Cloudsat Mission and the A-Train, *Bull. American Meteor. Soc.*, **83**(12), 1771–1790, doi:10.1175/BAMS-83-12-1771.
- Stephens, G. L. et al. (2008), CloudSat mission: Performance and early science after the first year of operation, *J. Geophys. Res.*, **113**, D00A18, doi:10.1029/2008JD009982.
- Stephens, G. L. (2005), Cloud Feedbacks in the Climate System: A Critical Review. *J. Climate*, **18**, 237-273.
- Stevens, B. (2005), Atmospheric Moist Convection, *Ann. Rev. Earth Planet. Sci.*, **33**, 605–643, doi:10.1146/annurev.earth.33.092203.122658.
- Stubenrauch, C. J., A. Chédin, G. Rädcl, N. A. Scott, and S. Serrar (2006), Cloud Properties and Their Seasonal and Diurnal Variability from TOVS Path-B.

- Su, H., C. S. Bretherton, and S. S. Chen (2000), Self-Aggregation and Large-Scale Control of Tropical Deep Convection: A Modeling Study, *J. Atmos. Sci.*, **57**, 1797-1816.
- Wang, Z., and K. Sassen (2007), Level 2 cloud scenario classification product process description and interface control document, CIRA Tech. Rep. 5.0, 50 pp., Colo. State Univ., Fort Collins.
- Wood, N. (2008), Level 2 Radar-Visible Optical Depth Cloud Water Content Process Description Document, Version 5.1, CloudSat Project, CIRA, Colorado State University, Fort Collins, 26 pp.
- Wood, R. (2012), Stratocumulus Clouds, *Mon. Wea. Rev.*, **140**, 2373–2423, doi:10.1175/MWR-D-11-00121.1.
- Wood, R., and P. R. Field (2011), The distribution of cloud horizontal sizes, *J. Climate*, **24**(18), 4800–4816, doi:10.1175/2011JCLI4056.1.
- Xu, K.-M., T. Wong, B. a Wielicki, L. Parker, and Z. A. Eitzen (2005), Statistical Analyses of Satellite Cloud Object Data from CERES . Part I : Methodology and Preliminary Results of the 1998 El Niño / 2000 La Niña, *J. Climate*, **18**, 2497–2514.
- Yano, J.-I., and R. S. Plant (2012), Convective quasi-equilibrium, *Rev. Geophys.*, **50**, RG4004, doi:10.1029/2011RG000378. 1.
- Young, A. H., J. J. Bates, and J. A. Curry (2013), Application of cloud vertical structure from CloudSat to investigate MODIS-derived cloud properties of cirriform, anvil, and deep convective clouds, *J. Geophys. Res. Atmos.*, **118**, 4689-4699, doi:10.1002/jgrd.50306.
- Yuan, J. and R. A. Houze (2010), Global Variability of Mesoscale Convective System Anvil Structure from A-Train Satellite Data. *J. Climate*, **23**, 5864-5888.
- Yuan, T. (2011), Cloud macroscopic organization: order emerging from randomness, *Atmos. Chem. Phys.*, **11**, 7483-7490.
- Yuter, S. E., R. a Houze Jr., E. A. Smith, T. T. Wilheit, and E. Zipser (2005), Physical Characterization of Tropical Oceanic Convection Observed in KWAJEX, *J. App. Meteor.*, **44**, 385–415.
- Zelinka, M. D., and D. L. Hartmann (2010), Why is the longwave cloud feedback positive? *J. Geophys. Res.*, **115**, doi:10.1029/2010JD013817.

Chapter III

- Behrangi, A., T. Kubar, and B. Lambrigtsen (2012), Phenomenological Description of Tropical Clouds Using *CloudSat* Cloud Classification. *Mon. Wea. Rev.*, **140**, DOI: 10.1175/MWR-D-11-00247.1
- Benedetti, A., G. L. Stephens, and J. M. Haynes (2003), Ice cloud microphysics retrievals from millimeter radar and visible optical depth using an estimation theory approach. *J. Geophys. Res.*, **108**, 4335, doi:10.1029/2002JD002693.
- Bony, S., and coauthors (2006), How Well Do We Understand and Evaluate Climate Change Feedback Processes? *J. Climate*, **19**, 3445-3482.
- Chae, J. H. and S. C. Sherwood (2010), Insights into Cloud-Top Height and Dynamics from the Seasonal Cycle of Cloud-Top Heights Observed by MISR in the West Pacific. *J. Climate*, **67**, 248-261.
- Del Genio, A. D., and W. Kovari (2002), Climatic Properties of Tropical Precipitating Convection under Varying Environmental Conditions. *J. Climate*. **15**, 2597-2615.

- Harrop, B. E., and D. L. Hartmann (2012), Testing the Role of Radiation in Determining Tropical Cloud-Top Temperature. *J. Climate*, **25**, 5731-5747.
- Hartmann, D. L. and K. Larson (2002), An important constraint on tropical cloud-climate feedback. *Geophys. Res. Lett.*, **29**, doi: 10.1029/2002GL015835.
- Hartmann, D. L. and M. L. Michelsen (1993), Large-Scale Effects on the Regulation of Tropical Sea Surface Temperature. *J. Climate*, **6**, 2049-2062.
- Haynes, J. M., T. S. L'Ecuyer, G. L. Stephens, S. D. Miller, C. Mitrescu, N. B. Wood, and S. Tanelli (2009), Rainfall retrieval over the ocean with spaceborne W-band radar, *J. Geophys. Res.*, **114**, D00A22, doi:10.1029/2008JD009973.
- Igel, M. R., S. C. van den Heever, G. L. Stephens, and D. J. Posselt (2014), Convective-Scale Responses of a Large-Domain, Modeled Tropical Environment to Surface Warming. *Quart. J. Roy. Met. Soc.*, Doi:10.1002/qj.2230.
- Igel, M. R. (2011), A Tropical Radiation and Cloud System Feedback Modulated by Sea Surface Temperatures. Masters Thesis, Colorado State University, 79pp.
- Kuang, Z. and D. L. Hartmann (2007), Testing the Fixed Anvil Temperature Hypothesis in a Cloud-Resolving Model. *J. Climate*, **20**, 2051-2057.
- Lau, K.-M., H.-T. Wu, and S. Bony (1996), The Role of Large-Scale Atmospheric Circulation in the Relationship Between Tropical Convection and Sea Surface Temperature. *J. Climate*, **10**, 381-392.
- Lebsock, M. D., C. Kummerow, and G. L. Stephens (2010), An Observed Tropical Oceanic Radiative-Convective Cloud Feedback. *J. Climate*, **23**, 2065-2078.
- Li, Y., P. Yang, G. R. North, and A. Dessler (2012), Test of the Fixed Anvil Temperature Hypothesis. *J. Atmos. Sci.*, **69**, 2317-2328.
- Lin, B., T. Wong, B. Wielicki, and Y. Hu (2004), Examination of the Decadal Tropical ERBS Nonscanner Radiation Data for the Iris Hypothesis. *J. Climate*, **17**, 1239-1246.
- Lindzen, R. S., M.-D. Chou, and A. Y. Hou (2001), Does the Earth Have an Adaptive Iris? *Bull. Amer. Meteor. Soc.*, **82**, 417-432.
- Liou, K.-N. (1996), Influence of cirrus clouds on weather and climate processes: A global perspective. *Mon. Weather Rev.*, **114**, 1167-1199.
- Lloyd, J., E. Guilyardi, and H. Weller (2012), The Role of Atmosphere Feedbacks During ENSO in the CMIP3 Models. Part III: The Shortwave Flux Feedback. *J. Climate*, **25**, 4275-4293.
- Manabe, S., and R. F. Strickler (1964), Thermal equilibrium of the atmosphere with a convective adjustment. *J. Atmos. Sci.*, **21**, 361-385.
- Meehl, G. A., and Coauthors (2007), Global climate projections. *Climate Change 2007: The Physical Scientific Basis*, S. Solomon et al., Eds., Cambridge University Press, 747-845.
- Polonsky, I. N., L. C. Labonnote, S. Cooper (2008), Level 2 Cloud Optical Depth Product Process Description and Interface Control Document, Version 5.0. CloudSat Project, CIIRA, Colorado State University, Fort Collins, 21 pp.
- Posselt, D. J., S. C. van den Heever, and G. L. Stephens (2008), Trimodal cloudiness and tropical stable layers in simulations of radiative convective equilibrium, *Geophys. Res. Lett.*, **35**, L08802, doi:10.1029/2007GL033029.
- Ramanathan, V., and W. Collins (1991), Thermodynamic regulation of ocean warming by cirrus clouds deduced from observations of the 1987 El Niño. *Nature*, **351**, 27-32.

- Randall, D., M. Khairoutdinov, A. Arakawa, and W. Grabowski (2003), Breaking the Cloud Parameterization Deadlock, *Bull. Amer. Meteor. Soc.*, **84**, 1547–1564, doi:10.1175/BAMS-84-11-1547.
- Singh, M. S., and P. A. O’Gorman (2013), Upward Shift Of The Atmospheric General Circulation Under Global Warming: Theory And Simulations. *J. Climate*, **25**, DOI: 10.1175/JCLI-D-11-00699.1
- Stephens, G. L. (2005), Cloud Feedbacks in the Climate System: A Critical Review. *J. Climate*, **18**, 237-273.
- Stevens, B. (2005), Atmospheric Moist Convection, *Ann. Rev. Earth Planet. Sci.*, **33**, 605–643, doi:10.1146/annurev.earth.33.092203.122658.
- Xu, K.-M., T. Wong, B. A. Wielicki, L. Parker, B. Lin, Z. A. Eitzen, and M. Branson (2007), Statistical analyses of satellite cloud object data from CERES. Part II: Tropical Convective Cloud Objects during 1998 El Nino and Evidence for Supporting the Fixed Anvil Hypothesis. *J. Climate*, **20**, 819–842.
- Zelinka, M. D., and D. L. Hartmann (2010), Why is the longwave cloud feedback positive? *J. Geophys. Res.*, **115**, doi:10.1029/2010JD013817.

Chapter IV

- Arakawa, A. and W. H. Schubert (1974), Interaction of a Cumulus Cloud Ensemble with the Large-Scale Environment, Part I, *J. Atmos. Sci.*, **31**, 674-701.
- Bacmeister, J. T., and G. L. Stephens (2011), Spatial statistics of likely convective clouds in CloudSat data. *J. Geophys. Res.*, **116**, D04104, doi:10.1029/2010JD014444.
- Barnes, H. and R. Houze (2013), The precipitating cloud population of the Madden-Julian Oscillation over the Indian and west Pacific Oceans, *J. Geophys. Res.*, **118**, 6996-7023.
- Cetrone, J, and R. A. Houze (2006), Characteristics of Tropical Convection over Ocean near Kwajalein, *Mon Wea. Rev.*, **134**, 834-853.
- Chen, S. S., R. A. Houze, and B. E. Mapes (1996), Multiscale Variability of Deep Convection in Relation to Large-Scale Circulation in TOGA COARE, *J. Atmos. Sci.*, **53**, 1380-1409.
- Cotton, W. R., G. D. Alexander, R. Hertebstein, R. L. Walko, R. L. McAnelly, and M. Nicholls, (1995), Cloud Venting – a review and some new global annual estimates, *Earth.-Sci. Rev.*, **39**, 169-206.
- Cotton, W. R., and Coauthors (2003), RAMS 2001: Current status and future directions, *Meteor. Atmos. Phys.*, **82**, 5–29.
- Feng, Z., X. Dong, B. Xi, S. A. McFarlane, A. Kennedy, B. Lin, and P. Minnis (2012), Life cycle of midlatitude deep convective systems in a Lagrangian framework, *J. Geophys. Res.*, **117**, D23201, doi:10.1029/2012JD018362.
- Fierro, A. O, E. J. Zipser, M. A. LeMone, J. M. Straka, J. (Malkus) Simpson (2012), Tropical Oceanic Hot Towers: Need They Be Undilute to Transport Energy from the Boundary Layer to the Upper Troposphere Effectively? An Answer Based on Trajectory Analysis of a Simulation of a TOGA COARE Convective System, *J. Atmos. Sci.*, **69**, 195–213.
- Fueglistaler, S., A. E. Dessler, T. J. Dunkerton, I. Folkins, Q. Fu, and P. W. Mote (2009), Tropical tropopause layer, *Rev. Geophys.*, **47**, RG1004, doi:10.1029/2008RG000267.
- Gray, W. M. (1973), Cumulus Convection and Larger Scale Circulations 1. Broadscale and Mesoscale Considerations, *Mon. Wea. Rev.*, **101**, 839-855.
- Gray, W. M. and R. W. Jacobson Jr (1977), Diurnal Variation of Deep Cumulus Convection,

- Mon. Wea. Rev.*, **105**, 1171-1188.
- Heymsfield, G. M., L. Tian, A. J. Heymsfield, L. Li, and S. Guimond (2010), Characteristics of Deep Tropical and Subtropical Convection from Nadir-Viewing High-Altitude Airborne Doppler Radar, *J. Atmos. Sci.*, **67**, DOI: 10.1175/2009JAS3132.1
- Holle, R (1968), Some Aspects of Tropical Oceanic Cloud Populations, *J. App. Met.*, **7**, 173-183.
- Houze, R. A. (1982), Cloud clusters and large-scale vertical motions in the Tropics, *J. Meteor. Soc. Japan*, **60**, 396-410.
- Houze, R. A., Jr. (1993), *Cloud Dynamics*. Academic Press, 573 pp.
- Houze, R. A, Jr (2004), Mesoscale Convective Systems, *Rev. Geophys.*, **42**, RG4003, doi:10.1029/2004RG000150.
- Houze, R. A. and A. K. Betts (1981), Convection in GATE, *Rev. Geophys. Space Phys.*, **19**, 541-576.
- Houze, R. A. and C. Cheng (1977), Radar characteristics of tropical convection observed during GATE: Mean properties and trends over the summer season, *Mon. Wea. Rev.*, **105**, 964-980.
- Igel, M. R. (2011), A Tropical Radiation and Cloud System Feedback Modulated by Sea Surface Temperatures, M.S. thesis, Dept. Atmos. Sci., Colorado State Univ., Fort Collins, Colorado, USA.
- Johnson, R. H., T. M. Rickenbach, S. A Rutledge, P. E. Ciesieki, and W. H. Schubert (1999), Trimodal characteristics of tropical convection, *J. Clim.*, **12**, 2397- 2418.
- Kuang, Z. and D. L. Hartmann, 2007: Testing the Fixed Anvil Temperature Hypothesis in a Cloud-Resolving Model, *J. Climate*, **20**, 2051-2057.
- Leary, C. A. and R. A. Houze (1979), The Structure and Evolution of Convection in a Tropical Cloud Cluster, *J. Atmos. Sci.*, **36**, 437-457.
- Li, W., and C. Schumacher (2011), Thick Anvils as Viewed by the TRMM Precipitation Radar, *J. Climate*, **24**, 1718-1735.
- Liu, C., E. J. Zipser, G. G. Mace, and S. Benson (2008), Implications of the differences between daytime and nighttime CloudSat observations over the tropics, *J. Geophys. Res.*, **113**, D00A04, doi:10.1029/2008JD009783.
- Lindzen, R. S., M.-D. Chou, and A. Y. Hou (2001), Does the Earth Have an Adaptive Iris? *Bull. Amer. Meteor. Soc.*, **82**, 417-432.
- Liu, C., and E. Zipser (2013), Regional variation of morphology of organized convection in the tropics and subtropics, *J. Geophys. Res.*, **118**, 453-466, doi:10.1029/2012JD018409.
- Lopez, R. E. (1976), Radar Characteristics of the Cloud Population of Tropical Disturbances in the Northwest Atlantic. *Mon. Wea. Rev.*, **104**, 268-283.
- Luo, Z., G. Y. Liu, and G. L. Stephens (2008), CloudSat adding new insight into tropical penetrating convection, *Geophys. Res. Lett.*, **35**, L19819, doi:10.1029/2008GL035330.
- Machado, L. A. T. and W. B. Rossow (1993), Structural Characteristics and Radiative Properties of Tropical Cloud Clusters, *Mon. Wea. Rev.*, **121**, 3234-3260.
- Malkus, J. S., and H. Riehl (1964), Cloud Structure and Distributions Over the Tropical Pacific Ocean, *Tellus*, **16**, 275-287.
- Manabe, S. and R. F. Strickler (1964), Thermal equilibrium of the atmosphere with a convective adjustment. *J. Atmos. Sci.*, **21**, 361-385.
- Mapes, B. E. (1997), Equilibrium vs. Activation Control of Large-Scale Variations of Tropical Deep Convection, in *The Physics and Parameterization of Moist Atmospheric Convection*, 321-358, Kluwer Academic Publishers, Boston, MA.

- Mapes, B. E. and R. A. Houze (1993), Cloud Clusters and Superclusters over the Oceanic Warm Pool, *Mon. Wea. Rev.*, **121**, 1398-1415.
- Mapes, B. E. and R. A. Houze (1995), Diabatic Divergence Profiles in Western Pacific Mesoscale Convective Systems, *J. Atmos. Sci.*, **52**, 1807-1828.
- Mapes, B., S. Tulich, J. Lin, and P. Zuidema (2006), The mesoscale convection life cycle: Building block or prototype for large-scale tropical waves? *Dyn. Atmos. Oceans*, **42**, 3–29, doi:10.1016/j.dynatmoce. 2006.03.003.
- Masunaga, H. (2013), A Satellite Study of Tropical Moist Convection and Environmental Variability: Moisture and Thermodynamic Budget Analysis, *J. Atmos. Sci.*, **70**, 2443-2466.
- Masunaga, H., T. S. L'Ecuyer, and C. D. Kummerow (2006), Variability in the Characteristics of Precipitation Systems in the Tropical Pacific. Part I: Spatial Structure, *J. Climate*, **18**, 823-840.
- McGee, C. J. and S. C. van den Heever (2014), Latent Heating and Mixing Due to Entrainment in Tropical Deep Convection, *J. Atmos. Sci.*, doi:10.1175/JAS-D-13- 0140.1, in press.
- Mohr, K. I., J. S. Famiglietti, and E. J. Zipser (1999), The Contribution to Tropical Rainfall with respect to Convective System Type, Size, And Intensity Estimated from the 85-GHz Ice-Scattering Signature, *J. Appl. Meteor.*, **38**, 596-606.
- Mohr, K. I. and E. J. Zipser (1996), Mesoscale Convective Systems Defined by Their 85-GHz Ice Scattering Signature: Size and Intensity Comparison over Tropical Oceans and Continents, *Mon. Wea. Rev.*, **124**, 2417-2437.
- National Academy of Sciences (1971), Plan for US Participation in GARP Atlantic Tropical Experiment. Report of the Ad Hoc Tropical Task Group to the US Committee for the Global Atmospheric Research Program, National Research Council, Washington DC, 25pp.
- Ogura, Y. and H-R. Cho (1974), On the Interaction between the Subcloud and Cloud Layers in Tropical Regions, *J. Atmos. Sci.*, **31**, 1850-1859.
- Pielke, R. A., and Coauthors (1992), A comprehensive meteorological modeling system RAMS, *Meteor. Atmos. Phys.*, **49**, 69–91.
- Rickenbach, T. M. and S. A. Rutledge (1997), Convection in TOGA COARE: Horizontal Scale, Morphology, and Rainfall Production, *J. Atmos. Sci.*, **55**, 2715-2729.
- Riehl, H. and J. S. Malkus (1958), On the Heat Balance in the Equatorial Trough Zone, *Geophysica*, **6**, 503-538.
- Riley, E. M., B. E. Mapes, and S. N. Tulich (2011), Clouds Associated with the Madden-Julian Oscillation: A New Perspective from CloudSat, *J. Atmos. Sci.*, **68**, doi: 10.1175/JAS-D-11-030.1
- Rossow, W. B., A. Mekonnen, C. Peal, and W. Goncalves (2013), Tropical Precipitation Extremes, *J. Climate*, **26**, 1457-1466.
- Saleeby, S.M., and S.C. van den Heever (2013), Developments in the CSU-RAMS Aerosol Model: Emissions, Nucleation, Regeneration, Deposition, and Radiation. In press at *J. Appl. Meteor. Climatol.*
- Schumacher, C., R. A. Houze Jr, and I. Kraucunas (2004), The Tropical Dynamical Response to Latent Heating Estimates Derived from the TRMM Precipitation Radar, *J. Atmos. Sci.*, **61**, 1341-1358.
- Stephens, G. L., et al. (2008), CloudSat mission: Performance and early science after the first year of operation, *J. Geophys. Res.*, **113**, D00A18, doi:10.1029/2008JD009982.
- Storer, R. L. and S. C. van den Heever (2013), Microphysical Processes Evident in Aerosol

- Forcing of Tropical Deep Convective Clouds. *J. Atmos. Sci.*, **70**, 430-446.
- Takahasi, H. and Z. Luo (2012), Where is the level of neutral buoyancy for deep convection?, *Geophysic. Res Lett.*, **39**, L15809, doi:10.1029/2012GL052638.
- Tompkins, A. M. and K. A. Emanuel (2000), The vertical resolution sensitivity of simulated equilibrium temperature and water-vapour profiles, *Q. J. R Meteorol. Soc.*, **126**, 1219-1238.
- Tompkins, A. M. (2001), Organization of Tropical Convection in Low Vertical Wind Shears: The Role of Water Vapor, *J. Atmos. Sci.* **58**, 529-545.
- Waliser, D., et al. (2009), Cloud ice: A climate model challenge with signs and expectations of progress, *J. Geophys. Res.*, **114**, D00A21, doi:10.1029/2008JD010015.
- Walko, R. L., W. R. Cotton, G. Feingold, and B. Stevens (2000), Efficient computation of vapor and heat diffusion between hydrometeors in a numerical model, *Atmos. Res.*, **53**, 171-183.
- Webster, P. J., and R. Lukas (1992), TOGA COARE: The Coupled Ocean–Atmosphere Response Experiment, *Bull. Amer. Meteor. Soc.*, **73**, 1377–1416.
- Wexler, A. (1977), Vapor Pressure Formulation for Ice, *J. Res. Natl. Bur. Stand.*, **81A**, 5-20.
- Wood, R. and P. R. Field (2011), The Distribution of Cloud Horizontal Sizes, *J. Climate*, **24**, 4800-4816.
- Xu, K.-M., T. Wong, B. A. Wielicki, L. Parker, and Z. A. Eitzen (2005) Statistical analyses of satellite cloud object data from CERES. Part I: Methodology and preliminary results of 1998 El Nino/2000 La Nina, *J. Climate*, **18**, 2497–2514.
- Yang, G.-Y. and J. Slingo (2001), The Diurnal Cycle in the Tropics, *Mon. Wea. Rev.*, **129**, 784-801.
- Yuan, J., and R. A. Houze (2013), Deep Convective Systems Observed by A-Tain in the Tropical Indo-Pacific Region Affected by the MJO, *J. Atmos. Sci.*, **70**, 465-486.
- Yuter, S. E., and R. A. Houze (1995), Three-Dimensional Kinematic and Microphysical Evolution of Florida Cumulonimbus. Part II: Distributions of Vertical Velocity, Reflectivity, and Differential Reflectivity, *Mon. Wea. Rev.*, **123**, 1941-1963.
- Yuter, S. E., R. A. Houze, E. A. Smith, T. T. Wilheit, and E. Zipser (2005), Physical characterization of tropical oceanic convection observed in KWAJEX, *J. Appl. Meteor.*, **44**, 385–415.
- Zhang, C., J. Gottschalck, E. D. Maloney, M. W. Moncrieff, F. Vitart, D. E. Waliser, B. Wang, and M. C. Wheeler (2013), Cracking the MJO nut, *Geophys. Res. Lett.*, **40**, 1223–1230, doi:10.1002/grl.50244.
- Zipser, E. J. (1977), Mesoscale and Convective-Scale Downdrafts as Distinct Components of Squall-Line Structure, *Mon. Wea. Rev.*, **105**, 1568-1589.

Chapter V

- Abdul-Razzak, H., and S. Ghan (2000), A parameterization of aerosol activation: 2. Multiple aerosol types, *J. Geophys. Res.*, *105*(D5), 6837–6844.
- Andreae, M. O. (2009), Correlation between cloud condensation nuclei concentration and aerosol optical thickness in remote and polluted regions. *Atmos. Chem. Phys.*, **9**, 543-556.
- Andreae, M., D. Rosenfeld, P. Artaxo, A. Costa, G. Frank, K. Longo, and M. Silva-Dias (2004), Smoking rain clouds over the Amazon. *Science*, **303**, 1337–1342.

- Arakawa, A. (2004), The Cumulus Parameterization Problem : Past , Present , and Future, *J. Clim.*, *17*(13), 2493–2525.
- Aumann, H. H., Chahine, M. T., Gautier, C., Goldberg, M. D., Kalnay, E., McMillan, L. M., Revercomb, H., Rosenkranz, P. W., Smith, W. L., Staelin, D. H., Strow, L. L., and Susskind, J.: AIRS/AMSU/HSB on the Aqua mission: Design, science objectives, data products, and processing systems, *IEEE Trans. Geosci. Remote Sensing*, *41*, 253–264, 2003.
- Barnes, G. M., and K. Sieckman (1984), The environment of fast- and slow-moving tropical mesoscale convective cloud lines. *Mon. Wea. Rev.*, **112**, 1782–1794.
- Bluestein, H. B. and S. S. Parker (1993), Modes of Isolated, Severe Convective Storm Formation Along the Dryline, *Mon. Wea. Rev.*, **121**, 1354-1372.
- Bony, S., K.-M. Lau, and Y. C. Sud (1997), Sea Surface Temperature and Large-Scale Circulation Influences on Tropical Greenhouse Effect and Cloud Radiative Forcing, *J. Clim.*, *10*(8), 2055–2077, doi:10.1175/1520-0442(1997)010<2055:SSTALS>2.0.CO;2.
- Bony, S., J.-L. Dufresne, H. Le Treut, J.-J. Morcrette, and C. Senior (2004), On dynamic and thermodynamic components of cloud changes, *Clim. Dyn.*, *22*(2-3), 71–86, doi:10.1007/s00382-003-0369-6.
- Brown, R. G., and C. D. Zhang (1997), Variability of midtropospheric moisture and its effect on cloud-top height distribution during TOGA COARE, *J. Atmos. Sci.*, *54*(23), 2760–2774.
- Cetrone, J., and R. a. Houze (2006), Characteristics of Tropical Convection over the Ocean near Kwajalein, *Mon. Weather Rev.*, *134*(3), 834–853, doi:10.1175/MWR3075.1.
- Coniglio, M. C., D. J. Stensrud, and L. J. Wicker (2006), Effects of Upper-Level Shear on the Structure and Maintenance of Strong Quasi-Linear Mesoscale Convective Systems, *J. Atmos. Sci.*, *63*, 1231–1252.
- DeMott, C. A., and S. A. Rutledge (1998), The Vertical Structure of TOGA COARE Convection. Part I: Radar Echo Distributions, *J. Atmos. Sci.*, *55*, 2730–2747.
- Demott, C. A., and S. A. Rutledge (1998), The Vertical Structure of TOGA COARE Convection. Part II: Modulating Influences and Implications for Diabatic Heating, *J. Atmos. Sci.*, *55*, 2748–2762.
- Fan, J., T. Yuan, J. M. Comstock, S. Ghan, A. Khain, L. R. Leung, Z. Li, V. J. Martins, and M. Ovchinnikov (2009), Dominant role by vertical wind shear in regulating aerosol effects on deep convective clouds, *J. Geophys. Res.*, *114*(D22), D22206, doi:10.1029/2009JD012352.
- Fan, J., L. R. Leung, D. Rosenfeld, Q. Chen, Z. Li, J. Zhang, and H. Yan (2013), Microphysical effects determine macrophysical response for aerosol impacts on deep convective clouds., *Proc. Natl. Acad. Sci. U. S. A.*, *110*(48), E4581–90, doi:10.1073/pnas.1316830110.
- Del Genio, A. D., and W. Kovari (2002), Climatic Properties of Tropical Precipitating Convection under Varying Environmental Conditions, *J. Clim.*, *15*(18), 2597–2615.
- Gryspeerdt, E., P. Stier, and D. G. Partridge (2014a), Links between satellite retrieved aerosol and precipitation, *Atmos. Chem. Phys. Discuss.*, *14*(5), 6821–6861, doi:10.5194/acpd-14-6821-2014.
- Gryspeerdt, E., P. Stier, and D. G. Partridge (2014b), Satellite observations of cloud regime development: the role of aerosol processes, *Atmos. Chem. Phys.*, *14*(3), 1141–1158, doi:10.5194/acp-14-1141-2014.
- Halverson, J. B., B. S. Ferrier, T. M. Rickenbach, J. Simpson, and W. Tao (1999), An Ensemble of Convective Systems on 11 February 1993 during TOGA COARE: Morphology,

- Rainfall Characteristics, and Anvil Cloud Interactions, *Mon. Weather Rev.*, **127**, 1208–1228.
- Hildebrand, P. H. (1998), Shear-parallel moist convection over the tropical ocean: A case study from the 18 February 1993 TOGA COARE, *Mon. Wea. Rev.*, **126**, 1952–1976.
- Houze Jr., R. a, and C.-P. Cheng (1977), Radar Characteristics of Tropical Convection Observed During GATE: Mean Properties and Trends Over the Summer Season, *Mon. Weather Rev.*, **105**, 964–980.
- Houze, R. A. (2004), Mesoscale convective systems, *Rev. Geophys.*, **42**, 1–43, doi:10.1029/2004RG000150.1.INTRODUCTION.
- Johnson, R. H., S. A. Aves, P. E. Ciesielski, and T. D. Keenan (2005), Organization of oceanic convection during the onset of the 1998 East Asian summer monsoon. *Mon. Wea. Rev.*, **133**, 131–148.
- Johnson, R. H., T. M. Rickenbach, S. A. Rutledge, P. E. Ciesielski, and W. H. Schubert (1999), Trimodal Characteristics of Tropical Convection, *J. Clim.*, **12**, 2397–2418.
- Jones, T. A., and S. A. Christopher (2010), Statistical properties of aerosol-cloud-precipitation interactions in South America, *Atmos. Chem. Phys.*, (2005), 2287–2305.
- Kaufman, Y., Koren, I., Remer, L., Rosenfeld, D., and Rudich, Y.: The effect of smoke, dust, and pollution aerosol on shallow cloud development over the Atlantic Ocean, *P. Natl. Acad. Sci. USA*, **102**, 11207, doi:10.1073/pnas.0505191102, 2005. 6825
- Khain, A., D. Rosenfeld, and A. Pokrovsky (2005), Aerosol impact on the dynamics and microphysics of deep convective clouds. *Quart. J. Roy. Meteor. Soc.*, **131**, 2639–2664.
- Koren, I., L. a. Remer, O. Altaratz, J. V. Martins, and a. Davidi (2010), Aerosol-induced changes of convective cloud anvils produce strong climate warming, *Atmos. Chem. Phys.*, **10**(10), 5001–5010, doi:10.5194/acp-10-5001-2010.
- Koren, I., G. Feingold, and L. A. Remer (2010), The invigoration of deep convective clouds over the Atlantic: Aerosol effect, meteorology, or retrieval artifact? *Atmos. Chem. Phys.*, **10**, 8855–8872, doi:10.5194/acp-10-8855-2010.
- Koren, I., Altaratz, O., Remer, L. A., Feingold, G., Martins, J. V., and Heiblum, R. H.: Aerosol-15 induced intensification of rain from the tropics to the mid-latitudes, *Nat. Geosci.*, **5**, 118, doi:10.1038/ngeo1364, 2012.
- Koren I., J. V. Martins, L. A. Remer, and H. Afargan (2008), Smoke invigoration versus inhibition of clouds over the Amazon. *Science*, **321**, 946–949, doi:10.1126/science.1159185.
- Kumar, V. V., A. Protat, C. Jakob, and P. T. May (2014), On the Atmospheric Regulation of the Growth of Moderate to Deep Cumulonimbus in a Tropical Environment, *J. Atmos. Sci.*, **71**(3), 1105–1120, doi:10.1175/JAS-D-13-0231.1.
- Lau, K.-M., Wu, T.-U., and S. Bony (1997), The Role of Large-Scale Atmospheric Circulation in the Relationship between Tropical Convection and Sea Surface Temperature, *J. Climate*, **10**, 381–392.
- LeMone, M. a., E. J. Zipser, and S. B. Trier (1998), The Role of Environmental Shear and Thermodynamic Conditions in Determining the Structure and Evolution of Mesoscale Convective Systems during TOGA COARE, *J. Atmos. Sci.*, **55**(23), 3493–3518, doi:10.1175/1520-0469(1998)055<3493:TROESA>2.0.CO;2.
- Lindzen, R. S., M. Chou, and A. Y. Hou (2001), Does the Earth Have an Adaptive Infrared Iris ?, *Bull. Am. Meteorol. Soc.*, **82**(3), 417–432.

- Liu, C., and E. J. Zipser (2012), Regional variation of morphology of organized convection in the tropics and subtropics, *J. Geophys. Res.*, *118*(November 2012), 453–466, doi:10.1029/2012JD018409.
- Lucas, C., E. J. Zipser, and M. a. LeMone (1994), Vertical Velocity in Oceanic Convection off Tropical Australia, *J. Atmos. Sci.*, *51*(21), 3183–3193.
- Mapes, B and R. A. Houze, 1992: An integrated view of the 1987 Australian monsoon and its mesoscale convective systems. I: Horizontal structure. *Quart. J. Roy. Met. Soc.*, **118**, 927-963.
- Masunaga, H. (2012), A Satellite Study of the Atmospheric Forcing and Response to Moist Convection over Tropical and Subtropical Oceans, *J. Atmos. Sci.*, *69*(1), 150–167, doi:10.1175/JAS-D-11-016.1.
- Masunaga, H. (2013), A Satellite Study of Tropical Moist Convection and Environmental Variability: A Moisture and Thermal Budget Analysis, *J. Atmos. Sci.*, *70*(8), 2443–2466, doi:10.1175/JAS-D-12-0273.1.
- Meskhidze, N., L. A. Remer, S. Platnick, R. Negron, A. M. Lichtenberger, and A. R. Aiyyer (2009), and Physics Exploring the differences in cloud properties observed by the Terra and Aqua MODIS Sensors, *Atmos. Chem. Phys.*, *9*, 3461–3475.
- Meyers, M.P., R. L. Walko, J. Y. Harrington, and . R. Cotton (1997), New RAMS microphysics parameterization. Part II: The two-moment scheme. *Atmos. Res.*, **45**, 3-39.
- Moncrieff, M. W. and M. J. Miller (1976), The dynamics and simulation of tropical cumulonimbus and squall lines. *Quart. J. Roy. Met. Soc.*, **102**, 373-394.
- Nesbitt, S. W., and E. J. Zipser (2003), The Diurnal Cycle of Rainfall and Convective Intensity according to Three Years of TRMM Measurements, *J. Clim.*, *16*, 1456–1475.
- Nesbitt, S. W., E. J. Zipser, and D. J. Cecil (2000), A Census of Precipitation Features in the Tropics Using TRMM: Radar, Ice Scattering, and Lightning Observations, *J. Clim.*, *13*(23), 4087–4106.
- Nesbitt, S. W., R. Cifelli, and S. a Rutledge (2006), Storm Morphology and Rainfall Characteristics of TRMM Precipitation Features, *Mon. Weather Rev.*, *134*(10), 2702–2721.
- Peters, K., C. Jakob, L. Davies, B. Khouider, and A. J. Majda (2013), Stochastic Behavior of Tropical Convection in Observations and a Multicloud Model, *J. Atmos. Sci.*, *70*(11), 3556–3575, doi:10.1175/JAS-D-13-031.1.
- Pruppacher, H. R. and J. D. Klett (2010), *Microphysics of Clouds and Precipitation*, Springer, 954pp.
- Ramanathan, V., and W. Collins (1991), Thermodynamic regulation of ocean warming by cirrus clouds deduced from observations of the 1987 El Nino, *Nature*, *351*, 27–32.
- Remer, L. A., Kaufman, Y. J., Tanré, D., Mattoo, S., Chu, D. A., Martins, J.V., Li, R-R., Ichoku, C., Levy, R. C., Kleidman, R. G., Eck, T. F. Vermote, E., and Holben, B. N.: The MODIS aerosol algorithm, products, and validation, *J. Atmos. Sci.*, *62*(4), 947– 973, doi:10.1175/JAS3385.1, 2005.
- Rickenbach, T., P. Kucera, M. Gentry, L. Carey, A. Lare, R.-F. Lin, B. Demoz, and D. O. Starr (2008), The Relationship between Anvil Clouds and Convective Cells: A Case Study in South Florida during CRYSTAL-FACE, *Mon. Weather Rev.*, *136*(10), 3917–3932, doi:10.1175/2008MWR2441.1.

- Riley, E. M., B. E. Mapes, and S. N. Tulich (2011), Clouds Associated with the Madden–Julian Oscillation: A New Perspective from CloudSat, *J. Atmos. Sci.*, *68*(12), 3032–3051, doi:10.1175/JAS-D-11-030.1.
- Roff, G. L., and J.-I. Yano (2002), Tropical convective variability in the CAPE phase space, *Q. J. R. Meteorol. Soc.*, *128*(585), 2317–2333, doi:10.1256/qj.01.138.
- Rotunno, R., J. B. Klemp, and M. L. Weisman (1988), A Theory for Strong, Long-Lived Squall Lines, *J. Atmos. Sci.*, *45*(3), 463–485.
- Sassen, K., Z. Wang, and D. Liu (2009), Cirrus clouds and deep convection in the tropics: Insights from CALIPSO and CloudSat, *J. Geophys. Res.*, *114*(June), 1–11, doi:10.1029/2009JD011916.
- Saxen, T. R., and S. A. Rutledge (2000), Surface Rainfall – Cold Cloud Fractional Coverage Relationship in TOGA COARE: A Function of Vertical Wind Shear, *Mon. Weather Rev.*, *128*, 407–415.
- Schneider, T., P. A. O’Gorman, and X. J. Levine (2010), WATER VAPOR AND THE DYNAMICS OF CLIMATE CHANGES, *Rev. Geophys.*, *48*, doi:10.1029/2009RG000302.1.INTRODUCTION.
- Sherwood, S. C. (1999), Convective Precursors and Predictability in the Tropical Western Pacific, *Mon. Weather Rev.*, *127*, 2977–2991.
- Simmons, A., S. Uppala, D. Dee, and S. Kobayashi (2007), The ERA interim reanalysis, *ECMWF Newsl.*, *110*, 25–35.
- Stephens, G. L. (2005), Cloud Feedbacks in the Climate System: A Critical Review, *J. Clim.*, *18*(2), 237–273.
- Stephens, G. L. et al. (2002), The Cloudsat Mission and the A-Train, *Bull. Am. Meteorol. Soc.*, *83*(12), 1771–1790, doi:10.1175/BAMS-83-12-1771.
- Stephens, G. L. et al. (2008), CloudSat mission: Performance and early science after the first year of operation, *J. Geophys. Res.*, *113*, D00A18, doi:10.1029/2008JD009982.
- Storer, R. L., S. C. Van Den Heever, and T. S. L. Ecuyer (2014), Observations of aerosol-induced convective invigoration in the tropical east Atlantic, *J. Geophys. Res. Atmos.*, (May 2013), 3963–3975, doi:10.1002/2013JD020272.Abstract.
- Storer, R. L., and S. C. van den Heever (2013), Microphysical processes evident in aerosol forcing of tropical deep convective clouds. *J. Atmos. Sci.*, **70**, 430–446.
- Susskind, J., C. Barnet, J. Blaisdell, L. Iredell, F. Keita, L. Kouvaris, G. Molnar, and M. Chahine (2006), Accuracy of geophysical parameters derived from Atmospheric Infrared Sounder/Advanced Microwave Sounding Unit as a function of fractional cloud cover, *J. Geophys. Res.*, *111*(D9), D09S17, doi:10.1029/2005JD006272.
- Tao, W., J. Chen, Z. Li, C. Wang, and C. Zhang (2012), IMPACT OF AEROSOLS ON CONVECTIVE CLOUDS AND PRECIPITATION, *Rev. Geophys.*, *50*, doi:10.1029/2011RG000369.1.INTRODUCTION.
- Twomey, S. 1977: The influence of pollution on the shortwave albedo of clouds, *J. Atmos. Sci.*, *34*, 1149–1152, doi:10.1175/1520-0469(1977)034<1149:TIOPOT>2.0.CO;2. 6823
- van den Heever, S. C., G. L. Stephens, and N. B. Wood (2011), Aerosol Indirect Effects on Tropical Convection Characteristics under Conditions of Radiative-Convective Equilibrium. *J. Atmos. Sci.*, **68**, 699-718.
- van den Heever, S. C., G. G. Carrio, W. R. Cotton, P. J. DeMott, and A. J. Prenni (2006), Impacts of nucleating aerosol on Florida storms. Part I: Mesoscale simulations. *J. Atmos. Sci.*, **63**, 1752–1775.

- Wall, C., E. Zipser, and C. Liu (2014), An Investigation of the Aerosol Indirect Effect on Convective Intensity Using Satellite Observations, *J. Atmos. Sci.*, *71*(1), 430–447, doi:10.1175/JAS-D-13-0158.1.
- Wen, G., Marshak, A., Cahalan, R., Remer, L., and Kleidman, R.: 3-D aerosol-cloud radiative interaction observed in collocated MODIS and ASTER images of cumulus cloud fields, *J. Geophys. Res.*, *112*, D13204, doi:10.1029/2006JD008267, 2007. 6825
- Weisman, M. L. (1993), The Genesis of Severe, Long-Lived Bow Echoes, *J. Atmos. Sci.*, **50**, 645-670.
- Weisman, M. L., and J. B. Klemp (1982), The Dependence of Numerically Simulated Convective Storms on Vertical Wind Shear and Buoyancy, *Mon. Weather Rev.*, *110*, 504–520.
- Weisman, M. L., and R. Rotunno (2004), “A Theory for Strong Long-Lived Squall Lines” Revisited, *J. Atmos. Sci.*, *61*(4), 361–382, doi:10.1175/1520-0469(2004)061<0361:ATFSLS>2.0.CO;2.
- Wood, N. (2008), Level 2 Radar-Visible Optical Depth Cloud Water Content Process Description Document, Version 5.1, CloudSat Project, CIRA, Colorado State University, Fort Collins, 26 pp.
- Yano, J., and R. S. Plant (2012), Convective quasi-equilibrium, *Rev. Geophys.*, *50*(2011), 1–30, doi:10.1029/2011RG000378.
- Ye, B., A. D. Del Genio, and K. K.-W. Lo (1998), CAPE Variations in the Current Climate and in a Climate Change, *J. Clim.*, *11*, 1997–2015.
- Yuan, T., L. A. Remer, K. E. Pickering, and H. Yu (2011), Observational evidence of aerosol enhancement of lightning activity and convective invigoration. *Geophys. Res. Lett.*, **38**, L04701, doi:10.1029/2010GL046052.
- Yue, Q., E. J. Fetzer, B. H. Kahn, S. Wong, G. Manion, A. Guillaume, and B. Wilson (2013), Cloud-State-Dependent Sampling in AIRS Observations Based on CloudSat Cloud Classification, *J. Clim.*, *26*(21), 8357–8377, doi:10.1175/JCLI-D-13-00065.1.
- Zelinka, M. D., and D. L. Hartmann (2009), Response of Humidity and Clouds to Tropical Deep Convection, *J. Clim.*, *22*(9), 2389–2404, doi:10.1175/2008JCLI2452.1.

Chapter VI

- Wood, R., and P. R. Field (2011), The distribution of cloud horizontal sizes, *J. Climate*, *24*(18), 4800–4816, doi:10.1175/2011JCLI4056.1.